UNIVERSIDADE D
COIMBRA

Gabriel Oliveira Salgado

POLARIMETRY FOR HIGH-ENERGY ASTROPHYSICS

Thesis submitted to the University of Coimbra in fulfillment of the requirements for the Master's Degree in Physics Engineering under the scientific supervision of Ph.D. Rui Miguel Curado da Silva and Ph.D. Jorge Manuel Maia Pereira.

November 2021

1 2 9 0

FACULDADE DE CIÊNCIAS E TECNOLOGIA
UNIVERSIDADE D COIMBRA

Integrated Master in Physics Engineering

Polarimetry for High-Energy Astrophysics

LABORATÓRIO DE INSTRUMENTAÇÃO
E FÍSICA EXPERIMENTAL DE PARTÍCULAS
partículas e tecnologia

Gabriel Oliveira Salgado

Thesis submitted to the University of Coimbra in fulfillment of the requirements for the Master Degree in Physics Engineering

Supervisor:
Ph.D. Rui Miguel Curado da Silva
Ph.D. Jorge Manuel Maia Pereira

Coimbra, November 2021

Dedicado ao meu irmão.

Agradecimentos

Em primeiro lugar, agradeço ao Professor Rui Silva pela oportunidade de trabalhar neste projeto, pela sua orientação e pela partilha de conhecimento. Agradeço ao Dr. Miguel Moita, por toda a sua ajuda e disponibilidade que sempre demonstrou ao longo deste projeto, e à Dr. Henrike Fleischhack por me ter integrado na equipa do AMEGO.

Agradeço a todos os meus amigos que fiz durante o curso e também aqueles que me acompanham há mais tempo, pelo caminho que percorremos juntos e pela influência que tiveram em mim. Foram anos marcantes onde tivemos a oportunidade de aprender e crescer juntos. Vivemos grandes momentos, e certamente mais estarão por vir. Agradeço especialmente ao Afonso Marques que dedicou o seu tempo para me ajudar e corrigir este trabalho. Agradeço-lhe pela sua amizade e companhia durante este período. Agradeço também ao David Marques pela sua amizade desde o dia em que nos conhecemos. Agradeço aos Fonitos, pelas noites e momentos memoráveis. É um orgulho fazer parte desta família. Agradeço também ao Rodrigo Martins e Jorge Valério pelas suas velhas amizades. Espero levar estas amizades comigo para a vida.

Agradeço aos meus pais, pois sem eles nada disto seria possível. Obrigado pelo apoio e motivação que me dão, e pelo esforço e sacrifícios que fizeram. Agradeço pela educação e pelos valores que me transmitiram. Agradeço ao irmão, de quem tenho muito orgulho, por ser um patolas. Agradeço-vos por todo o amor.

Agradeço à minha querida Melissa, pelo carinho e força que me dá, por se preocupar e cuidar de mim, e por estar ao meu lado nos bons e maus momentos. Obrigado por fazeres parte da minha vida.

Resumo

A polarimetria é aplicada ao longo de todo o espetro electromagnético, contribuindo há décadas para o estudo de fontes astronómicas. A polarimetria contribui com medições do ângulo de polarização e do nível de polarização linear de fotões, permitindo a distinção entre modelos concorrentes de mecanismos de emissão de fontes astronómicas. No entanto, a polarimetria de altas energias começou a progredir apenas nos últimos 20 anos, contribuindo com medições polarimétricas da Nebulosa do Caranguejo e de explosões de raios gama (gamma-ray burst, GRB). Apesar dos avanços desta área, os mecanismos de emissão de GRBs ainda são desconhecidos.

O objetivo deste trabalho é caracterizar, através de simulações, a sensibilidade à polarização dos instrumentos AMEGO e AMEGO-X. O AMEGO foi desenhado para a chamada de missões da NASA do tipo *probe*, enquanto o AMEGO foi desenhado para o tipo de missões MIDEX. O segundo consiste numa versão de um instrumento mais leve e menos complexo que o primeiro, com um custo associado menor. O AMEGO irá operar como um telescópio de Compton e de produção de pares e irá observar o céu em modo *survey*, promovendo sinergias com outros observatórios e contribuindo para a astrofísica multimensageira. É capaz de produzir imagens e realizar medições de espectroscopia, temporais e polarimétricas, com melhores sensibilidades que instrumentos anteriores, na gama de energias da ordem dos MeV.

A sensibilidade à polarização do AMEGO e do AMEGO-X são determinadas através de simulações com o MEGAlib, que é uma ferramenta que permite simular a interação de radiação γ com detetores de radiação. Os fatores de modelação do AMEGO e do AMEGO-X, apresentam um valor superior nas energias mais baixas, e diminuem à medida que a energia dos fotões aumenta, apresentando um valor de ~ 0.57 e ~ 0.43, a 200 keV, e ~ 0.16 e ~ 0.06, a 1100 keV. O valor mais alto da eficiência do AMEGO é obtido a 600 keV e corresponde a $\sim 20\%$, enquanto a eficiência do AMEGO-X é $\sim 5\%$ nesta energia, para fotões com um ARM menor que 15°.

É avaliada a contribuição de cada detetor para a eficiência e para o fator modelação. O calorímetro de baixas energias é o detetor que mais contribui para a o fator de modelação e eficiência do instrumento. Isto é observado para interações que ocorrem unicamente com este detetor, mas também para interações que ocorrem entre pares de detetores. O calorímetro de baixas energias consiste num detetor plano único, com uma espessura de 4 cm e feito de um material de alto número atómico. O alto número atómico e a sua espessura contribuem para a sua elevada eficiência, e a sua geometria contribui para um fator de modelação alto, devido a deteção de fotões que são dispersos a ângulos perto de 90°. O pares de detetores

que apresentam melhores eficiências a energias abaixo de $\sim$ 800 keV é o par constituído pelo calorímetro de baixas energias e pelo detetor *tracker*, e acima destas energias a melhor eficiência é obtida com o calorímetros de baixas e altas energias. Os pares que contribuem com o melhor fator de modelação são aqueles que não estão alinhados verticalmente, o que favorece a deteção de fotões que dispersam perto de ângulos retos.

Em relação às sensibilidades polarimétricas dos instrumentos nas suas condições de operação, é calculada a polarização mínima detetável (minimum detectable polarization, MDP) em função do tempo de observação para a GRB 170817A, um modelo de GRBs curtas e para a Nebulosa do Caranguejo. É observado que as diferenças da sensibilidade à polarização entre os dois instrumentos são mais acentuadas para fontes com baixa emissão e para tempos de observação curtos. Para a GRB 170817A, é obtido uma MDP de $\sim$ 55% e $\sim$ 78%, com o AMEGO e AMEGO-X, respetivamente, enquanto que para a GRB mais intensa do modelo de GRBs curtas, é esperado uma MDP de $\sim$ 10% e $\sim$ 20%, respetivamente. Para um tempo de observação de 10^3 s, da Nebulosa do Caranguejo, é obtida uma MDP de $\sim$ 42% e $\sim$ 64%, com o AMEGO e AMEGO-X, respetivamente, e para um tempo de observação de 10^6 s, as MDPs são $\sim$ 1% e $\sim$ 2%.

O AMEGO apresenta melhores sensibilidades à polarização e será capaz de fazer medições polarimétricas de fontes menos intensas do que o AMEGO-X. A proposta dos dois instrumentos aumenta a probabilidade de um ser aceite e lançado para orbita, o que beneficiará várias áreas da astrofísica na região de energia dos MeV.

Palavras-chave: AMEGO, AMEGO-X, Radiação gama, Polarimetria, Polarimetro, Polarização mínima detetável, Erupções de raios gama, Nebulosa do Caranguejo.

Abstract

Polarimetry is an active field across the electromagnetic spectrum and has played a significant role on the study of astronomical sources for decades. Polarimetry contributes with measurements of the polarization angle and degree of linear polarization of photons, allowing the discrimination between competing models of emission mechanisms of astronomical sources. However, high-energy polarimetry has known its first progresses only in the past couple decades, contributing with measurements of the Crab and of bright gamma-ray bursts (GRBs). Despite the advances in this field, the emission mechanisms behind GRBs are still unknown.

The objective of this work is to characterize, through simulations, the sensitivity to polarization of the AMEGO and AMEGO-X instruments. AMEGO is projected for the probe-class NASA missions call, while AMEGO-X is designed for the MIDEX call. The second consists of lighter and less complex version of the first, with a smaller cost. AMEGO will operate as a Compton-pair telescope observing the sky in survey mode, promoting synergies with other observatories and contributing to the multi-messenger astrophysics. It is capable of performing imaging, spectroscopic, timing and polarimetric measurements, providing better sensitivities than previous instruments, in the MeV range.

The potential polarimetric sensitivity of AMEGO and AMEGO-X is estimated through simulations with MEGAlib, which is a consolidated Monte Carlo simulation tool that simulates the interactions of the γ radiation with the radiation detectors. The modulation factors of AMEGO and AMEGO-X are its highest values at low-energies, decreasing as the energy of the photons increases, presenting a value of ~ 0.57 and ~ 0.43, at 200 keV, and ~ 0.16 and ~ 0.06, at 1100 keV. The efficiency of AMEGO is at its highest at 600 keV and corresponds to $\sim 20\%$, while the efficiency of AMEGO-X corresponds to $\sim 5\%$, at this energy, while applying an ARM cut of $15°$.

The contribution that each detector type has on the overall efficiency and modulation factor is assessed. The low-energy calorimeter is the detector that contributes the most for the modulation factor and efficiency of the instrument. This is observed for interactions happening uniquely in this detector, but also for interactions that happen in pairs of detectors. The low-energy calorimeter consists of a 4 cm thick, high atomic number, single plane detector. Its thickness and high atomic number contributes to its efficiency and its single plane geometry to its high modulation factor, due to the measurement of photons that scatter close to right angles. Regarding the pairs of detectors, the best efficiency at energies below ~ 800 keV is obtained with

the low-energy calorimeter and the tracker detector, and above this energy the best efficiency is obtained with the low and high-energy calorimeter. The best modulation factors obtained with pairs of detectors are obtained with the ones that are not vertically aligned, which favors the detection of photons scattered at near right angles.

Regarding the sensitivities to polarization of the instruments in its operation conditions, it is computed the minimum detectable polarization (MDP) as a function of the observation time for the GRB 170817A, a model of short gamma-ray bursts (GRBs) and the Crab. It is observed that the differences of the sensitivity to polarization, between both instruments, are more distinct for weak sources and for short observation times. It is determined that for the GRB 170817A, a MDP of $\sim 55\%$ and $\sim 78\%$ is obtained with AMEGO and AMEGO-X, respectively, while for the most intense GRB of the short GRB model, it is expected a MDP of $\sim 10\%$ and $\sim 20\%$, respectively. For an observation time of 10^3 s of the Crab, a MDP of $\sim 42\%$ and $\sim 64\%$ is obtained with AMEGO and AMEGO-X, respectively, and for an observation time of 10^6 s, the MDPs are $\sim 1\%$ and $\sim 2\%$.

AMEGO presents a higher sensitivity to polarization and will be able to perform polarimetric measurements of weaker sources than AMEGO-X. The proposal of the two instruments increases the odds of one being accepted and launched, which will benefit many areas of the MeV astrophysics.

Keywords: AMEGO, AMEGO-X, Gamma radiation, Polarimetry, Polarimeter, Minimum detectable polarization, Gamma-ray bursts, Crab.

Contents

List of Figures

List of Tables

List of Acronyms

ACD Anti-Coincidence Detector.

AMEGO All-sky Medium Energy Gamma-ray Observatory.

AMEGO-X All-sky Medium Energy Gamma-ray Observatory eXplorer.

ARM Angular Resolution Measure.

COMPTEL Imaging Compton Telescope.

DSSD Double-sided Silicon Strip Detector.

FOV Field Of View.

GRB Gamma-Ray Burst.

GW Gravitational Wave.

HIGS High Intensity Gamma-Ray Source.

INTEGRAL INTErnational Gamma-Ray Astrophysics Laboratory.

MDP Minimum Detectable Polarization.

MEGA Medium Energy Gamma-ray Astronomy.

MEGAlib Medium-Energy Gamma-ray Astronomy library.

MIDEX Medium-Class Explorer.

PMT Photomultiplier Tube.

PoGO Polarised Gamma-ray Observer.

RBT Radial Bin Technique.

SiPM Silicon Photomultiplier.

SPI SPectrometer of INTEGRAL.

Introduction

Motivation

Polarimetric measurements of X and γ radiation from astronomical sources, can provide information on the properties of the sources that can not be determined with spectroscopic, imaging and timing measurements. It increases the number of observational parameters by two: the degree of linear polarization and the polarization angle of the emissions from astronomical sources, allowing to differentiate between different emission mechanisms that can be at play [1]. It also allows to probe the conditions of the source, such as the geometry of its magnetic fields.

The study of polarization of photons in the radio, optical, UV and X-ray wavelengths has played a significant role in the study of astronomical sources for decades [2]. Polarimetry, for energies above $\sim$ 100 keV, suffers from challenges such as the low fluxes of astronomical sources at these energies. Despite the challenges, polarimetry for high-energy astrophysics has progressed significantly in the past 20 years. INTEGRAL has contributed successfully with polarimetric measurements of the Crab Nebula and of gamma-ray bursts (GRBs). POLAR also performed polarimetric measurements for bright GRBs. Despite their contributions, the mechanisms behind GRBs are still unknown, due to inconclusive results [2, 3]. These instruments and their contributions will be addressed and presented in section 2.4. Despite the progress made in this field, the polarimetric measurements remain for energies below the pair-production threshold and no γ-ray polarimeter for energies above $\sim$ 1 MeV has been flown to space.

In this work it will be characterized the polarimetric sensitivities of the AMEGO and AMEGO-X mission proposals, which will observe the γ-ray sky. This characterization allows for the estimation of the performance of the instruments and to perform calibrations that can not be performed once the instruments are in orbit.

Framework

This work was developed in the Space Instrumentation for Astrophysics (i-Astro) group of the Laboratory of Instrumentation and Experimental Particle Physics (LIP). LIP is a laboratory with experience on nuclear and radiation physics and on the development of radiation detectors, and i-Astro has experience on the development of γ-ray detectors with spectroscopic, imaging and polarimetric capabilities.

The framework of this thesis is based in the participation of i-Astro group in consortium of the AMEGO mission. AMEGO is a probe-class mission concept proposed to NASA. Its team consists of more than 200 scientists from 15 countries. It operates as a Compton-pair telescope, performing measurements of γ-rays from astronomical sources, covering the 200 keV to 10 GeV energy range. It is capable to perform spectroscopic, imaging, timing and polarimetric measurements, with better sensitivities than previous instruments. The participation of i-Astro in AMEGO proposal is due to its expertise on high-energy astrophysics polarimetry, contributing to the design, optimization and development the AMEGO instrument for polarimetric observations. The work described in this thesis is part of this effort of designing and optimizing the AMEGO instrument. During this project, me and i-Astro team were in permanent contact with the AMEGO team, headed by NASA Goddard Space Centre, participating in videoconference meetings, performing tasks requested by the team and presenting the respective results. Currently, it is being built a prototype of the instrument that will be calibrated at the High Intensity Gamma-Ray Source (HIGS) from Duke University and will go through a balloon flight, by the end of 2022. Our group will coordinate the polarimetric measurements that will be performed during these experimental campaigns. A smaller version of AMEGO, the AMEGO-X, is being proposed as a MIDEX mission. This instrument is also object of this thesis.

Objectives

The objective of this work is to characterize the sensitivity to polarized radiation from astronomical sources, of the AMEGO and AMEGO-X instruments, through simulations. This includes:

- Evaluating the effects that parameters used during the data analysis have on the response of the instruments to polarized photons.
- Computing the modulation factor and efficiency, as a function of the energy, for different polarization angles and different angles of irradiation.
- Estimating the contribution of each family of detectors, as well as the combination of the detectors that provide the best polarimetric performance.
- Determining the sensitivity of the instruments in its conditions of operation, such as the minimum detectable polarization, for astronomical sources, as a function of the observation time.

Thesis structure

This document is divided into four chapters:

- In chapter 1 - Gamma-ray polarimetry - is presented the contributions of polarimety to

the study of astronomical sources. It is presented mechanisms that produce polarized γ radiation and astronomical sources that can probed through polarimetric measurements.

- In chapter 2 - Gamma-ray detection & measurement - is presented the main interaction mechanisms of γ-rays with matter and how polarimetric information can be retrieved from these. It is described the working principle of Compton telescopes and the methods used to perform polarimetric measurements. At the end of the chapter, it is described the instruments of astronomical polarimeters and their contributions, and it is presented MEGAlib, a software tool capable of simulating and analysing data from γ-ray detectors.
- In chapter 3 - The AMEGO mission - is presented the AMEGO mission and descriptions of its detectors. It is presented the simulations and methods used to characterize the polarimetric sensitivity of AMEGO and AMEGO-X, and the results are exposed and discussed.
- In chapter 4 - Conclusion - is presented the main conclusions and proposed future work.

1

Gamma-ray polarimetry

This chapter presents the motivations for γ-ray polarimetry, examples of emission mechanism of polarized γ-rays and astronomical sources that can be studied through polarimetric measurements.

1.1 Polarization of gamma-rays

Gamma-rays are a a form of electromagnetic (EM) radiation. These correspond to photons with the highest energy of the EM spectrum. EM waves consist of an electric and magnetic field, oscillating in orthogonal directions with inversely correlated amplitudes, propagating through space at a constant velocity. The orientation of these fields over time characterize the polarization of the photons. If the orientation of the fields is constant, the photon is said to be linearly polarized. If these rotate, the photon is said to be elliptically polarized. Elliptical polarization will not be considered in this work, as only linear polarization can be measured using current γ-ray polarimetry techniques [4]. The *degree of linear polarization*, Π, is the fraction of linearly polarized photons on a flux of photons. If all photons are linearly polarized with the same polarization angle, the Π equals to 100%, if the photons are randomly polarized, it equals to 0%.

1.2 Polarized gamma-ray emission mechanisms

Astronomical γ-ray emissions are mainly due to non-thermal mechanisms. Different degrees of linear polarization can be expected from the different emission mechanisms, thus the implementation of polarization measurements can help discriminate between emission mechanisms, and better understand the astronomical sources. Examples of emission or interaction mechanisms that produce polarized radiation are: *bremsstrahlung*, *magneto-bremsstrahlung* and *Compton scattering*. The descriptions of these mechanisms are based on [1].

Bremsstrahlung radiation is the radiation produced by the acceleration of charged particles, generally in a nucleus of an atom. Under the Coulomb field of the nucleus, the charged particles are accelerated and convert its kinetic energy to EM radiation. This phenomenon is more significant in electrons, as they experience greater accelerations due to their low-mass.

The degree of linear polarization varies with the emission angle, relative to the direction of the incident particles, reaching a maximum for a given scattering angle that varies with the energy of the incident electron. The degree of linear polarization can reach levels of 80%, and the polarization angle tends to be parallel to the direction of the acceleration. In regions where electrons are assumed to have random directions, the radiation is expected to be unpolarized [2].

Magneto-bremsstrahlung radiation is produced by the movement of charged particles, subject to a centripetal acceleration due to the Lorentz force, around a magnetic field. Depending on the energy of the charged particle, the emission can be characterized as cyclotron or synchrotron. The cyclotron radiation is emitted by non-relativistic electrons, having the greatest intensity in the perpendicular direction to the acceleration, while synchrotron radiation is due to relativistic electrons, resulting in a confined beam in the direction of motion of the electrons that is only observed if emitted in the direction of the observer. The cyclotron radiation is polarized with a polarization angle lying in the plane described by the acceleration vector and the direction of the photon. The synchrotron radiation is elliptically polarized, but as the energy of the electron increases the radiation tends toward linear polarization. In the astronomical context, the distribution of the energies of electrons are often approximated to a power-law. The degree of linear polarization, with a power-law distribution of energies, is given by:

$$\Pi = \frac{\alpha + 1}{\alpha + 7/3}, \tag{1.1}$$

where α is the power-law index. For power-law indices from 1.0 to 5.0, observed for astrophysical synchrotron sources, the observed degree of linear polarization ranges from 65% to 80%.

Compton scattering consists of the scattering of high-energy photons on electrons, where the incident photon transfers a fraction of its energy to an electron. It will be further described in section 2.3. **Inverse Compton scattering**, consist of the scattering of low-energy photons due to collisions with relativistic electrons, which can scatter optical photons to γ-rays, with energies in the MeV range. The polarization of photons scattered through Compton scattering can, in theory, reach almost 100%. It depends on the energy of the incident photons and on their scattering angle. In figure 1.1 is presented the expected degree of linear polarization as a function of the scattering angle, in the scattering of unpolarized beam. In the case of the scattering of a 100% linearly polarized beam, the angle of the scattering also allows to compute the resultant degree of linear polarization. More information on this, can be found in [1].

1.3 Astronomical gamma-ray sources

In this section it is presented the astronomical sources addressed in this work, that can be probed through polarimetry, such as the Crab and GRBs.

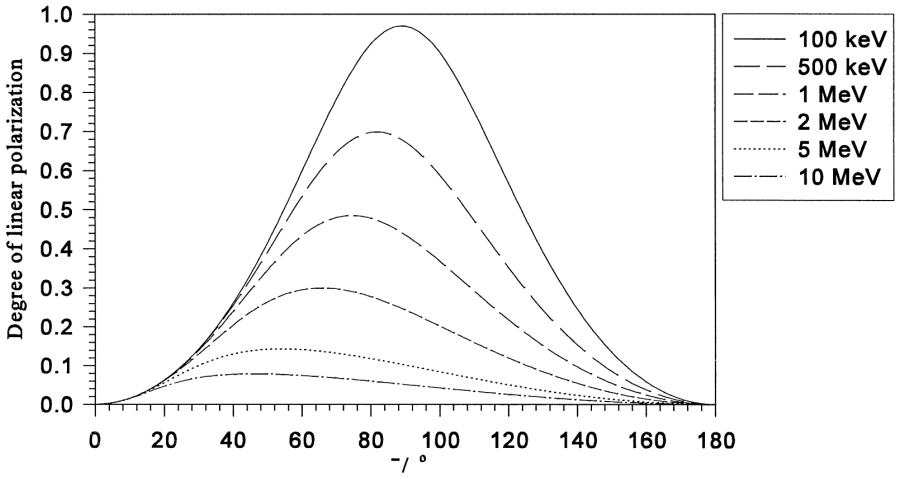

Figure 1.1: Degree of linear polarization of Compton scattered photons from a unpolarized beam, as a function of the scattering angle. Figure from [1].

1.3.1 Crab

The Crab is the result of the supernova SN 1054, which was observed in 1054 by Chinese astronomers. The event was bright enough that it could be observed during the day for some days and, for the following two years it could be observed with the naked eye during the night [5].

Above 200 keV, the Crab is the brightest persistent source in the sky [6]. As it is a very intense and constant source [5], the fluxes of astrophysical sources are commonly described as multiples of the Crab flux, such as the mCrab. The Crab consists of the SN 1054 remnant, known as the Crab nebula, and of a central star, the Crab pulsar, which has a stable spin period of ~ 33 ms and emmits EM radiation that covers the full spectrum, ranging from radio-waves to high-energy γ-rays ($\sim 10^{12}$ eV) [7]. It is believed that the pulsar injects high-energy electrons into the nebula, which irradiate via synchrotron emission [5]. Polarimetry can be used to understand the wind geometry of the pulsar and its magnetic field [6]. Figure 1.2 presents the pulses of the signal due to the pulsar emission. A power-law is used to fit the diffuse and pulsed emission. In [5], observational data from a set of instruments is used to perform a fit of the overall spectra of the Crab to a power-law, in different energy ranges. It was determined that in the 50 keV to 1 MeV energy range, the normalization constant and the index of the power-law are 10.74 and 2.17, respectively.

Forot et al. [6], performed a polarimetric analysis with data from the Crab, in the 200 to 800 keV energy range. It was observed that no significant polarized emission is found in the pulsed component and that the radiation emitted in the off-pulse signals is polarized, with a polarization angle parallel to the pulsar rotation axis, suggesting that the high-energetic polarized radiation is produced inside the pulsar nebula.

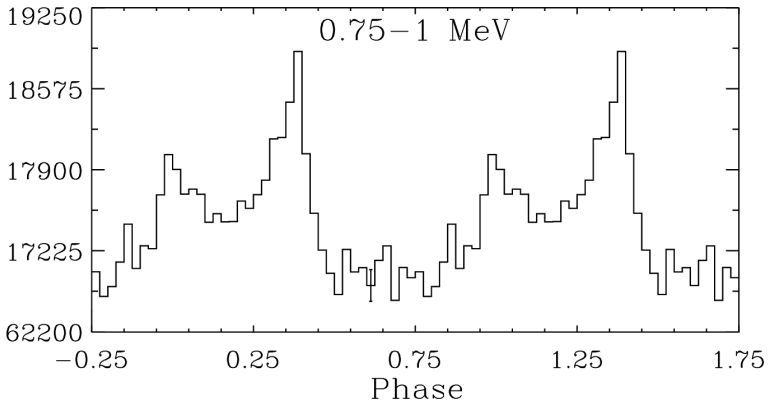

Figure 1.2: Pulse profile (double cycle) of the Crab pulsar, measured by COMPTEL in the 0.75 to 1 MeV energy range. The pulse profile can be divided in four phase intervals: the two main peaks, from -0.12 to 0.14 and from 0.25 to 0.52, the bridge, from 0.14 to 0.25, and the off-pulse, from 0.52 to 0.88 [6]. Figure adapted from [8].

1.3.2 Gamma-ray bursts

Gamma-ray bursts are short-lived transients of γ radiation that are observed in random direction in the sky, with durations that range from a few ms to hundreds of seconds. These are the most luminous events in the universe, emitting an energy that spans from 10^{50} to 10^{54} erg (1 erg = 10^{-7} J = 6.2415×10^{11} eV) and temporarily outshining all other sources. Despite their short duration, through the long-lived X-ray and optical counterparts it is possible to assess properties of the sources, such as their redshifts [3].

The GRBs are separated in two classes: short and long GRBs. The classification is usually performed by their duration, but a more complex classification can be performed using the hardness of their spectra. The short GRBs are commonly defined as those with a duration below 2 s, and it was observed that their spectra is generally harder than the spectra of average long GRB [9], i.e., present a larger component of high-energy photons. These also present lower fluences than long GRBs. The long GRBs are believed to be originated from the collapse of their progenitors, being associated with supernovae [3, 9], while short GRBs are believed to be originated from compact binary mergers, such as the merge of two neutron stars or of a neutron star and a black hole [9]. In 2017, it was performed the first observation of a short GRB originated from the merger of two neutron stars, the GRB 170817A [9, 10].

Despite the study of spectral and timing properties of the GRBs, the physical properties of their origin are still not well understood. Polarimetric measurements should allow to probe the conditions that give origin to a GRB, and provide information on the emission mechanims and on the structure of the magnetic fields involved [11].

GRB 170817A

The GRB 170817A [9, 10] is a short GRB that resulted from the merger of two neutron stars. Its detection marked the first coincident observation of EM radiation and gravitational-waves

(GWs). It was detected by the Fermi Gamma-ray Burst Monitor (GBM) and, ~ 1.7 s prior to the detection of the GRB, the Laser Interferometer Gravitational-wave Observatory (LIGO) detected its GW counterpart. Since 2008, until the detection of the GRB in 2017, the GBM detected more than 2000 GRBs, providing their position, and data for temporal and spectral analysis. From the Fermi's observations it was determined that it is a short GRB with a softer spectrum that the typical short GRBs detected by GBM, and that its peak flux is one of the weakest ones measured. Its fluence is $(2.8 \pm 0.2) \times 10^{-7}$ erg cm^{-2}, in the 10 to 1000 keV energy range.

2

Gamma-ray detection & measurement

In this chapter the main interaction mechanisms for hard X-rays ($E_{ph} \gtrsim 10$ keV) and γ-rays ($E_{ph} \gtrsim 100$ keV) are presented. It is discussed how polarimetric measurements can be performed and it is presented a description of instruments, that are currently on operation or development, capable of performing polarimetry. In the end of the chapter it is given a brief description of MEGAlib, a software capable of simulating instruments for the detection of X and γ-rays, and analyze the results from the simulations and real data.

2.1 Interaction of gamma radiation with matter

The most relevant interaction mechanisms for γ radiation with matter are the *photoelectric effect*, *Compton scattering* and *pair production*. These processes consist of a partial or complete transference of the energy of the photon to an electron or on the conversion of the energy of the photon into a pair composed of an electron and a positron. These interaction mechanisms are described in the following subsections. For the photoelectric effect and the pair production, it is described an instrument capable of performing polarimetry, based on each interaction mechanisms. The Compton polarimeters are discussed in section 2.4.

2.1.1 Attenuation of a flux of photons through a medium

The Beer-Lambert law describes the attenuation of a flux of photons through a medium. The attenuation is described as:

$$\frac{I}{I_0} = e^{-(\frac{\mu}{\rho})\rho t}, \tag{2.1}$$

where I_0 is the initial flux of photons, I is the transmitted flux, μ is the linear attenuation coefficient, ρ is the density of the material, and t is its thickness. The ratio $\frac{\mu}{\rho}$ is known as the mass attenuation coefficient.

In figure 2.1 it is presented the mass attenuation coefficient for silicon, for a wide range of energies in the X and γ-ray spectrum. It can be observed that approximately below 60 keV, the

dominant interaction mechanism is the photoelectric effect. Above this energy and below 10 MeV, the dominant process is the Compton scattering, and above 10 MeV the most significant interaction mechanism is the pair production.

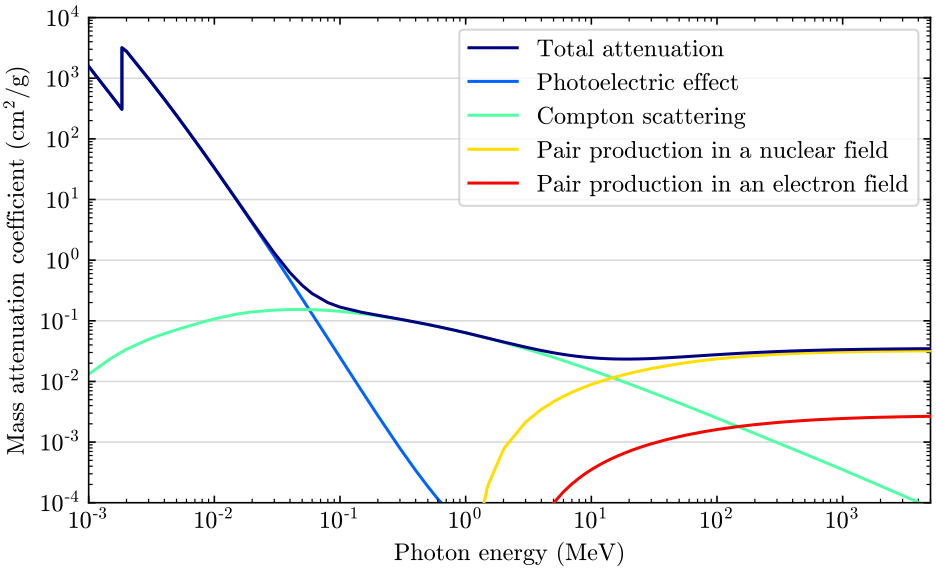

Figure 2.1: Total mass attenuation coefficient, for silicon, as a function of the energy of the photons. It is also presented the contribution of the three most significant interaction mechanisms for high-energy radiation, with the addition of *triplet production* (or pair production in an electron field). The peak, close to the 2×10^{-3} MeV, corresponds to the K-shell binding energy of silicon (1.839 keV) [12]. Data obtained from [13].

The average distance traveled by photons in a medium, before interacting with it, is defined as the *mean free path*, λ, and it is related with the linear attenuation coefficient by $\lambda = 1/\mu$. In table 2.1 it is presented the mean free path for different materials and for different photon energies.

Table 2.1: Mean free path for different photon energies in different mediums. Computed with data from [13].

Energy (MeV)	λ_{Si} (cm)	λ_{CdTe} (cm)	λ_{CsI} (cm)
0.1	2.55	0.11	0.12
0.2	3.48	0.58	0.64
0.5	4.94	1.94	2.40
1	6.77	3.04	3.89
2	9.59	4.23	5.44
5	14.47	4.86	6.15

2.1.2 Photoelectric effect

In the photoelectric effect (or photoelectric absortion), a photon is absorbed by an atom, transferring its energy to an electron. In the case of X and γ-rays, the transferred energy is high enough to eject a photoelectron with a substantial kinetic energy, which may further ionize the medium. The energy of the resulting photoelectron is given by:

$$E_{e^-} = h\nu - E_b, \tag{2.2}$$

where E_{e^-} is the kinetic energy of the photoelectron, $h\nu$ is the energy of the photon, h being the Planck constant and ν the frequency of the photon, and E_b is the binding energy of the electron to the atom. In the X and γ-ray energy range, the photon is more likely to interact with the most tightly bound electron in the K-shell of the atom [14].

The ionization of the atom creates a vacancy in one of its shells. The atom can either capture a free electron, or rearrange its electrons from the outer shells in order to fill the vacancy, generating a characteristic X-ray or an Auger electron.

The photoelectric effect is the dominant process for the interaction of X-rays and low energy γ-rays with matter, as can be seen in figure 2.1. A material with a higher atomic number, Z, has a higher photoelectric cross-section. The probability of photoelectric effect is proportional to $\frac{Z^n}{E_\gamma^{3.5}}$, where n can vary from 4 and 5 and E is the energy of the photon [14].

The photoelectric effect is sensitive to the polarization of the photon. The differential cross-section of s-shell electrons [15], scattered through a polarized photon, is given by:

$$\frac{d\sigma}{d\Omega} = r_0^2 \frac{Z^5}{137^4} \left(\frac{mc^2}{h\nu}\right)^{7/2} \frac{4\sqrt{2}\sin^2(\theta)\cos^2(\phi)}{(1-\beta\cos(\theta))^4}, \tag{2.3}$$

where θ is the polar scattering angle of the electron, and ϕ is its azimuthal scattering angle. The electrons are ejected preferentially in the direction of the polarization plane of the photon.

Some experiments use this mechanism to measure the polarization of X-rays. One example is the Imaging X-ray Polarimetry Explorer (IXPE) [16], a satellite that will be launched in the fall of 2021. IXPE uses polarization-sensitive gas pixel detector [15], and will measure the X-rays emitted from astronomical objects in the 2-8 keV range. The working principle of the polarization-sensitive gas pixel detector is explained in figure 2.2.

2.1.3 Compton scattering

Compton scattering is a phenomenon that consists in the scattering of photons on electrons while they travel through matter. This interaction corresponds to an inelastic scattering, where the photon transfers some of its energy and momentum to an electron, resulting in a change of the direction of the photon. The decrease of the energy of the photon is known as the *Compton shift*. A schematic of the process is presented in figure 2.3. The probability of Compton scattering increases linearly with Z [14].

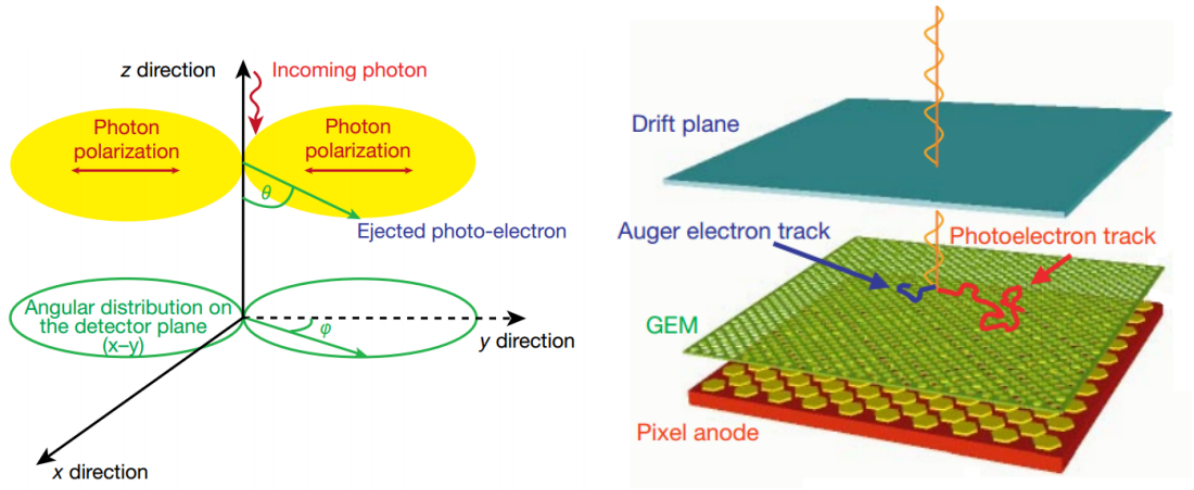

Figure 2.2: On the left it is presented the azimuthal distribution of scattered electrons through a polarized photon. The distribution follows a $\cos^2(\phi)$ function, with the electrons being ejected preferentially in the direction of the angle of polarization. The anisotropic distribution of the scattered electrons is the basis of the polarimetric measurements in the photoelectric regime. On the right it is presented a schematic of a gas pixel detector. The photoelectron leaves a track in the gas, then the electrons ejected along the track are drifted to a gas electron multiplier (GEM), where the charge is amplified. The signal from the charges is measured in a multi-pixel, two-dimensional, read-out anode. From the energy deposited along the track, and its direction, it is possible to reconstruct the direction of the photoelectron. Adapted from [15].

Kinematic equations

The kinematic equations of the Compton scattering are based on the conservation of energy and momentum of the photon and electron:

$$E_i + E_{i,e}^{rel} = E_g + E_e^{rel}, \tag{2.4}$$

$$\vec{p}_i + \vec{p}_{i,e} = \vec{p}_g + \vec{p}_e, \tag{2.5}$$

where $E_{i,e}^{rel} = \sqrt{E_0^2 + p_e^2 c^2} = E_0 + E_e$, and $\vec{p}_i$, $\vec{p}_{i,e}$, $\vec{p}_g$ and $\vec{p}_e$ are the momentum of the incident photon, of the electron before the interaction, of the scattered photon and of the scattered electron.

Generally, it is considered that the collision is given with a free electron at rest. This is an approximation, but in practice the interaction may be given with a bound electron, with energy higher than E_0 and non-null momentum, leading to an effect called *Doppler-broadening*. This effect is addressed in section 2.2.2.

The relation between the scattering angle and the amount of energy lost by the photon, is

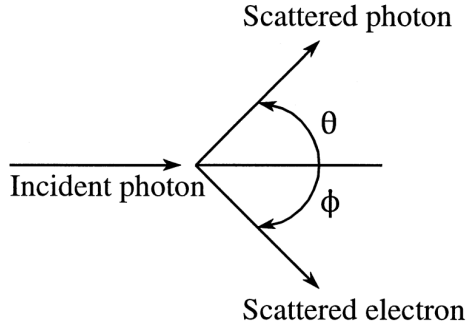

E_i	Energy of the initial photon
E_g	Energy of the scattered photon
E_0	Rest energy of the electron
E_e	Kinetic energy of the recoil electron
E_e^{rel}	Total relativistic energy of the electron
θ	Scattering angle of the photon
ϕ	Scattering angle of the electron

Figure 2.3: Compton scattering schematic. The incoming photon, with energy E_i, transfers some of its energy to an electron, resulting in a photon with energy $E_g < E_i$ and scattering angle θ.

known as the *Compton equation*:

$$\epsilon = \frac{E_g}{E_i} = \frac{1}{1 + \left(\frac{E_i}{E_0}\right)(1 - \cos(\theta))}. \tag{2.6}$$

Rearranging the equation 2.6:

$$\cos(\theta) = 1 - \frac{E_0}{E_g} + \frac{E_0}{E_i}. \tag{2.7}$$

As the $\arccos(\theta)$ domain is $[-1; 1]$, the energy of the recoil particles is constrained to:

$$\frac{E_0 E_i}{2E_i + E_0} < E_g < E_i, \tag{2.8}$$

$$0 < E_e < \frac{2E_i^2}{2E_i + E_0}, \tag{2.9}$$

for the scattered photon and scattered electron, respectively.

Differential cross-section

The Klein-Nishina differential cross-section [1], for unpolarized scattered photons on free electrons at rest, is given by:

$$\left(\frac{d\sigma}{d\Omega}\right)_{unpol} = \frac{r_0^2 \epsilon^2}{2}\left(\epsilon + \epsilon^{-1} - \sin^2(\theta)\right), \tag{2.10}$$

where r_0 is the classical radius of the electron.

As for polarized photons, it is given by:

$$\left(\frac{d\sigma}{d\Omega}\right)_{pol} = \frac{r_0^2 \epsilon^2}{2}\left(\epsilon + \epsilon^{-1} - 2\sin^2(\theta)\cos^2(\phi)\right), \tag{2.11}$$

where ϕ is the azimuthal scattering angle, defined as the angle between the polarization vector and the plane of scattering.

The azimuthal scattering distribution of unpolarized photons is expected to be isotropic, as equation 2.10 does not depend of ϕ. On the other hand, from equation 2.11, it is expected that the azimuthal scattering distribution of polarized photons to be anisotropic.

In figure 2.4 it is shown the dependence of the differential cross-section, for unpolarized photons, as a function of the scattering angle. It can be observed that, as the energy of the photon increases, the probability of a low scattering angle also increases, resulting in a lower fraction of deposited energy in the medium. In figure 2.5 it is represented the theoretical anisotropic azimuthal scattering angle, ϕ, for polarized photons. It can be observed that polarized photons have a higher probability of being scattered on the orthogonal direction to the polarization angle. This property is the basis of polarization measurements in the Compton regime. This topic is further discussed in section 2.3.

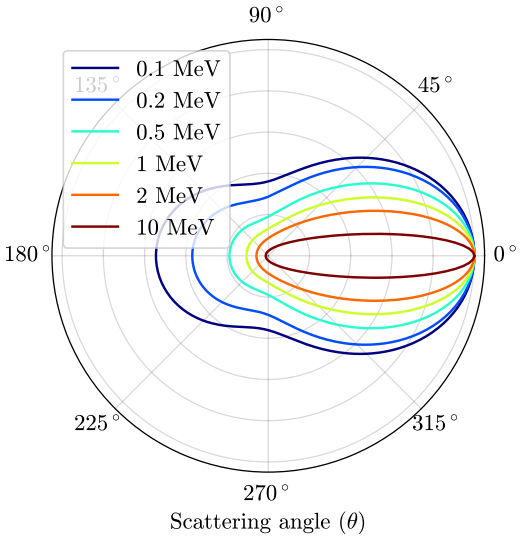

Figure 2.4: Differential cross-section for unpolarized photons [a.u.] as a function of the Compton scattering angle, θ, for different energies. The differential cross-section is independent of the azimuthal angle, ϕ.

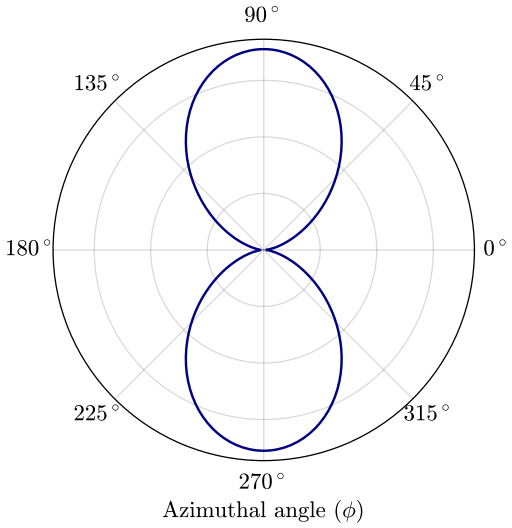

Figure 2.5: Differential cross-section for 100 keV polarized photons [a.u.], as a function of the azimuthal scattering angle, ϕ, scattered at $\theta = 90°$.

2.1.4 Pair production

The existence of positrons was suggested by Paul Dirac in 1928, and was observed experimentally in 1932, by Carl Anderson, with cloud chambers operating under a strong magnetic field, as mentioned in [17]. C. Anderson also observed the signature of a pair production with the observation of symmetrical tracks curving in opposite directions, originated by a photon induced by a cosmic ray. Pair production occurs when photons, with an energy of at least 1.02 MeV (twice the rest-mass energy of an electron), interact with the Coulomb field of a nucleus. If the energy of the photons is four times the rest-mass of the electron, the pair production can occur

in the Coulomb field of the electron - *triplet production* [18]. In nuclear pair production, as in triplet production, the photon is absorbed and its energy is converted into a positron and an electron. In figure 2.6 it is presented a schematic of a pair production.

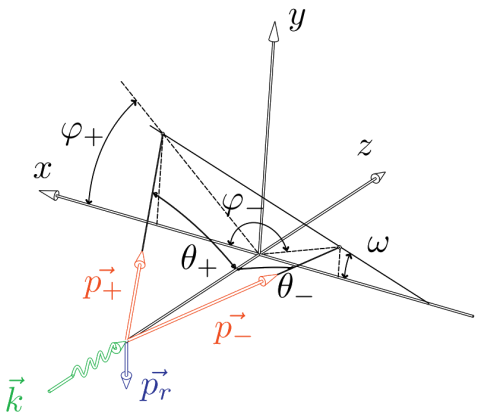

Figure 2.6: Pair production schematic. The subscripts i, $-$, $+$, r stand for the initial photon, electron, positron and recoil particle. θ stands for polar angle, φ for the azimuthal angle, and $\vec{p}$ for the momentum of the particles. $\vec{k}$ is the wave number of the photon and w is the pair plane azimuthal angle.

As conservation of energy must occur, the additional energy of the photon, above the 1.02 MeV threshold, is shared between the electron, the positron and the recoil particle. The conservation laws for the pair production are:

$$E_i = E_- + E_+ + E_r + 2E_0, \tag{2.12}$$

$$\vec{p_i} = \vec{p_-} + \vec{p_+} + \vec{p_r}. \tag{2.13}$$

In the case of an interaction in the Coulomb field of a nucleus, the recoil particle is the nucleus, which absorbs some of the energy and momentum of the photon, but no current instrument for the high-energy astrophysics is sensitive enough to record these parameters [18]. In the case of an interaction in the Coulomb field of an electron the recoil particle is an electron, that generates a track signature.

The probability of pair production varies roughly with Z^2 [14]. For silicon, the nuclear pair production becomes the dominant interaction mechanism for photons with energies above ~ 10 MeV (see figure 2.1), and the cross-section for triplet production is approximately one order of magnitude lower than for nuclear pair production.

Pair production is also sensitive to polarization of the photons. The pair products tend to be coplanar with the direction of the polarization of the photons, resulting in an asymmetry of the azimuthal distribution of the pairs. Polarimetric measurements can be performed through the asymmetry of the azimuthal distribution the events. The differential cross-section is described by [19]:

$$\frac{d\sigma}{d\phi} \propto \Big(1 + A\,P\cos\left(2(\phi - \phi_0)\right)\Big), \tag{2.14}$$

where A is the azimuthal polarization asymmetry of the conversion process, P is the fraction of the linear polarization of the photon beam, ϕ is the azimuthal angle of the event and ϕ_0 is

the orientation of the polarization vector. Experimental effects lead to an effective asymmetry, A_{eff}, that is lower than the theoretical asymmetry, A. The asymmetry dilution, D, is defined by the ratio $D = A_{eff}/A$. At low energies the asymmetry converges to $A = \frac{\pi}{4} \approx 0.785$, and at high energies it converges to $A = 1/7 \approx 0.143$ [20]. The polarization fraction, P, of a γ-ray flux can be measured by analyzing the azimuthal distribution of the pairs, similarly to the Compton scattering techniques (see section 2.3). As mentioned before, the plane of the pair correlates with the polarization angle of the photon, as the pair is emitted preferably in the plane of polarization of the photon. In the case of triplet production, the direction of the recoil electron is more likely to be orthogonal to the plane of polarization [19].

In [20] are discussed the details regarding the extraction of the polarization information. The asymmetry is larger when the electron and the positron share the energy equally and when the opening angle of the pair is small. The attempts made to increase the polarization asymmetry with event selection have shown that, despite the increase of the asymmetry, the reduction of the size of the sample translates in small or no improvements. The use of low-Z active sensors as scatterers, instead of high-Z passive elements, as used in Fermi-LAT telescope, can also increase the effective asymmetry due to lower scattering in the high-Z medium. One example is pure silicon detectors, that can be used as a scatter medium and as a detector. These silicon detectors, when disposed in layers, can be used as trackers, enabling the reconstruction of the path of the pair and the measurement of its energy. For thick silicon trackers ($\sim$ 500 μm), the effective polarization asymmetry is low due to multiple scattering. Higher sensitivities to polarization are expected from thin silicon detectors ($\sim$ 150 μm). Also in [20], it is studied the set of variables that provide a higher sensitivity to polarization, or higher A_{eff}. These include the pair plane azimuthal angle, w, and the bisector angle, defined as $\phi = (\varphi_+ + \varphi_-)/2$. It is shown that the bisector angle is the variable that provides a higher A_{eff}.

An alternative solution to minimize the multiple scattering of the pair is to use detectors of low-density such as gas detectors. The HARPO (Hermetic ARgon POlarimeter) detector is a project that aims to characterize the TPC (Time Projection Chamber) technology as a MeV - GeV telescope and polarimeter [21]. It is a gaseous TPC filled with a mixture of argon and isobutane (95:5), capable of operating up to 5 bar. More details of the HARPO detector can be found in figure 2.7. Laboratory measurements in a polarized γ-ray beam provided an asymmetry, at 11.8 MeV, of $A_{eff}^{beam} = 0.074 \pm 0.006$, while the simulated and theoretical values are $A_{eff}^{sim} = 0.103 \pm 0.006$ and $A_{eff}^{theo} = 0.164 \pm 0.007$ [22].

2.2 Compton telescopes

A Compton telescope is an apparatus that estimates the origin of the detected photons through Compton scattering. Due to the nature of the events, when carefully designed, they can be used as imagers, polarimeters and spectrometers. The imaging capabilities are described in the following subsection. These instruments can be used as polarimeters if they are made of fine-

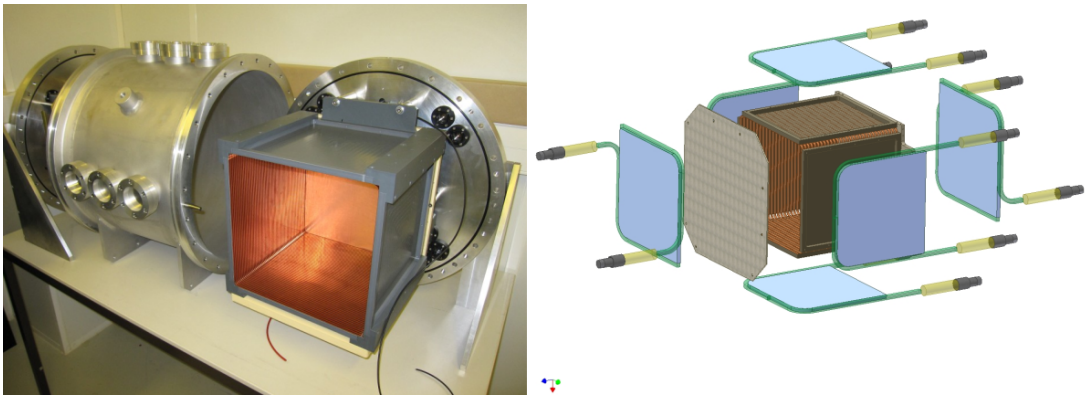

Figure 2.7: On the left it is presented the HARPO TPC demonstrator and an aluminum system that houses the detector. On the right it is presented a sketch of HARPO. The HARPO detector [21, 22] is a cubic gas detector with a side length of 30 cm. It is surrounded by 6 scintillator plates that provide a trigger of the instant when a particle interacts with the gas. The light yielded by each scintillator is collected by two Photomultiplier Tubes (PMTs). In a pair production event, it is produced an electron and a positron with high kinetic energy. As they travel through the gas, they ionize and excite the medium, producing a track. The electrons resulting from the ionization are drifted, through an electric field, to the readout plane. By knowing the drift velocity of the electrons, at the operation conditions, and the initial trigger time, the Z-coordinate can be estimated. The HARPO detector uses 2 GEMs and a Micromegas (Micro-Mesh Gaseous Structure) as an amplification stage, and the readout is performed with two series of copper strips, with 1 mm pitch, perpendicular to each other. Adapted from [21].

segmented or pixelated detectors, capable of detecting double events, i.e., the initial position of the Compton scattering, and the position of the absorption of the scattered photon (or the position of a second Compton scattering, if it is the case). Spectroscopy is achieved by measuring the energy deposited in the detectors for each event. In the following subsections is discussed the working principle of Compton telescopes and their limitations.

2.2.1 Origin of the detected photons

Classical Compton telescopes are composed of at least two detector elements in different planes, working as scatterers and absorbers [23]. A single detector plane can be also used as a Compton telescope, at the expense of double event detection efficiency.

The initial energy of the photon, E_i, can be computed by the sum of the energy deposited in the scatterer, E_e, and in the absorber, E_g: $E_i = E_g + E_e$ (assuming that the photon was completely absorbed) and the scattering angle can be computed by the Compton equation (equation 2.7). This results in a range of possible directions of incidence, which can be represented by a cone-like shape (see figure 2.8). In Compton telescopes, if the direction of the recoil electron is measured, the scattering angle of the electron can be computed through Compton kinematics, resulting in another cone that superimposes with the first, resulting in a arc-like distribution. Detailed information about these processes can be found in [18].

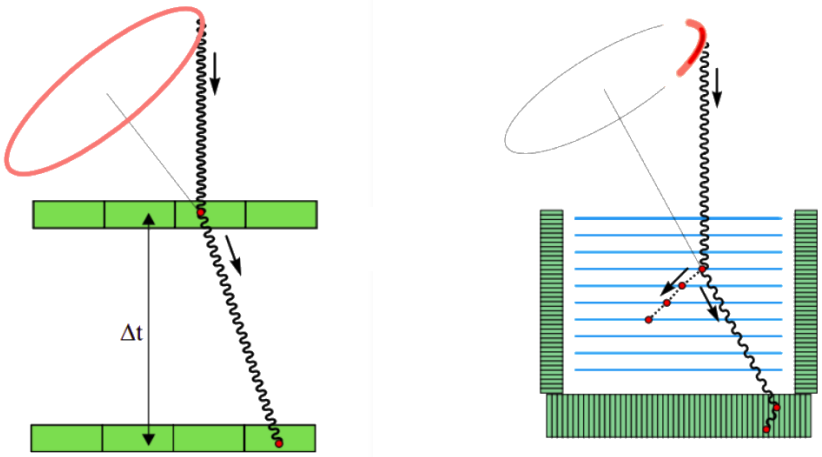

Figure 2.8: Determination of the original direction of the photon in Compton telescopes. Using the Compton kinematics, if the direction of the recoil electron is not measured, the incidence direction of the photon is restricted to a cone (left). If the direction of the recoil electron is measured, the cone may be restricted to an arc-like distribution (right). If more than one photon interacts in the instruments through Compton scattering, the direction of the source can be estimated. Adapted from [18].

2.2.2 Angular resolution

The angular resolution measure (ARM) is the smallest angular distance between the Compton cone and the origin of the photon [18]. The distribution of the ARM values, for a large number of scattered photons, allows the characterization of the angular resolution of the telescope, providing an uncertainty for the computed direction of the incident photons (see figure 2.9).

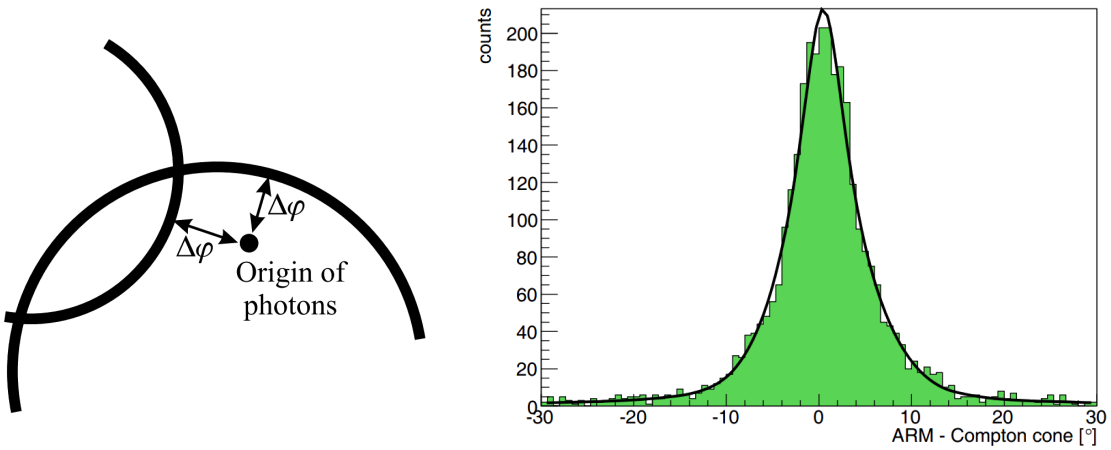

Figure 2.9: On the left is presented a schematic of a cross-sectional view of the Compton cones, the origin of the photons and of the ARM. On the right is presented the ARMs of the simulated 710 keV photons, detected with the MEGA instrument (section 2.4.5). The FWHM (full width at half maximum) of the ARMs distribution defines the angular resolution of the instrument and is usually determined as a function of the energy of the photons. Adapted from [18].

There are several factors that may affect the ARM: the stochastic nature of energy deposition in materials; the abrupt changes in the direction of energetic electrons, due to multiple scattering as they travel through matter; the energy lost via *bremsstrahlung*; the incomplete absorption of the recoil electron or photon; and the assumption that the interaction of the incident photon is given with a free electron at rest.

The first effect can be mitigated using detectors with good energy resolution. Also, radiative losses can be minimized using detectors with low Z [14]. The incomplete absorption of recoil electrons and photons can be reduced by increasing the volume of sensitive material, or by using detectors of high Z. The latter effect is known as *Doppler-broadening*. In reality, the collision of the photon is most likely given with a bound electron with non-null momentum and total energy different from its rest-mass energy. This effect constrains the angular resolution of Compton telescopes.

Zoglauer [24] computed the Doppler-broadening through Monte Carlo simulations for different elements, showing that the angular resolution worsens with increasing Z, and with a high scattering angle, θ. A summary of his results is shown in table 2.2 and figure 2.10.

Table 2.2: Doppler-broadening for different materials. The materials presented in the table are used in the AMEGO instrument (see section 3.3). These values are obtained from [24].

Material	Si	CdZnTe	CsI
FWHM at 200 keV [deg]	1.80	3.50	2.95
FWHM at 500 keV [deg]	0.80	1.55	1.25
FWHM at 1000 keV [deg]	0.40	0.85	0.75

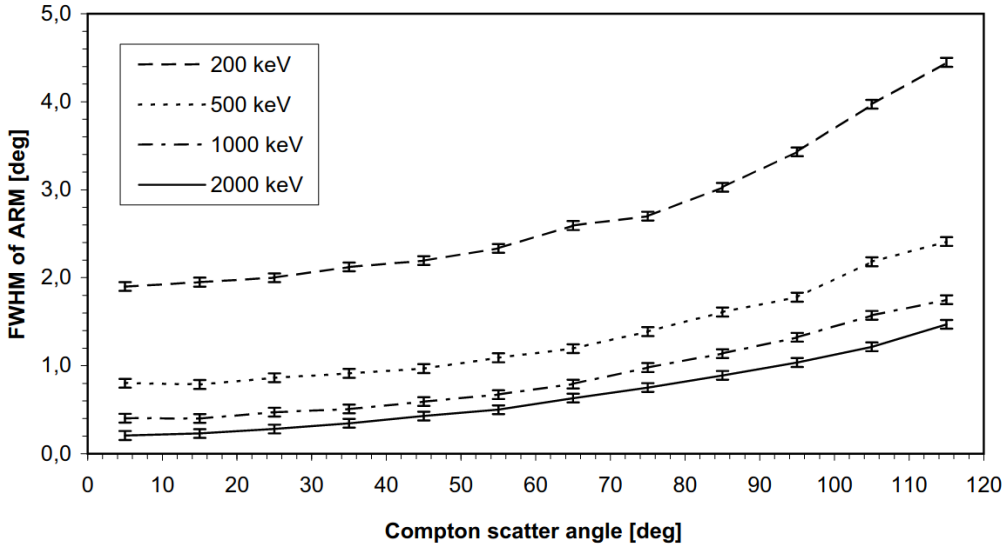

Figure 2.10: Dependence of the angular resolution as a function of the scattering angle, for germanium, at 200, 500, 1000 and 2000 keV. Figure from [24].

2.3 Polarization measurements - Compton scattering

Polarization measurements of X and γ radiation are based on the anisotropic distribution of the scattered particles from the interaction of the radiation with the medium. As mentioned in previous sections, in the photoelectric effect the electrons are more likely to be ejected in the direction of the electric field of the photon. In Compton scattering, the scattered photons are more likely to be scattered through the orthogonal direction to the electric field, and in pair production, the pairs are preferably emitted in the direction of the electric field of the photon.

In the following subsections are introduced parameters that help characterize the sensitivity to polarization of X and γ-ray detectors, and it is discussed the physical limits of the measurements. Methods to analyse the data recorded by detectors for polarimetry analysis, will be presented.

2.3.1 Modulation factor

The *polarimetric modulation factor*, Q, is a parameter that characterizes the response of a detector system to polarized radiation [1], through the measurement of the anisotropy of the azimuthal scattering distribution of the Compton events. It can be computed experimentally or through simulations with the following expression:

$$Q = \frac{N_\perp - N_\parallel}{N_\perp + N_\parallel}, \tag{2.15}$$

where $N_\perp$ and $N_\parallel$ are the number of counts from detectors positioned in the orthogonal and parallel direction to the polarization vector of the photons, respectively.

Replacing $N_\perp$ and $N_\parallel$, with the Klein-Nishina differential cross-section for polarized photons (equation 2.11), scattered in the azimuthal angles $\phi = 90°$ and $\phi = 0°$, respectively, results in:

$$Q = \frac{d\sigma(\phi = 90°) - d\sigma(\phi = 0°)}{d\sigma(\phi = 90°) + d\sigma(\phi = 0°)}, \tag{2.16}$$

which yields:

$$Q = \frac{\sin^2(\theta)}{\epsilon^{-1} + \epsilon - \sin^2(\theta)}. \tag{2.17}$$

In figure 2.11 it is plotted the maximum attainable, or ideal, modulation factor as a function of the scattering angle for different energies. It can be observed that, as the energy of the photons increases, the maximum modulation factor decreases, and that the maximum is shifted for lower scattering angles. Also, if the photon is backscattered ($\theta = 180°$), or scattered with a low angle ($\theta \approx 0°$), no polarimetric measurements can be performed as the photons carry no polarization information. In the keV energy range, the highest modulation factor is attained for photons that are scattered approximately at right angles.

The degree of linear polarization of a given flux can be obtained by [1]:

$$\Pi = \frac{Q}{Q_{100}}, \tag{2.18}$$

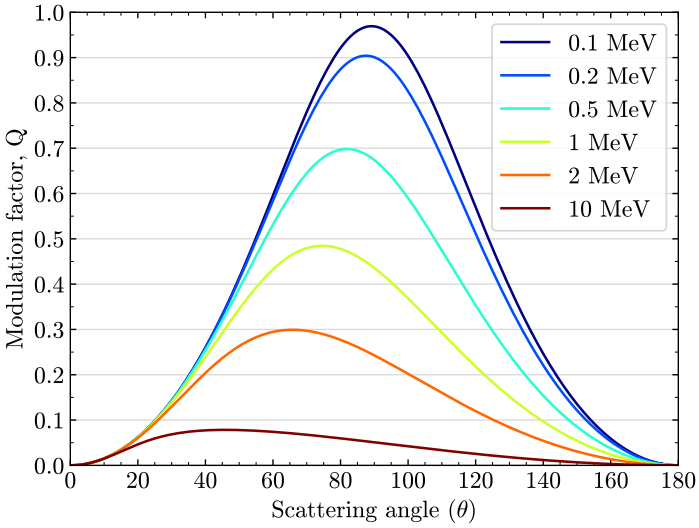

Figure 2.11: Maximum polarimetric modulation factor as a function of the scattering angle for different energies. In real instruments the modulation factor is lower, but highly dependent on the geometry of the detectors.

where Q is the measured modulation factor and Q_{100} is the modulation factor measured for a 100% polarized flux. The polarimeters must be calibrated for a 100% polarized source, at different energies, in order to measure Π.

Some scientific missions are equipped with γ-ray detectors that, initially, were not designed as polarimeters. Some of these detectors, despite not being calibrated in laboratory, have the potential to perform polarimetric measurements. This requires an estimation of the Q_{100} through Monte Carlo simulations, as was the case with COMPTEL and INTEGRAL [6, 25].

2.3.2 Radial bin technique

The *radial bin technique* (RBT) is described by F. Lei et al. in [1]. It consists in constructing a displacement plane (explained in figure 2.12) and dividing it in a number of equal sized radial bins. With a histogram of the number of counts per radial bin (also referred as *polarigram* [26]), the data is fitted to equation 2.19, from where the polarization angle of the photon and Q can be extracted.

$$N(\phi) = P_1 \cos\left(2(\phi - P_2)\right) + P_3 \tag{2.19}$$

In equation 2.19, ϕ is the angle that corresponds to each bin from the histogram. It usually ranges from 0 to 2π, but when the statistics are low, some authors [3, 26] take advantage of the π-symmetry of the differential cross-section and join the π-symmetric bins in order to improve the signal-to-noise ratio. The polarization angle of the photon, ϕ_0, is directly obtained from P_2, and the modulation factor from $Q = \frac{P_1}{P_3}$.

In [28] it is shown, through Monte Carlo simulations, that the modulation factor can be increased by excluding the central pixel of the displacement plane, and by excluding the first and second order pixels around the central pixel, i.e. excluding the pixels around central pixel.

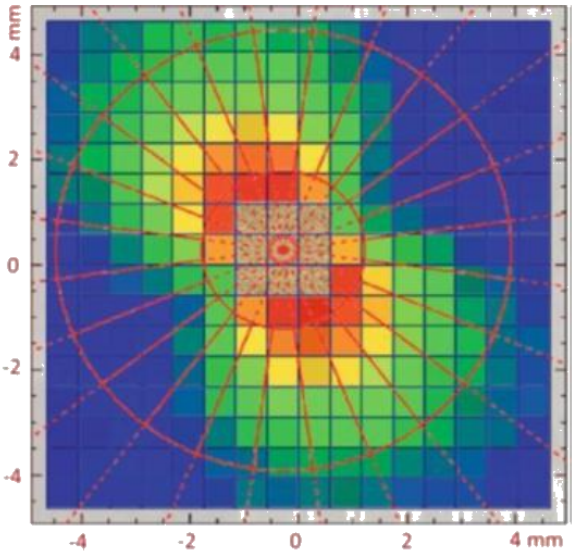

Figure 2.12: Displacement plane obtained with a 200 keV collimated beam, with a degree of linear polarization equal to 98%, polarized at 30°, that irradiated the central pixels of the detector Caliste 256 [27]. A displacement plane consists of a map that represents the distance, in the X-axis and Y-axis, between two Compton interactions [1]. As only the central pixels were irradiated, the displacement plane can be directly obtained by the number of counts in each pixel. The Caliste 256 consists of a spectrometer with 16×16 pixels and a sensitive area of ~ 1 cm^2, that can be equipped with a CdTe or a CZT detector. It is able to detect photons with energy between 2 and 280 keV, with a resolution of 1 keV at 60 keV.

The simulations were performed for a pixelated CdTe detector. With a second order suppression, the modulation factor increased from around 0.3 to 0.5, in the 200 - 400 keV range. This is due to the better angular distribution obtained for the scattered photons inside pixels that are more distant from the central pixel. By applying this filter the polarization sensitivity increases, but reduces the efficiency of double event detection.

For faint sources it may be advantageous to optimize the efficiency, and for very intense sources it may be preferable to filter some events and obtain a better modulation factor, at the expense of the efficiency.

2.3.3 Systematic error corrections

For an unpolarized beam irradiation, it is expected a uniform azimuthal distribution of the Compton scattered photons. In real detectors this is not the case, as may exist inconsistencies in the geometrical layout of the detector plane. For example, in cubic detectors, the diagonal directions are longer than the straight counterparts, therefore more events will be detected in these directions. As the azimuthal distribution of events is dependent on the detector geometry, these distributions can lead to false results of the parameters extracted from the fit to the polarigram (ϕ_0 and Q).

The non-uniformities can be minimized using the response of the detector to unpolarized photons [1], as follows:

$$N_{true}(\phi) = \frac{N_{pol}(\phi)}{N_{non}(\phi)} N_{max}, \tag{2.20}$$

where $N_{true}(\phi)$ is the corrected azimuthal distribution of the events, $N_{pol}(\phi)$ and $N_{non}(\phi)$ are the distribution of polarized and unpolarized events, respectively, and N_{max} is the maximum value of $N_{non}(\phi)$.

In figure 2.13 it is presented a polarigram of the COMPTEL response to polarized radiation, obtained through simulations, for an irradiation on-axis, i.e., photons with a direction perpendicular to the plane of the detector. From the figure, it can be observed the effectiveness of the correction of equation 2.20.

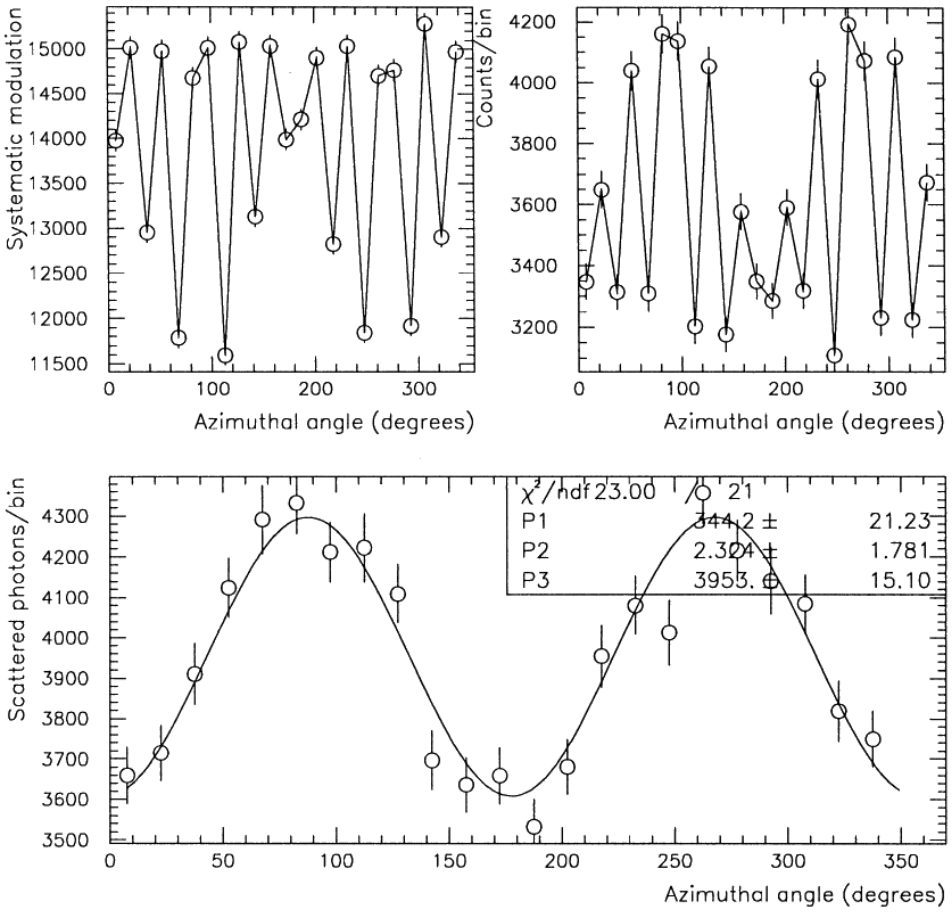

Figure 2.13: Azimuthal distribution of scattered photons, detected with COMPTEL [25]. This data was acquired through simulations, with a source of 1 MeV photons, on-axis. The top-left distribution is due to non-polarized photons, the top-right is due to 100% polarized photons, and at the bottom is presented the corrected distribution, obtained through equation 2.20.

2.3.4 Off-axis incidence of photons

For observations carried with off-axis sources, an artificial modulation is introduced, as shown in [25, 28].

This pseudo-polarimetric response can be removed by transforming each point of the displacement plane into a new displacement plane, normal to the incident photon direction, by

applying the system of equations 2.21, followed by the method of equation 2.20 [1].

$$\begin{cases} \Delta X' = (\Delta X \cos(\alpha) + \Delta Y \sin(\alpha)) \ \cos(\beta) - \Delta Z \sin(\beta) \\ \Delta Y' = \Delta Y \cos(\alpha) - \Delta Y \sin(\alpha) \\ \Delta Z' = (\Delta X \cos(\alpha) + \Delta Y \sin(\alpha)) \ \sin(\beta) - \Delta Z \cos(\beta) \end{cases} \tag{2.21}$$

In the system of equations 2.21, α and β are the azimuth and zenith angles of the direction of the source, respectively, ΔX, ΔY, ΔZ are the displacement coordinates of the instrument and $\Delta X'$, $\Delta Y'$, $\Delta Z'$ are the displacement coordinates in which the Z' axis is the direction of the incident photon and the X' axis is in the X - Y plane of the telescope coordinates.

2.3.5 Minimum detectable polarization

The *minimum detectable polarization* (MDP) is the main parameter to assess the polarimetric sensitivity of an instrument. It provides the minimum degree of linear polarization that an instrument can measure with the observation time.

The MDP, for a 99% confidence level, is given by [1]:

$$MDP_{99\%} = \frac{4.29}{A\,\varepsilon\,S_F\,Q_{100}} \sqrt{\frac{A\,\varepsilon\,S_F + B}{\Delta t}}, \tag{2.22}$$

where A is the sensitive area, ε is the efficiency of the detectors, S_F is the flux of the source (photons s^{-1} cm^{-2}), B is the background flux (photons s^{-1}) and Δt is the observation time.

F. Lei et al., in [1], refers the following considerations regarding observations in the presence of background radiation. Most astronomical observations are dominated by background noise, which highlights the importance of minimizing the background contribution to the signals. The effect of the background translates into a reduction of Q, as the parameter P_3, from equation 2.19, will contain the background contribution. This effect can be reduced with systematic error corrections by measuring the distribution of the background radiation on the operating site, with an on/off observation strategy or by detailed modeling.

Residuals on the background distribution will also reduce Q by contributing with a pseudo-modulation.

M. Bagheri et.al [29] shows that in an ideal case, with no background radiation and a detection efficiency of 100%, the minimum number of counts required to achieve a certain MDP is given by:

$$S = \left(\frac{4.29}{Q_{100} \times MDP_{99\%}} \right)^2. \tag{2.23}$$

In this case, 7400 photons are required in order to achieve a MDP of 10%, for a detector with a Q_{100} of 0.5, for example.

2.4 Astronomical Compton polarimeters

In this section are presented past and current instruments capable of performing polarimetric measurements of astronomical sources, through Compton scattering. Some of these instruments operate as dedicated polarimeters, while others were designed for imaging and spectroscopy, but are capable of performing polarimetry due to their geometry. A summary of scientific contributions of the instruments is also provided.

2.4.1 COMPTEL

The Imaging Compton Telescope (COMPTEL) is an instrument that flew on board of the Compton Gamma-Ray Observatory (CGRO), which orbited Earth from 1991 to 2000. It provided images of the sky in the gamma-ray energy range through Compton scattering kinematics. It operated in the 0.75 - 30 MeV energy range, with a *field of view* (FOV) of 1 sr and an angular resolution of $\sim 1^{\circ}$ [1].

The COMPTEL is decribed in [1] and its schematic is presented in figure 2.14. It is composed of two layers of detectors separated by 1.5 m. The upper layer consists of seven cylindrical containers with a low-Z liquid scintillator. The yielded light is measured by eight PMTs, which allow the determination of the location of the interaction using centroid techniques, with a position resolution between 1 and 2 cm. The lower layer consists of fourteen NaI(Tl) crystal scintillators with a cylindrical shape. The light yielded by each crystal scintillator is collected by seven PMTs, resulting in a position resolution between 1.5 and 3 cm. The total sensitive area of the top and bottom layer is 4188 and 8620 cm^2, respectively. Despite the large detection area, the probability of a photon interacting in both layers is low, resulting in a combined effective area between 10 and 20 cm^2 for photons with energies between 1 and 5 MeV [1].

COMPTEL was not designed to work as a polarimeter, however polarimetric analysis can be performed through the azimuthal distribution of the scattered photons. As it was not optimized for polarimetric measurements, several factors affect its performance, for example, the large distance between the first and second layer, which results in the detection of scattered photons with low angles, resulting in a modulation factor substantially lower than the maximum modulation factor theoretically possible [1].

The polarimetric performace of the COMPTEL was evaluated through Monte Carlo simulations [25]. The modulation factor varies between 0.1 and 0.03 between 1 and 10 MeV. The MDP from a 1 Crab source, for an observation time of 14 days in the energy range of 750 - 1125 keV, is 29.5% [1].

2.4.2 INTEGRAL

The INTErnational Gamma-Ray Astrophysics Laboratory (INTEGRAL) is a satellite loaded with instruments capable of performing fine spectroscopy and imaging, of celestial gamma-ray

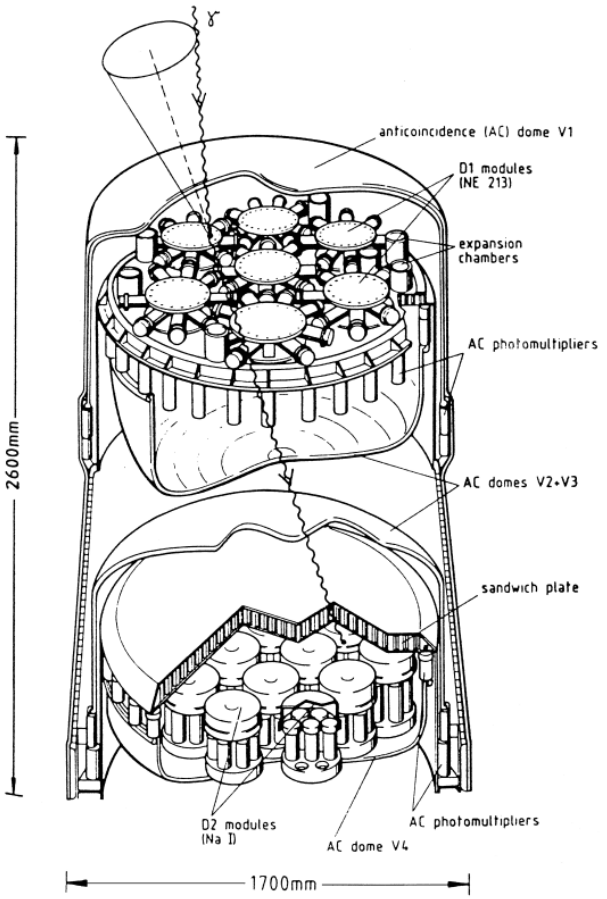

Figure 2.14: Schematic of the COMPTEL instrument. Ideally, a γ-ray goes through Compton scattering in the first layer and through photoelectric absorption in the second layer. By measuring the energy deposited in each layer, and the angle of the scattered photon with relation to the instrument axis, it is possible to determine the direction of the incident photon through the Compton kinematic equations. Through the azimuthal distribution of the scattered photons, polarimetric measurements can be performed. Figure from [1].

sources, in the 0.15 - 10 MeV energy range [1]. It was launched in 2002 and it is still in operation. Despite not being designed as a polarimeter, or calibrated to perform polarimetry, it is sensible to polarization due to its detectors geometry.

Its main instruments, sensible to polarization, are the IBIS (Imager on-Board the INTEGRAL Satellite) and the SPI (SPectrometer of INTEGRAL). In [1], these instruments are described and its polarimetric performance is estimated through simulations.

The IBIS, presented in figure 2.15, consists of two layers of pixelated detectors, separated by ~ 10 cm. The first layer is made of a total of 16384 CdTe detectors, of size $4 \times 4 \times 2$ mm^3. The bottom layer is made of 4096 CsI bar-shaped scintillators, optically isolated from each other. The size of each scintillator is $8.7 \times 8.7 \times 30$ mm^3. The light yielded by each scintillator is measured by a photodiode. Both layers are surrounded by a BGO (Bismuth Germanate, $Bi_4Ge_3O_{12}$) crystal block, with a thickness of 20 mm. The BGO crystal works as an active shield, contributing to a reduction of the background noise.

The SPI is a spectrometer dedicated to measuring high-resolution energy lines in the 0.2 - 8 MeV energy range. It consists of 19 closely packed hexagonal Ge bars, with a side of 3.2 cm and height of 7 cm. The SPI is also surrounded in all directions with BGO crystals, except the direction of the field of view.

Due to the pixelated geometry, these detectors can work as polarimeters. In [1] it is shown, through simulations, that the modulation factor of IBIS is 0.30 in the 200 - 500 keV energy range, falling to 0.04 in the 2 - 5 MeV energy range. The SPI modulation factor is 0.17 and 0.04, for the mentioned energy ranges. It is also shown that for an exposure time of 10^6 s ($\sim$ 12 days), the MDP for the Crab nebula is 2% and for the Crab pulsar is 11%.

Between 2003 and 2007, the INTEGRAL observed the Crab Nebula for a total of 1.2×10^6 s. It was determined that, in the 200 to 800 keV energy range, there is no significant polarization in the pulsed peaks, which are dominated by the pulsar emission, and that the off-pulse intervals, which are dominated by emissions from the nebula, present a polarization fraction of >0.72, and that the overall polarization fraction is $0.47^{+0.19}_{-0.13}$, with a 95% confidence level [6].

In 2006, INTEGRAL detected one of its most energetic GRBs, the GRB 061122. This GRB had a T_{90} duration of 12 s. It presented a polarization fraction of 0.6 and 0.33 at a 68% and 90% confidence level, respectively, in the 250 to 800 keV energy range [3].

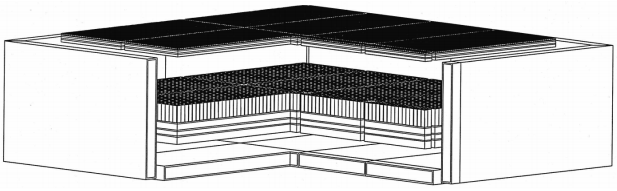

Figure 2.15: The IBIS instrument. It has two layers of detectors: the first consists of CdTe detectors and the second of CsI scintillators. It uses a coded mask to form the images in the hard X and γ-ray domain. Figure from [1].

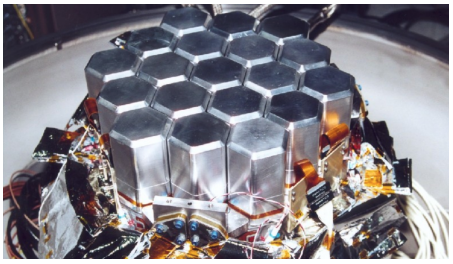

Figure 2.16: The SPI instrument. The instrument is composed of hexagonal germanium bars. It provides good energy resolution, but requires cooling. Figure from [30].

2.4.3 PoGoLite Pathfinder

The Polarised Gamma-ray Observer - light-weight version (PoGOLite) is a balloon-borne astronomical γ-ray polarimeter designed to observe celestial point sources with fluxes as low as 200 mCrab and with a narrow field of view of 1.25 msr [31]. The PoGOLite Pathfinder is a version of the previous instrument, with a smaller effective area and lower sensitivity, which allows the observation of 1 Crab sources in the 25 - 240 keV energy range [32].

The PoGOLite Pathfinder scientific instruments are described in [31]. It consists of 61 hexagonal phoswich detector cells (PDCs) in a honeycomb configuration, and 30 side anti-coincidence shields (SAS) detectors that surround the previous instrument (see figure 2.17). The PDCs are described in figure 2.18.

The PDC is composed of four different elements: a thin-walled tube of slow plastic scintillator; a solid rod of a fast plastic scintillator; an anticoincidence BGO crystal; and a PMT.

The plastic scintillators are wrapped with a reflective layer, 80 μm thick, to maximize light collection, and the BGO scintillators are covered with epoxy loaded with reflective $BaSO_4$. The thin-walled tube scintillators are additionally covered with a 50 μm thick foil of lead and tin to provide additional passive collimation. The light yielded by each PDC is read by its corresponding PMT. The mean diameter of the PDC is 24 mm. The SAS are rods of BGO crystals, tightly packed around the PDC assembly, covering two thirds of the height of the PDCs scintillators. To each SAS is also applied a reflective layer of $BaSO_4$. The correlation between the SAS and the PDC hits allows for the rejection of background events.

In the PDC the incoming photons go through Compton scattering and photoelectric effect. Event selection can be performed by analyzing the interactions that occurred, as shown in figure 2.19, and polarimetric measurements can be made through the azimuthal distribution of the scattered photons.

In 2013, the 549 minutes PoGOLite Pathfinder balloon flight [32, 33], measured the linear polarization of hard X-ray emission from the Crab. The MDP for the observations is 28.4±2.2%. The degree of linear polarization was computed to be $18.4^{+9.8}_{-10.6}$ (1σ of uncertainty), with an upper limit, at a confidence level of 99%, equal to 42.2%.

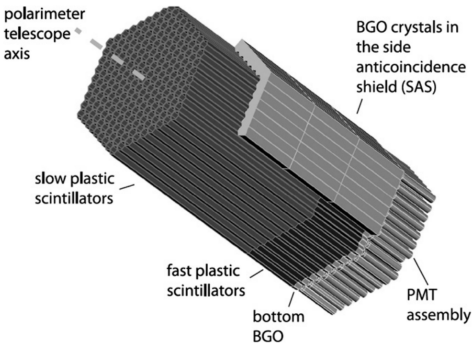

Figure 2.17: Overview of the PoGOLite instrument. The PoGOLite is composed of 217 PDCs, providing a higher sensitive area than its successor, the PoGOLite Pathfinder, which is composed of 61 PDCs. Figure from [31].

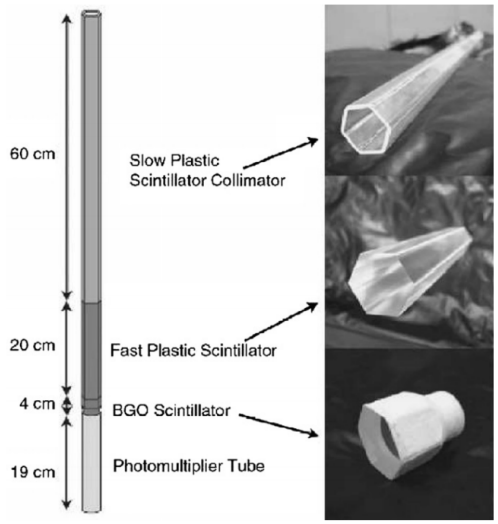

Figure 2.18: Elements of a PDC. A PDC is a detector composed of scintillators, with different pulse shape characteristics, coupled to each other and to a PMT. Each scintillator element is covered with reflective layers in order to create collimation and maximize the light collection. Figure from [31].

2.4.4 POLAR

POLAR is a dedicated polarimeter launched into orbit, in 2016, in a joint European-Chinese mission. It was placed on the Chinese Space Lab Tiangong-2 at a stable low-orbit, pointing

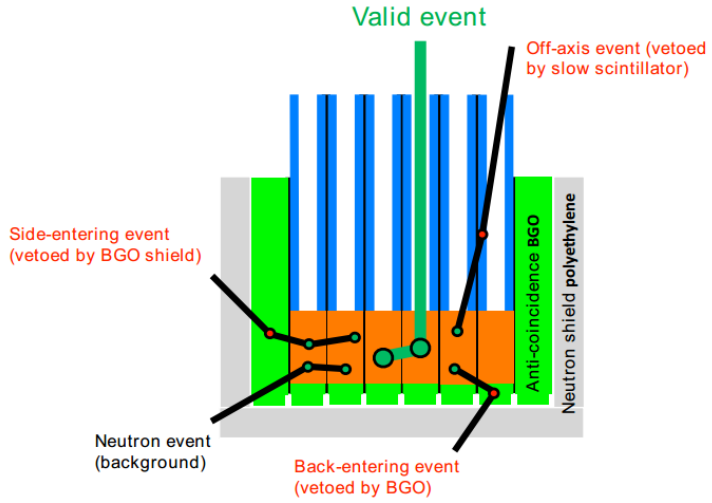

Figure 2.19: Diagram of the PoGOLite instrument, and possible interactions. Through the azimuthal scattering angle of the Compton scattered photons, the polarization degree of the incident beam, and its polarization angle can be determined. Figure from [32].

to the zenith [34]. It detected 55 GRBs during 3180 hours of data, 10 of which were bright enough to perform a polarimetric analysis [11, 34, 35]. After six months of data collection, the high voltage power supply showed some problems, ceasing further measurements. In 2019, the spacecraft Tiangong-2 made an atmospheric reentry, concluding the POLAR mission. A new mission, the POLAR-2, aims to be launched on board of the China space station in 2024. It provides an increase of the sensitive area by an order of magnitude. Also, the multi-anode photomultipliers (MAPMTs) will be replaced with silicon photomultipliers (SiPMs) [36].

The instrument is presented in figure 2.20. It is composed of 1600 plastic scintillator bars of a low-Z material, divided into 25 modular units. Each module is read by an Hamamatsu H8500, a MAPMT with 64 anodes with an area of 4.8×4.5 mm^2 [37]. The scintillator bars have 6×6 mm^2 of surface area, and a length of 176 mm. The bars are optically isolated from each other with a reflective foil, and are optically coupled to a MAPMT. Each module is composed of 64 bars. These are wrapped in a 1 mm thick layer of carbon fiber, which provides mechanical support and works as a passive shield for low energy charged particles and low-energy photons [38].

The instrument does not have a layer of veto sensors. The background rejection is based on the analysis of the generated signals. Some parameters, on which background rejection is based, are presented: the number of trigger channels; total energy deposition; and position of the signals, as the rate of signals generated by charged particles is higher in the peripheral bars.

The data size reserved for POLAR on Tiangong-2 was 40 GB/day, which allowed for a continuous data gathering [38].

POLAR has a high sensitivity (on average, 14% of the events fulfill the double energy deposition coincidence required by the trigger [39]), a large effective area of approximately 300 cm^2, and a field of view of approximately 1/2 of the sky [34].

Through the measurement of the position of the interactions, it is able to perform polarimetric studies in the 50 - 500 keV energy range [38]. The instrument was extensively characterized

with simulations, calibrated on ground with polarized beams and in orbit [34, 38, 39, 40]. The calibrations show that the instrument modulation factor varies aproximatelly between 0.22 and 0.34, between 60 keV and 110 keV [40]. The performance of the in orbit instrument was also studied, for example the modulation factor induced by the background radiation, as function of its position in the orbit [34].

As mentioned before, 10 out of the 55 GRBs, detected by POLAR, were bright enough to perform polarization analysis. The data acquired provides a MDP between 6 and 15% [35]. In [11], 5 of these 10 GRBs were studied. A summary of the results is presented in table 2.3. There were found low levels of linear polarization, but a time-segmented analysis shows that, for GRB 170114A (the brightest detected), the low polarization degree is explained by changes in the polarization angle overtime.

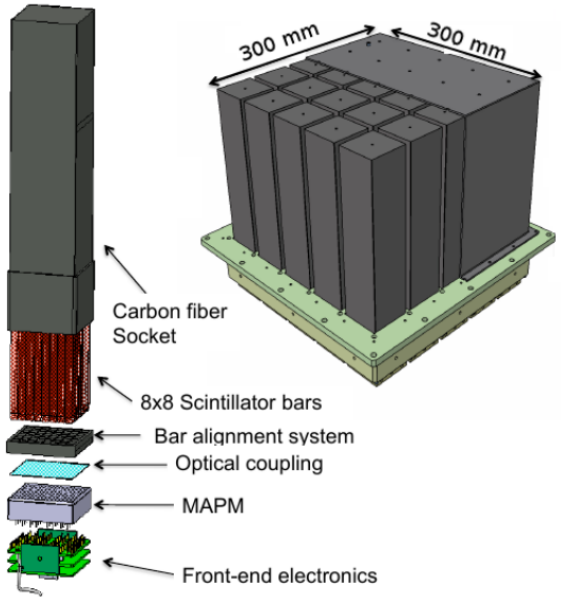

Figure 2.20: Diagram of POLAR. The sensitive volume corresponds to plastic scintillator bars, which have its yielded light measured by multi-anode photomultipliers, providing position resolution. Figure from [38].

2.4.5 MEGA

The Medium Energy Gamma-ray Astronomy (MEGA) telescope [41] is a Compton and pair telescope concept, that aims to provide a medium-energy all-sky survey in the 0.4 - 50 MeV energy range. The instrument would cover the sensitive gap that currently exists in the MeV range. A prototype was built and calibrated in laboratory, at the HIGS from Duke University and aimed to fly in a balloon mission, to prove the capabilities of background rejection [18]. MEGA never got materialized as a mission, but contributed with conceptual and practical developments for future instruments that intend to cover the MeV range [2].

The MEGA prototype, presented in figure 2.21, is described in [18, 41]. It is composed of a scatterer/converter/tracker, calorimeters and a surrounding anti-coincidence shield (ACS) [18]. The first operates as a Compton scattering and pair production medium, and can be used

Table 2.3: Polarimetric study of 5 GRBs, detected by POLAR during its operation [11]. T_{90} corresponds to the time interval over which 90% of the total background-subtracted counts are observed, Π is the polarization degree, Π_{up} is the 99% confidence upper limit in Π, and ϕ is the polarization angle. The fluence is given in the 10 to 1000 keV energy range.

GRB	T_{90} (s)	Fluence (10^{-5} erg cm^{-2})	Π (%)	$\Pi_{up\,99\%}$(%)	ϕ (°)
161218A	6.76	1.25	9	45	40
170101A	2.82	1.27	8	31	164
170127C	0.21	0.74	11	67	38
170206A	1.2	1.34	10	31	106
170114A	8.0	1.93	4	28	164
170114Ap1	NA	NA	15	43	122
170114Ap2	NA	NA	41	74	17

to reconstruct the track of scattered electrons and of pair products. It consists of 11 layers, separated by 1 cm, of 0.5 mm thick double-sided silicon strip detectors (DSSD). Each layer consists of 3×3 wafers with 6×6 mm^2 sensitive area. The strips of the DSSD wafer have a pitch of 0.47 mm. The calorimeters cover the lower hemisphere of the tracker. It is made up of 20 modules of 10×12 CsI(Tl) scintillator bars, with an area of 5×5 mm^2 and a thickness of 8, 4 and 2 cm, depending on the position their placed (the thicker calorimeters are placed at the bottom). The CsI bars are separated by a reflective paper and are coupled to photodiodes. The calorimeters are used to stop and measure all secondary particles, i.e., the Compton scattered photons, and the electrons and positrons originated in pair production. The ACS encloses the previous detectors. It consists of 1.27 cm thick BC-412 plastic scintillators and wavelength-shifting fibers which propagate the light to PMTs. It contributes with the ability to reject charged-particle events, of solar and cosmic origin, as well as charged-particles trapped in the magnetosphere of the earth, improving the signal-to-background ratio.

At the HIGS facility, the measurements were performed with a monoenergetic 100% polarized γ-ray beam. The test campaign provided a modulation factor of 0.17 at 0.71 MeV, 0.12 at 2 MeV and 0.06 at 5 MeV, which agrees with the simulated values [18].

2.5 The Medium-Energy Gamma-ray Astronomy library

The Medium-Energy Gamma-ray Astronomy library (MEGAlib) [42] is a set of software tools designed to simulate and analyse the data from γ-ray detectors. The MEGAlib toolkit was developed alongside the MEGA telescope [42]. The software specializes on Compton telescopes, but can be used for simulating a variety of detectors and high-energy particles. It can also be applied to medical imaging detectors.

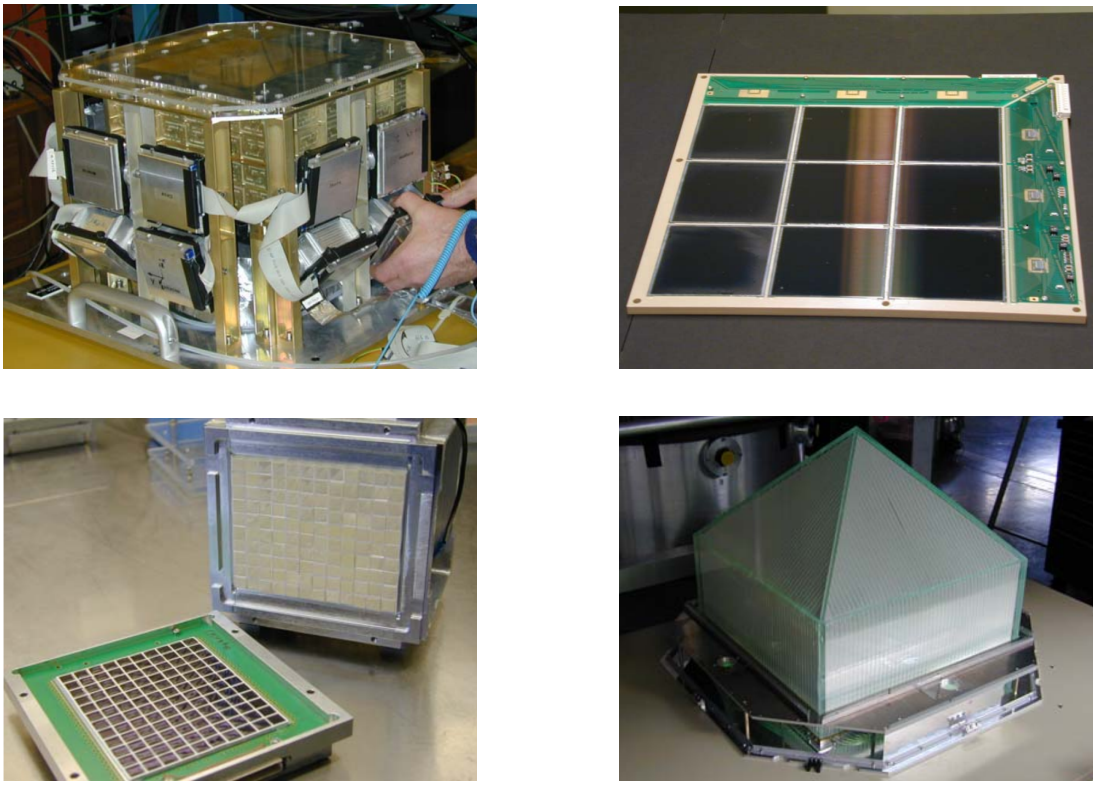

Figure 2.21: On the top-left it is presented the MEGA prototype. It is composed of 11 layers of DSSD wafers and 20 calorimeter modules. At the top-right it is presented a layer of the tracker. It is composed composed of 3×3 DSSD wafers and the associated electronics. At the bottom-left it is presented a calorimeter module. It is composed of 120 CsI bars, each bar coupled to a photodiode. At the bottom-right it is presented the ACS. Adapted from [18].

MEGAlib is a C++ object oriented software, based on ROOT and Geant4. The main tools of MEGAlib are the Geomega, Cosima, Revan and Mimrec. Instructions for the MEGAlib instalation, as well as the manuals for the Geomega and Cosima can be found at the MEGAlib website[1].

Geomega (Geometry for MEGAlib) is the library from where the geometries, materials, detectors and trigger criteria can be defined. These are defined in an ASCII file, with an object oriented syntax. For example, a cuboid pixel of CdTe (here denominated as finger) can be defined as:

// Build a single CdTe finger: $0.2 \times 0.2 \times 1$ *cm*
Volume CdTe_finger
CdTe_finger.Shape BRIK 0.1 0.1 0.5
CdTe_finger.Material CdTe ,

and its properties as a detector, as:

[1] https://megalibtoolkit.com/home.html

```
// Define the properties of a detector and associate it with a volume
Calorimeter CdTe_calorimeter
CdTe_calorimeter.SensitiveVolume CdTe_finger
CdTe_calorimeter.TriggerThreshold 30
CdTe_calorimeter.EnergyResolution Gauss 100 100 2
CdTe_calorimeter.EnergyResolution Gauss 1000 1000 5 .
```

A detector plane, consisting of 16 × 16 pixels, can be defined as:

```
// Volume that contains 16 × 16 fingers
Volume CdTe_matrix
CdTe_matrix.Shape BRIK 1.6 1.6 0.5
CdTe_matrix.Material Vacuum
// Place the CdTe fingers into the volume
For I 16 -1.5 0.2
   For J 16 -1.5 0.2
      CdTe_finger.Copy CdTe_finger_%I_%J
      CdTe_finger_%I_%J.Position I J 0.0
      CdTe_finger_%I_%J.Mother CdTe_matrix
   Done
Done .
```

Examples of detectors classes are: strip detectors, scintillators, calorimeters, Anger-cameras, etc.

The geometries and detector properties are defined in files with a .geo and .det extension, and the files where the detectors are defined in a single volume, assembling the instrument, and where the sources and triggers are defined have the .setup extension.

Cosima (Cosmic Simulator for MEGAlib) is the MEGAlib simulator, based on Geant4. It uses the geometries and detector properties defined in Geomega. The Cosima manual contains the information needed to configure the radiant sources. Similarly to Geomega, these are also defined with an object oriented syntax. For example, it is defined the particle type, the spectrum, the flux, the beam type (”FarFieldPointSource”, ”PointSource”, ”ConeBeam”, etc.), among other properties. The beam type ”FarFieldPointSource” is particularly useful for determining the modulation factor of a given instrument (see figure 2.22), as the particles have a well defined direction. The simulation files have the .sim extension.

Revan (Real Event Analyzer) is the software responsible for the reconstruction of events. It can be used with simulated and measured data. It can be used for reconstructing single site events, Compton scatter, pair production and high-energy charged particle events. Revan specializes in the Compton events reconstruction, determining the Compton interaction sequence and, when possible, the Compton electron track.

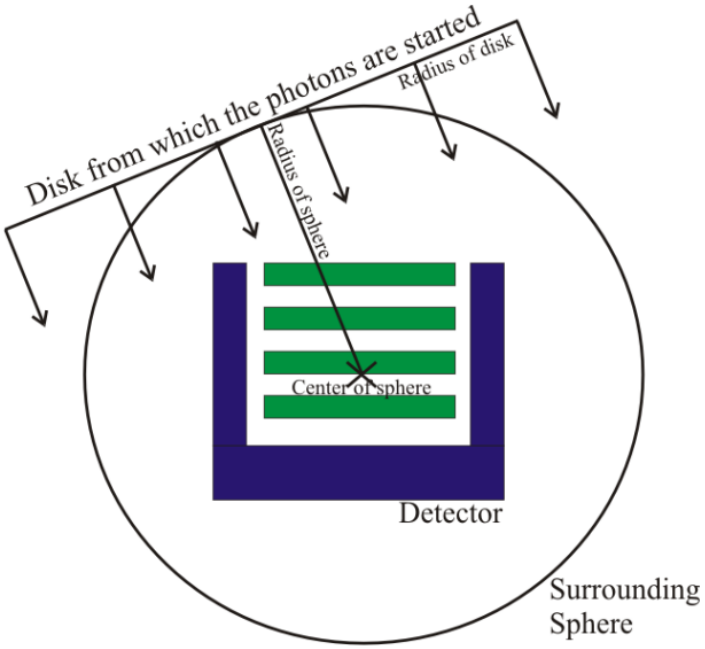

Figure 2.22: The far-field point source beam simulates particles originated from a distant source. The particles are originated from a disk, which has the same radius as the sphere, tangent to a surrounding sphere. The position of the disk, in the surrounding sphere, can be defined with a polar and azimuth angle. The dimensions of the surrounding sphere and the position of the disk, are defined in Geomega. The particles have the same direction, which is defined by the center of the disk and the center of the sphere. The start position of the particles have a random position on the disk.

Mimrec (MEGAlib image reconstruction) is MEGAlib's high-level data analyzer. It can be used to perform selection of events, reconstruction of images, obtain energy spectra, ARM distributions and, among other options, perform polarization measurements, applying off-axis and systematic error corrections.

3

The AMEGO mission

In this chapter the AMEGO mission is presented. The requirements and objectives of the mission are briefly described, highlighting the most relevant ones related to high-energy astrophysics polarimetry. The AMEGO scientific instrument and its operational performances characteristics are also described. The efficiency and modulation factor of the instrument, as a function of the energy of the photons, is characterized through simulations in this chapter. It is also studied which detectors contribute the most to the modulation factor and efficiency and it is evaluated the effects of event selection, based on the scattering angle of the first Compton interaction. The sensitivity of the instrument to polarization is determined, estimating the background rates in its operation conditions and computing the MDP for astronomical sources.

In the remainder of the chapter, it is presented the AMEGO-X, an instrument version for the NASA MIDEX call, as well an estimation of its efficiency, modulation factor, background rates and MDP for the same astronomical sources.

3.1 Overview and framework

The All-sky Medium Energy Gamma-ray Observatory (AMEGO)[1] [43, 44, 45] is a probe-class mission[2] concept that operates as a Compton-pair telescope. AMEGO aims to contribute to the multi-messenger astrophysics, helping understand GWs, GRBs, active galactic nuclei and element formation in extreme conditions such as supernovae [45], in a mission with a duration of at least 5 years [43]. The mission concept was submitted to the Astro2020 Decadal Survey [43]. Currently, the AMEGO team consists of more than 200 scientists from 15 countries [44].

The AMEGO mission originated from the ComPair (Compton-Pair Production Space Telescope), a MIDEX[3] proposal which consisted in a smaller version of AMEGO and did not include the low-energy calorimeter (see section 3.3). Due to a projected cost higher than a MIDEX cost cap, the mission was rethought for a probe-class mission. The ComPair now referes to the

[1] https://asd.gsfc.nasa.gov/amego/

[2] A probe-class mission is a NASA class mission, which cost ranges between the cost of a MIDEX mission and of a large mission, capping at about $1B.

[3] A MIDEX (Medium-Class Explorer) is a NASA class mission. It is included in the heliophysics and astrophysics explorer missions. Its price cap is $200M.

AMEGO prototype that is currently being built and will be tested in 2021, at the HIGS facility from Duke University [45]. In the fall of 2022, the prototype will go through a balloon flight.

The AMEGO instrument presents technical maturity, as its detectors and associated electronics, except the low-energy calorimeter, have flight heritage from missions such as the Fermi-LAT and INTEGRAL, among others [43].

Currently, a concept of a smaller version of AMEGO, the AMEGO-X[4], is being developed and will be submitted to the 2021 Astrophysics Announcement of Opportunity, as a MIDEX mission. AMEGO-X is further discussed in section 3.5.

3.2 Summary of the mission requirements and objectives

AMEGO will cover the 200 keV to 10 GeV energy range, imaging the sky with a better sensitivity than previous instruments (see figure 3.1). It will contribute to the MeV astrophysics, observing the sky in a survey mode, with a wide field of view and with good timing capabilities, promoting synergies with other observatories. It will be able to perform narrow-line spectroscopy and polarimetric measurements [45] (see figure 3.2). The AMEGO will fly in a low-Earth orbit, at an altitude of 600 km and an orbital inclination of 6°, performing an observation of the full sky every 3 hours (2 orbits). It will operate mainly in survey mode, but it has the capability to perform inertial target pointing. A data volume of 45 GB/day is expected [45]. A summary of the mission requirements and expected performance is presented in table 3.1.

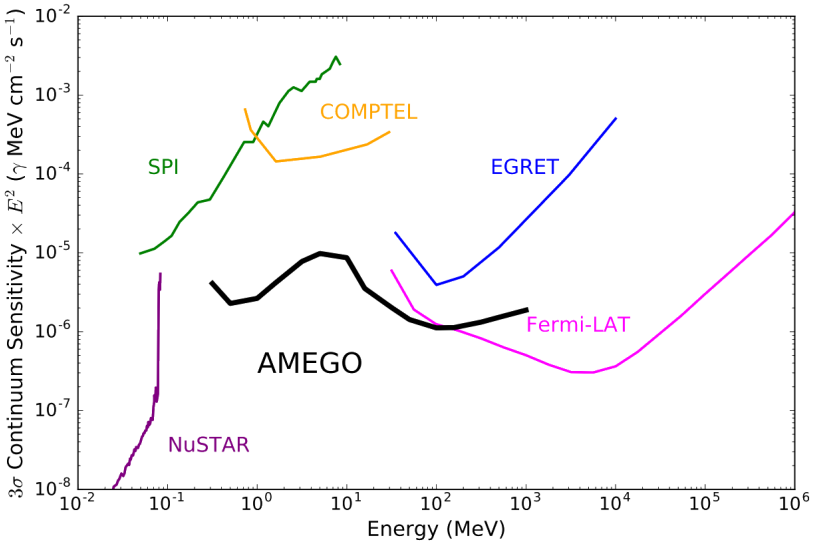

Figure 3.1: The MeV sensitivity gap and the continuum sensitivity of AMEGO for a 5-year mission. AMEGO aims to cover the sensitivity gap that currently exists in the hard X-ray and soft gamma-ray energy range. The 3σ continuum sensitivity is the minimum flux that produces a signal-to-noise ratio at least 3σ over the background level. Figure from [43].

[4]https://asd.gsfc.nasa.gov/amego-x/

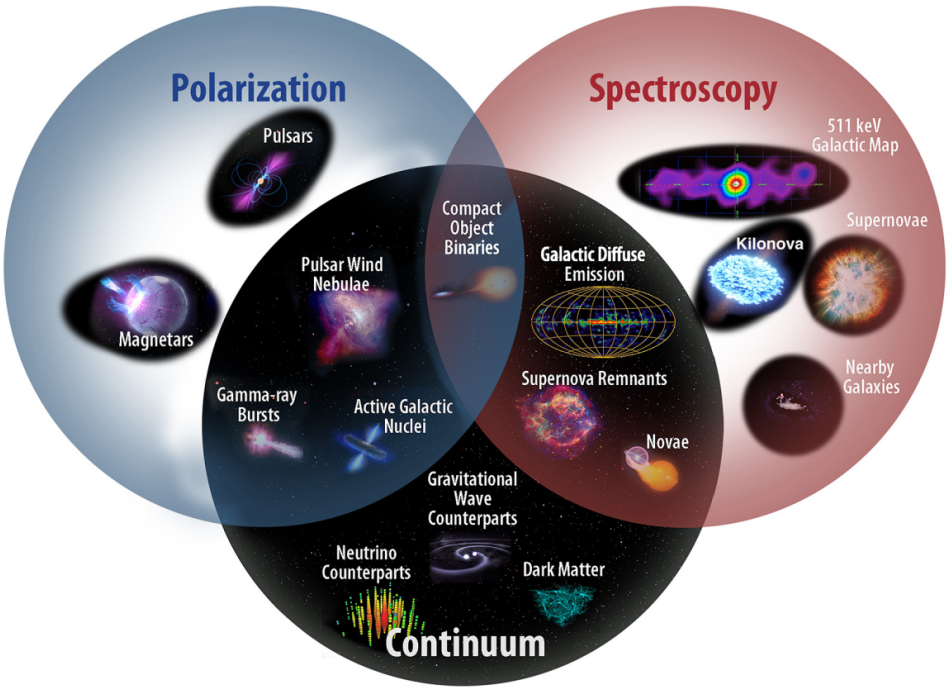

Figure 3.2: AMEGO will contribute to the high-energy astrophysics with time-domain measurements, continuously observing the sky and promoting synergies with measurements performed in other wavelengths. It will provide spectroscopic capabilities, increasing our understanding of element formation in dynamic environments, and will be able to perform polarimetric measurements, that will allow us to probe the conditions and processes behind highly energetic phenomena, such as astrophysical jets and winds of compact objects. Figure from [43].

The performance of AMEGO was simulated using MEGAlib [45]. The simulations provide an effective area between 500 and 1000 cm^2, an angular resolution of $\sim 11°$ at 200 keV and $\sim 2°$ at 2 MeV, an energy resolution of 1% at 1 MeV and ~10% at 1 GeV. The continuum sensitivity of AMEGO was also determined to be over an order of magnitude above the previous instruments that cover the same energy range, as can be observed in figure 3.1. Several factors contribute to its good sensitivity, such as the large effective area and the background rejection with the anti-coincidence detector and through the analysis of the detected signals.

The main requirements related to polarimetry are the energy range, the FOV and the MDP. Although the AMEGO observations will be performed in the 200 keV to $>$ 5 GeV energy range, the polarization measurements are expected be performed below 5 MeV [44]. This means that the main interaction mechanism, in which the polarization measurements are based on, is Compton scattering, as it is the most dominant process in silicon for photon energies below ~10 MeV (see figure 2.1). Regarding the measurements made in the pair regime, as the MEGAlib is optimized for the Compton regime, improvements on the identification and reconstructions can be expected when state-of-the-art algorithms developed for the Fermi-LAT are taken into account [45]. The FOV is related to off-axis observations, i.e., a FOV of 2.0 sr corresponds to a

observation of $\sim 16\%$ of the sky, and to sources being observed up to 47° off-axis, and a FOV of 2.5 sr corresponds to a observation of $\sim 20\%$ of the sky, and to sources being observed up to 53° off-axis.

Table 3.1: Summary of the requirements of the AMEGO instrument and its projected performance. The following are descriptions of examples of the scientific studies in which the sensitivity requirements applies: (1) Study of neutron star mergers, relativistic jets and of GRB prompt and afterglow emission. (2) Study of the explosion mechanisms of supernovae, production of heavy elements, distribution of the ejected matter and chemical composition of the progenitor star. (3) Source of galactic positrons and distribution of positron annihilation. (4) Characteristics of different classes of neutron stars and their winds. Adapted from [43].

Parameter	Instrument requirements	Projected performance
Energy range	300 keV to 1 GeV	200 keV to > 5 GeV
Energy resolution	$< 2\%$ FWHM (1 MeV)	1% FWHM (1 MeV)
FOV	> 2 sr	> 2.5 sr
Angular resolution	$< 5°$ FWHM (511 keV)	3° FWHM (511 keV)
Location accuracy	< 5 deg radius	< 1 deg radius
Absolute timing	< 10 μs	< 3 μs
Continuum sensitivity		
(1)	$< 5 \times 10^{-6}$ erg cm^{-2} s^{-1} (1 MeV, 2 sec)	10^{-6} erg cm^{-2} s^{-1} (1 MeV, 2 sec)
(2)	$< 2 \times 10^{-11}$ erg cm^{-2} s^{-1} (1 MeV)	7×10^{-12} erg cm^{-2} s^{-1} (1 MeV)
Narrow line sensitivity		
(2)	$< 10^{-5}$ ph cm^{-2} s^{-1} (^{26}Al 1.8 MeV, 5 yrs)	10^{-6} ph cm^{-2} s^{-1} (^{26}Al 1.8 MeV, 5 yrs)
(3)	$< 4 \times 10^{-6}$ ph cm^{-2} s^{-1} (511 keV, 5 yrs)	2×10^{-6} ph cm^{-2} s^{-1} (511 keV, 5 yrs)
MDP		
(1)	$< 30\%$ for a GRB with fluence of 8×10^{-6} erg cm^{-2} (300 keV to 3 MeV)	$< 20\%$ for a GRB with fluence of 8×10^{-6} erg cm^{-2} (300 keV to 3 MeV)
(1)	$< 20\%$ for a 100 mCrab source in 10^6 sec	4% for a 100 mCrab source in 10^6 sec
(4)	$< 30\%$ for 10^{-10} erg cm^{-2} s^{-1} (300 keV, 2 yrs)	5% for 10^{-10} erg cm^{-2} s^{-1} (300 keV, 2 yrs)

3.3 Detectors

The AMEGO instrument is composed of four main subsystems [43]: the tracker, the low-energy calorimeter, the high-energy calorimeter and the ACD. These subsystems, except the ACD, are presented in figure 3.3. They are highly modular and are mounted in the so called towers. These towers consist of modules of the tracker, low-energy calorimeter and high-energy calorimeter. The AMEGO is composed of four towers, each in a quadrant.

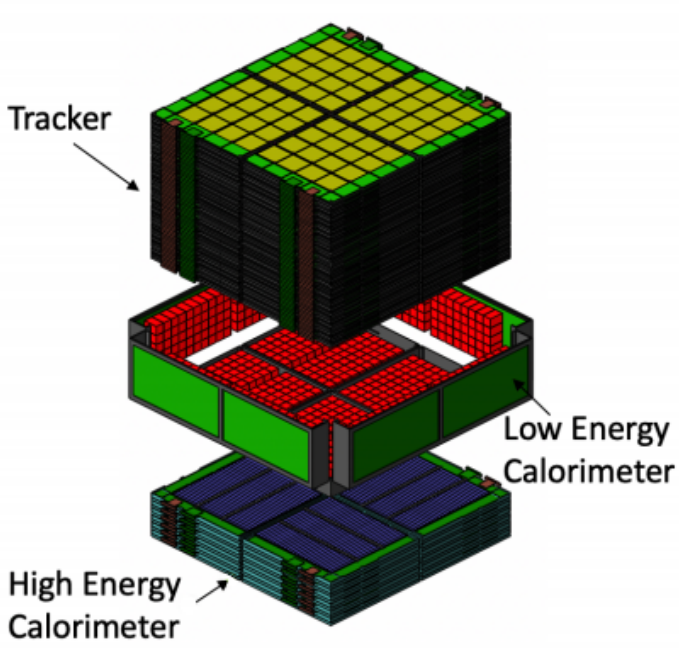

Figure 3.3: Scientific instruments of AMEGO. The detectors are modular and divided in 4 towers. Each tower is composed of 60 layers of DSSDs, CZT detectors that cover the bottom of the DSSDs and 1/3 of its sides, and 6 layers of thick CsI bars beneath the CZT detector. It is not presented the ACD, which covers the sides and top of the DSSDs and of the CZT detectors.

3.3.1 Tracker

The tracker is composed of DSSDs wafers. It consists of 4 columns of stacked DSSDs. Each column is composed of 60 layers, separated by 1 cm, of modules of 4×4 wafers of DSSDs. Each DSSD wafer is 9.5×9.5 cm^2 and 500 μm thick, with 190 strips per side, which corresponds to a strip pitch of 500 μm.

These detectors are used to measure the first interaction of a Compton scattering event (at energies lower than ~10 MeV) and also the track of pair-conversion products (mainly above ~10 MeV, where pair-conversion is the main interaction of the γ-rays with the material). As DSSDs are a medium of low atomic number, the effect of Doppler broadening on the angular resolution is minimized [24]. The thickness of the DSSDs affects the efficiency, changing the amount of sensitive material, but also affects the tracking of Compton scattered electrons and of the pair-conversion products, influencing the reconstruction of the events. The strip pitch in each wafer influences the position resolution.

DSSDs are position-sensitive detectors widely applied in the tracking of high-energy particles and in the imaging of X-rays [14]. These detectors consists of thin silicon wafers with electrodes,

subdivided into a number of parallel strips, displaced in a orthogonal orientation on the opposite sides of the wafer. The opposite strips on the wafer consist of n and p-type strips. The electron-hole pairs, created within the volume, drift along the electric field and induce a signal on the strips of both sides of the wafer. If a signal is induced in more than one strip, the position of the interaction can be determined with center of gravity techniques.

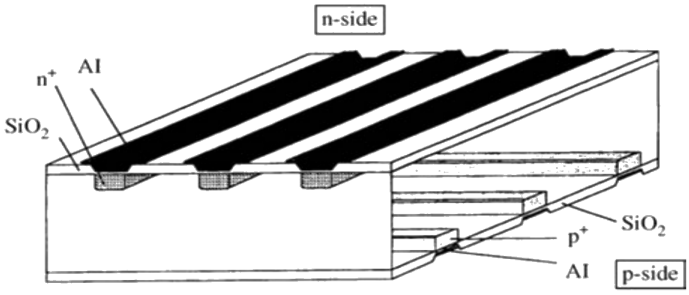

Figure 3.4: Schematic of a double-sided silicon strip detector. Adapted from [14].

3.3.2 Low-energy calorimeter

The low-energy calorimeter is composed of modules of virtual Frisch-grid CZT detectors. Each CZT detector has $8 \times 8 \times 40$ mm^3 and read by 6 channels, providing a sub-mm position sensitivity in 3 dimensions. It operates at room temperature and provides a good energy resolution (<1% at 662 keV). These CZT bars are arranged in modules, with a 4×4 configuration, sharing a circuit board which provides 4 kV to bias the detectors. These modules are then arranged in arrays of 5×10.

The low-energy calorimeter covers the bottom of the tracker and surrounds its sides, covering 1/3 of its height. This configuration enhances the chance of photoabsorption of a scattered photon, increasing the effective area of the instrument. It also benefits the polarimetric measurements, as the modulation factor is generally higher for scattering angles close to 90° [1]. This detector can act as a stand-alone Compton detector, not requiring the first interaction to take place in the tracker, increasing the detection efficiency at lower energies.

Virtual Frisch-grid CZT detectors are cadmium zinc telluride (CdZnTe) semiconductor detectors, that make use of the same concept used in Frisch-grids in gaseous detectors. $Cd_{1-x}Zn_xTe$ detectors have wide bandgaps (for example, for x equal to 0.04 and 0.20, the bandgap is 1.53 and 1.64 eV, respectively [14]), which makes them suitable for operations at room temperature. The high-atomic number ($Z_{Cd} = 48$, $Z_{Zn} = 30$, $Z_{Te} = 52$) translates in a higher coefficient of linear attenuation and higher detection efficiency than lower atomic number detectors. CZT detectors show, however, low hole mobility [46] and significant hole trapping [47], inhibiting an efficient collection of the total charge. A solution for this problem is to make these detectors operate as single-charge-carriers, in which only electrons contribute to the induced signals, as is achieved in gaseous detectors with Frisch grids. This results in a better energy resolution [47]. The Frisch grid effect, without an embedded grid, can be achieved in multiple ways. A simple

method is introducing a non-contacting Frisch ring [47] (see figure 3.5). This configuration is depth-sensitive, allowing for the estimation of the Z-coordinate of the interaction point [46, 48]. Another configuration, the position-sensitive virtual Frisch grid (PSVFG), can provide <1 mm resolution on the XYZ coordinates [48]. This is achieved by reading the amplitude of the signals of the 4 metal pads that are attached to dielectric shell near the anode (see figure 3.6). This allows for the correction of non-uniformities caused by small defects of the crystal. As mentioned in [48], this detector has an energy resolution <1% at 662 keV, for temperatures up to 30° C.

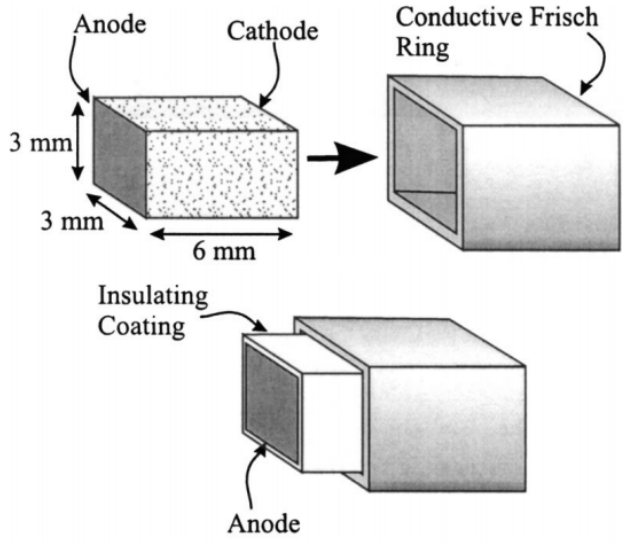

Figure 3.5: Virtual Frisch grid CZT detector. The CZT detector is coated with an insulator and placed inside a conductive ring. The conductive Frisch ring contributes with the screening of the induction due the motion of charges in the region between the ring edge and the cathode, thus the induction on the anode results from the movement of charges in the region between the anode and the Frisch ring. Adapted from [47].

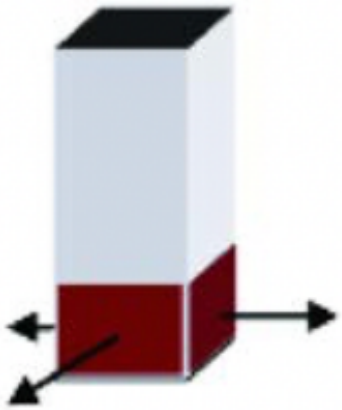

Figure 3.6: The position-sensitive virtual Frisch grid (PSVFG) is an improvement of the virtual Frisch-grid detector. It is built in a similar way, but sensitive to the position of the interaction, due to the 4 metal pads that are attached near the anode. Adapted from [48].

3.3.3 High-energy calorimeter

The high-energy calorimeter consists of thick CsI scintillators doped with thallium. It is composed of 6 layers of 26 CsI bars. Each bar is $1.5 \times 1.5 \times 38$ cm^3 and it is wrapped in a reflective material, to maximize the light collection. The yielded scintillation light is collected at both ends of the bars by SiPMs. Each layer of the CsI bars are oriented orthogonally to the one above. The depth of the interaction along the bar is determined by the amplitude of the signals generated at each end, with a position resolution of 1 cm at 1 MeV.

The high-energy calorimeter is placed at the bottom of the instrument, under the low-energy calorimeter and it is designed to fully contain the products of the high-energy pair-production events. It is also optimized to the detect low-energy pair events that extend beyond the low-energy calorimeter.

A smaller version of the high-energy calorimeter that is being built for the AMEGO is presented in figure 3.7.

CsI(Tl) detector is an inorganic scintillator. Its high atomic number ($Z_{Cs} = 55$, $Z_I = 53$, $Z_{Tl} = 81$) makes it suitable for γ-ray spectroscopy due to the increased photoelectric cross-section, when compared with lower atomic number materials. The inorganic scintillators are known for their good light output and linearity, but are generally slower than the organic ones.

CsI scintillators are suitable for space instrumentation, not only for its large absorption coefficient but also because it can be subject to severe conditions from strong vibrations and shocks. When cut into thin sheets, it is malleable and can be bent without fracturing [14]. The dopping of CsI scintillators with Tl results in an emission spectrum with a peak at 540 nm, reducing the effect of self-absorption. CsI(Tl) also has the advantage of having different decay times for various exciting particles, allowing for their identification with the analysis of the pulse shape.

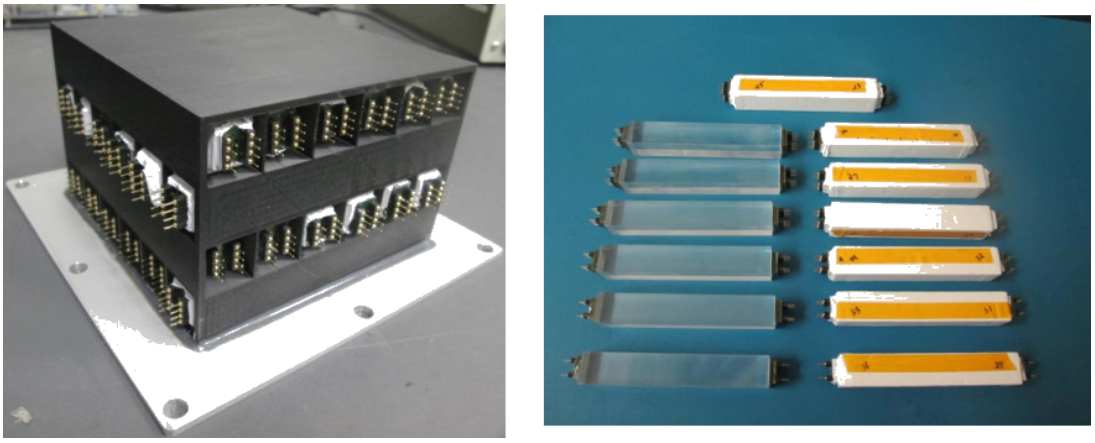

Figure 3.7: On the left it is presented the high-energy calorimeter prototype. It consists of 4 layers of six $16.7 \times 16.7 \times 100$ mm^3 CsI(Tl) crystals. The prototype is intended to be used in the beam test and balloon flight. On the right it is presented the CsI(Tl) crystals. Each crystal is read on its ends, by an array of 2×2 SiPMs. Adapted from [49].

3.3.4 Anti-Coincidence Detector

The anti-coincidence detector (ACD) consists of 5 Eljen EJ-208 plastic scintillator panels, surrounding the 4 sides and the top of the instrument. It is based on the ACD of Fermi-LAT, sharing the same plastic scintillator material and design [45] (see figure 3.8). Each panel has a thickness of 15 mm and the side panels have an area of 134×87 cm^2 while the top panel has an area of 134×134 cm^2. These are wrapped in a reflective material to maximize light collection. On the edges of each panel it is placed a wavelength shift bars, with SiPMs at its ends. This detector has no position resolution as the only requirement is to effectively veto charged particles [45].

The ACD improves the sensitivity of the instrument and reduces the amount of unwanted data in the system, by detecting charged particles that transverse it and vetoing the signals induced in the main detectors. The abundance of cosmic-rays, in the orbit of a γ-ray telescope orbit, generate signals that may overcome the ones of the observed sources by two orders of magnitude [50]. Thus the ACD acts as the first layer of shielding against the background, vetoing unwanted signals.

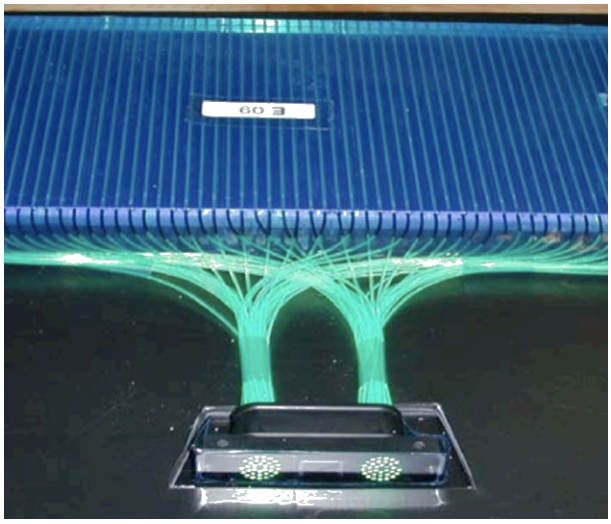

Figure 3.8: ACD panel from Fermi Gamma-Ray Space Telescope. The ACD from AMEGO is based on this same plastic scintillator detectors. The main differences between the two is that the ACD from AMEGO is not segmented, while the ACD from Fermi is, providing it with sensitivity to position and allowing it to not veto an event that was produced withing the instrument and interacted with the ACD. The ACD from AMEGO uses wavelength shifting bars on the edges of the panels, which have its light measured by SiPMs, while the ACD from Fermi uses wavelength shifting optical fibers, which are read by PMTs. Figure from [51].

3.4 Characterization of the polarimetric sensitivity

The polarimetric sensitivity of the AMEGO mission is characterized through simulations with MEGAlib. This characterization is based on Compton interactions. In order to achieve this, the modulation factor, the efficiency, the background and the MDP are computed with data from the simulations, where the instrument is irradiated with monochromatic sources and astronomical sources with more complex spectra, such as the Crab nebula and the GRB 170717A. The sensitivity of the instrument is also estimated for off-axis sources.

3.4.1 Computation of the modulation factor and efficiency

The modulation factor can be directly computed using the graphical user interface of Mimrec, from the azimuthal distribution of the scattered photons, as is explained in sections 2.3.1 and 2.3.2. The uncertainties associated with the modulation factor values are obtained from the fit performed through Mimrec.

In this work, when we refer to efficiency, it is meant efficiency of detection through Compton scattering, except when mentioned otherwise. The efficiency is also presented taking into consideration certain event selections, such as the ARM cut. It is determined as follows: the photons, from a far-field point source, are originated in a random position from the disk tangent

to the surrounding sphere. The surrounding sphere can be visualized in figure 3.9. As the area of the disk is greater than the area of the instrument, only a fraction of photons will reach the instrument. This fraction is obtained by the ratio between the projected area of the instrument, in relation to the disk, and the area of the disk. The efficiency is obtained by computing the percentage of interactions that pass a given set of event selections from the total number of photons that reach the instrument. Examples of event selection criteria include an event being reconstructed as a Compton event, the ARM being smaller than a given angle, the detector in which the first interaction takes place, etc. The total number of generated photons can be consulted in the .sim files, while the number of photons that the event selections can be obtained through the Mimrec graphical user interface. The area of the disk and the area of the instrument are defined in the Geomega files. The efficiency is then calculated through equation 3.1, where N stands for the number of photons and A for the area. The uncertainty associated with the efficiency is obtained from the propagation of the uncertainties associated with photon detection Poisson statistics, which is $\sigma_N = \sqrt{N}$.

$$\varepsilon = \frac{N_{measured}}{N_{generated} \times \dfrac{A_{instrument}}{A_{disk}}} \tag{3.1}$$

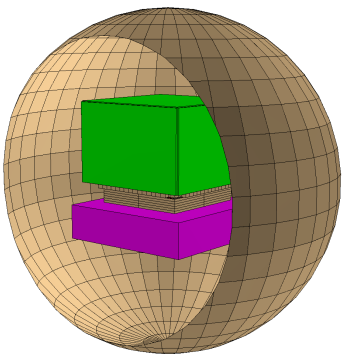

Figure 3.9: Geometry of the instrument and the surrounding sphere. These are defined in the Geomega files. It is also defined a disk, whose center is tangent to the surrounding sphere. The sphere and the disk have the same radius, that has to be great enough to surround the instrument without overlapping it.

3.4.2 Simulations overview

In this section it is given an overview of the steps taken in order to characterize the polarimetric sensitivity of the AMEGO instrument. The goal is to compute the modulation factor and efficiency of the instrument, as a function of the energy of the photons, estimate the background signal rates on the operation conditions of the instrument, and compute the MDP for a given source as a function of the observation time.

The first step before performing the simulations and the corresponding data analysis is to prepare the geometry and source files. Here it is defined the materials of the detectors, their size, spacial arrangement, properties, such as energy and spatial resolution, and the characteristics of source, such as particle type, position, beam type, spectrum, flux, etc. It is also defined the

detectors, namely trigger threshold, the number of hits to activate a trigger, etc. A detailed description of the configurable parameters can be found in the Geomega and Cosima manuals[5].

A preliminary study is performed, with the objective of providing an insight on what type of interactions may occur in the instrument, for a given photon energy. This study also provides information on how some parameters, such as the ARM cut event selection and the bin width applied during the RBT, may affect the modulation factor and efficiency of the instrument.

In order to characterize the instrument modulation factor and efficiency, it is performed a set of simulations where a 100% polarized monochromatic beam, from a far-field point source, irradiates the instrument on-axis. Then, simulations are performed in order to evaluate the effects of the off-axis incidence on the modulation factor and on the efficiency of the instrument.

As explained in section 3.4.3, the base geometry files of AMEGO do not include all possible combinations of triggers. In order to access the impact of the triggers on the modulation factor and efficiency of the instrument, a new set of simulations is performed for a new geometry that includes all possible triggers. These new trigger criteria enables a better understanding on how photons interact with the instrument and which set of sensors contribute the most for the efficiency and overall modulation factor.

The last study to assess the response of the instrument as a function of the energy of the photons, is the evaluation of the effects of event selection, more specifically the selection of events through the scattering angle of the first Compton interaction.

The characterization of the polarimetric potential of the AMEGO mission is ended by determining its sensitivity to polarization under operational conditions, i.e., in orbit. In order to do so, an estimation of the expected background signal rates is required. This can be achieved through simulations with MEGAlib, and will be further explained in section 3.4.9. The MDP is computed for different sources, such as the GRB 170817A, a short GRB model (further explained in section 3.4.10) and the Crab, as function of the observation time. For the same source, are performed simulations in different energy ranges in order to evaluate the trade-off between background rates, flux of the source, modulation factor and efficiency, since all of these factors vary with the spectrum of the source and its energy range.

3.4.3 Geometry

In this section it is presented and summarized the geometry of the AMEGO, defined in Geomega. The geometry was developed by the AMEGO team and is available at GitHub[6]. In figure 3.10a it is presented the geometry of the detectors of AMEGO (the passive material and the ACD are omitted). In figures 3.10b and 3.10c it is presented a representation of the modules of the tracker and low-energy calorimeter, respectively, and in figure 3.10d it is presented a representation of the high-energy calorimeter.

A difference between the low-energy calorimeter of the geometry and the design of the real

[5]https://megalibtoolkit.com/documentation.html
[6]https://github.com/ComPair

instrument was detected while inspecting the geometry files. In the Geomega geometry the modules of this detector are 6×6, while the modules of the low-energy calorimeter are 4×4.

The trigger criteria of the detectors affect its performance, as will be further discussed in section 3.4.7. In table 3.2 are presented the trigger criteria of the base geometry of AMEGO and of the geometry with all the possible combinations of triggers.

The energy threshold of the detectors also affects its performance, as will be discussed in section 3.5.1. The discussion is performed during the study of the performance of the AMEGO-X, and resulted from the interest of knowing how a different detector, the *AstroPix*, in replacement of the DSSDs of the tracker, affects the sensitivity to polarization. The AstroPix detector allows for lower thresholds, improving the sensitivity of AMEGO-X at lower energies. The trigger thresholds of the AMEGO and AMEGO-X detectors are 60, 50, 100 and 200 keV, for the tracker, low-energy calorimeter, high-energy calorimeter and ACD, respectively, and the trigger thresholds of the AstroPix is 25 keV.

The computation of the efficiency and the MDP requires the value of the area of the instrument, which is approximately 90 cm^2, and the radius of the disk associated with the surrounding sphere, which is 150 cm.

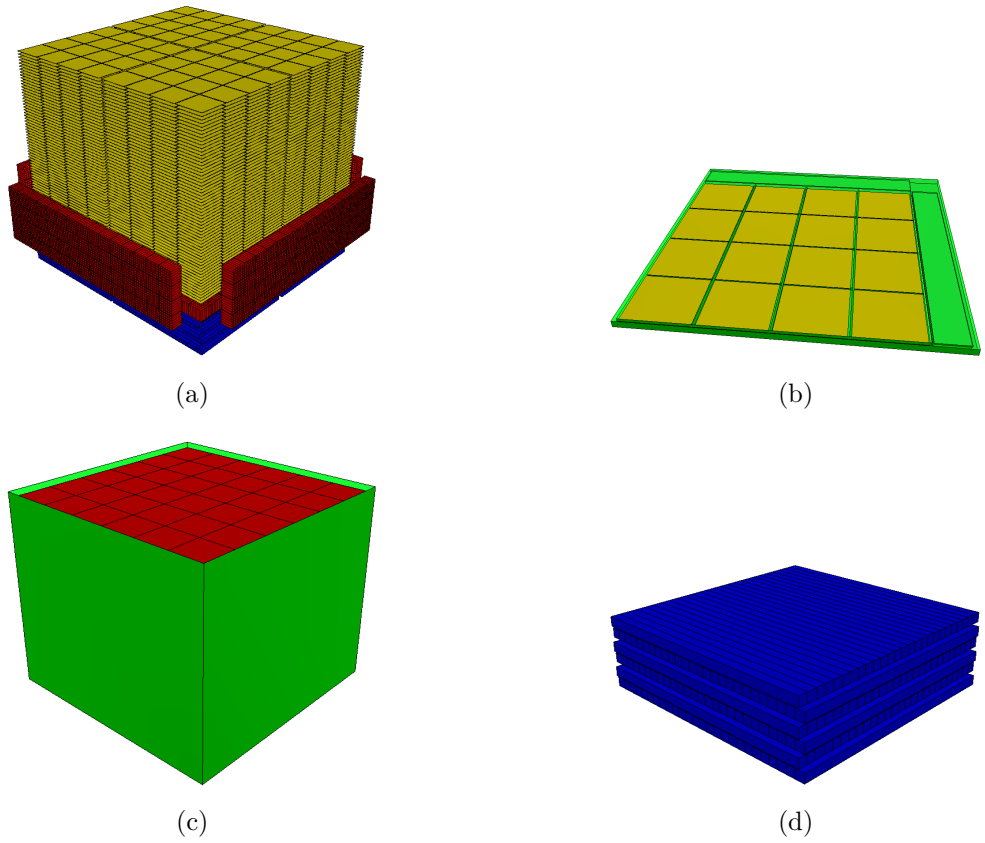

(a) (b) (c) (d)

Figure 3.10: Visualization of the AMEGO detectors defined in Geomega. a) Detectors of AMEGO, except the ACD, without passive material. b) A module of the tracker. c) A module of the low-energy calorimeter. d) The high-energy calorimeter.

Table 3.2: Triggers defined for the AMEGO instrument. The additional, or modified, triggers included in the "all trigger" geometry are presented in bold. In addition to the triggers presented here, it is also defined an additional trigger as a veto, corresponding to any event that has at least one hit on the ACD.

AMEGO - base triggers
Two hits on the tracker
One hit on the tracker and one hit on the side low-energy cal.
One hit on the tracker and one hit on the bottom low-energy cal.
Two hits on the tracker and one hit on the high-energy cal.
Two hits on the side low-energy cal.
Two hits on the bottom low-energy cal.
One hit on the side low-energy cal. and one hit on the bottom low-energy cal.
AMEGO - all triggers
Two hits on the tracker
One hit on the tracker and one hit on the side low-energy cal.
One hit on the tracker and one hit on the bottom low-energy cal.
One hit on the tracker and one hit on the high-energy cal.
Two hits on the side low-energy cal.
One hit on the side low-energy cal. and one hit on the bottom low-energy cal.
One hit on the side low-energy cal. and one hit on the high-energy cal.
Two hits on the bottom low-energy cal.
One hit on the bottom low-energy cal. and one hit on the high-energy cal.
Two hits on the high-energy cal.

3.4.4 Preliminary studies

As mentioned before, it was performed a preliminary study with the objective of providing an overall idea of the interactions taking place in the detector and its efficiency. This study also aims to provide insights on the consequences of the decisions made during the data analysis, such as the ARM cut event selection and the bin width applied during the RBT analysis.

Physical processes' ratio

The efficiency of detection of photons is determined with the simulations described in table 3.3. As the interactions through photoelectric effect require only one trigger, the base triggers filter these events. In order to estimate the rates of the photoelectric effect, the triggers of the geometry were modified to a single trigger per detector.

Table 3.3: Summary of the simulation parameters for an on-axis source.

Parameter	Description
Particle type	Photons
Energy	200 to 2000 keV
Spectrum	Monoenergetic
Polarization	100% linearly polarized and unpolarized beam
Beam	Far-field point source located at $\theta = 0$ and $\phi = 0$
Flux	1 photon/cm^2/s
Number of triggers	500 000

In figure 3.11 it is presented the efficiency of detection of photons, differentiating between the main interaction mechanisms in the keV energy range. It can be observed that the Compton interactions start to dominate for energies above 500 keV, while the photoelectric effect dominates below this energy. The pair production events have no significant contribution in the studied energy range, due to the small cross-section.

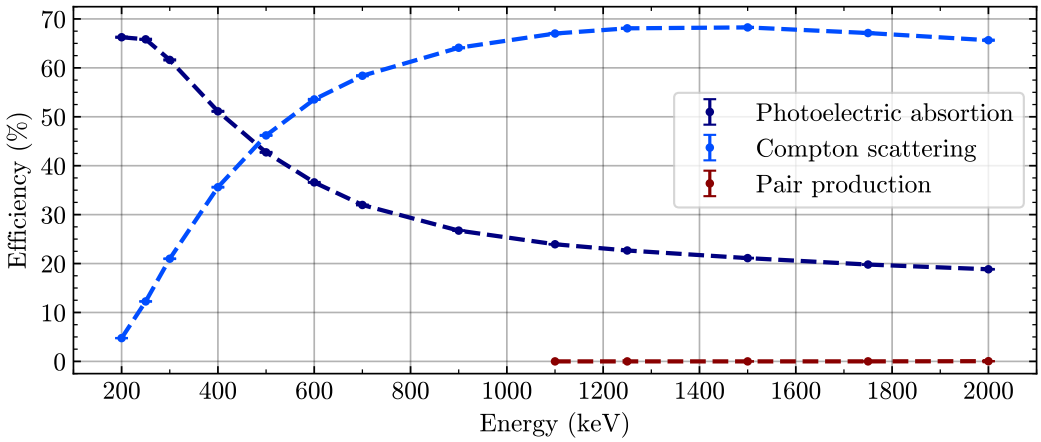

Figure 3.11: Overall efficiency of AMEGO, differentiating between the main interaction mechanisms of high-energy photons with matter.

Bin width effects

As shown in [1], the radial bin width affects the computed value of the modulation factor. It is higher for smaller radial bin widths and decreases as the width of the bins increases. In a real scenario, the number of detected photons may be small and the number of photons that pass the event selection even smaller, so it may be necessary to use wider bins in order to have a smoother distribution (see figure 3.12).

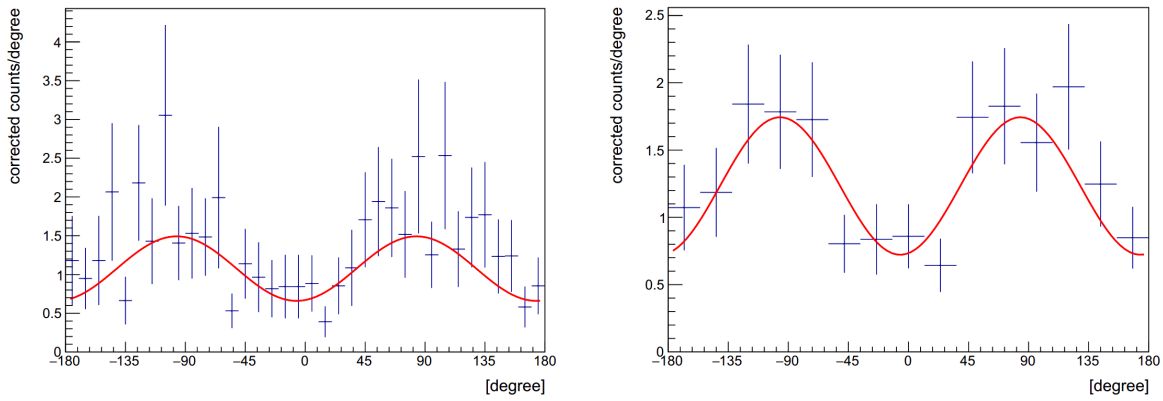

(a) (b)

Figure 3.12: Polarigrams obtained with 500 keV photons. The number of photons in the polarigram is kept low ($\sim$ 500 photons) in order to have a qualitative idea of the influence of the bin width in the construction of polarigrams with low counts. In a) the polarigram is constructed with a radial bin width of 10° and in b) it is 24°.

These results were obtained with the simulation settings described in table 3.3. In figure 3.13 it is presented the modulation factor as a function of the radial bin width, computed with data from the simulations of the 250 keV source. The effects of the ARM cut event selection, on the modulation factor and efficiency, will be discussed in the following section, but for this plot it is chosen an ARM cut of 15°. In figure 3.14 it is presented the ratio of the modulation factor, for different energies, computed for a given bin width, and the modulation factor determined for a radial bin width of 1°.

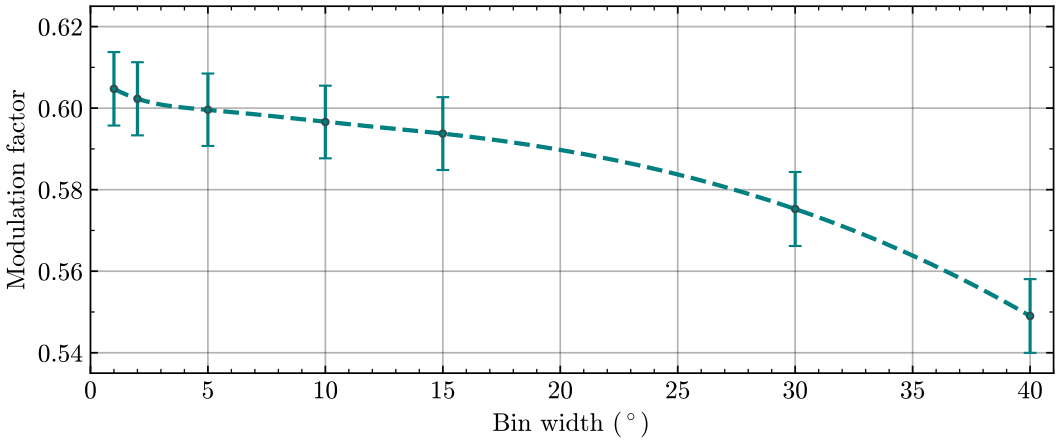

Figure 3.13: Modulation factor as a function of the radial bin width applied during the RBT. Simulations performed with a 250 keV far-field point source.

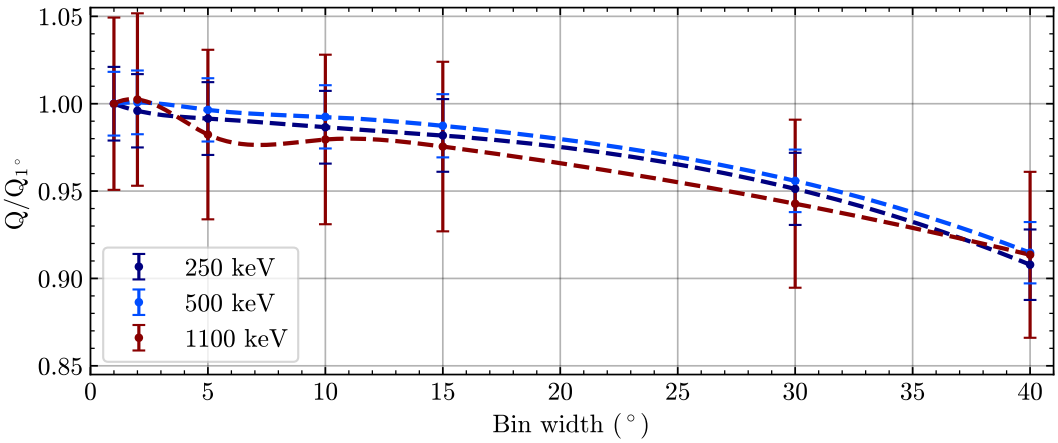

Figure 3.14: Ratio of the modulation factor, for different energies, computed for a given bin width, and the modulation factor computed for a radial bin width of 1°.

F. Lei et al. [1] performed a similar analysis. Lei's results are similar to those observed in figure 3.14. The authors observed a reduction of 1.1% and 2.9% of the modulation factor, for a radial bin size of 15° and 24°, respectively.

In conclusion, one can state that the radial bin width slightly affects the modulation factor. When the photon counts are low, a wider bin may allow us to perform a better fit at the expense of a small percentage of the modulation factor.

ARM cut effects

In real operation conditions, the ARM is one of the most relevant ways of determining which photons were emitted from a given source. It allows for the operation of the telescopes with a large FOV, detecting photons from multiple directions and sources at the same time, allowing the discrimination between photons of different sources, by choosing the photons that are reconstructed to originate from a certain angular direction.

The effects of the ARM cut event selection on the modulation factor and efficiency of the instrument were estimated and analysed, using the simulation settings described in table 3.3.

In figure 3.15 is presented the modulation factor as a function of the ARM cut, computed with a fixed radial bin width of 15°. It can be observed that the modulation factor tends to increase as the ARM cut decreases. The reason behind this phenomenon, may be that events with a wide ARM correspond to events from photons that are not completely absorbed within the instrument and from incorrectly reconstructed events. In [18] it is shown that wrongly reconstructed events contribute to the widening of the ARM peak. The widening of the ARM peak is also due to other factors, such as the ones discussed in section 2.2.2, however if the events are wrongly reconstructed, such as the ordering of the Compton interactions, the polar and azimuthal angles of the first interaction will differ from their true values. A wrong scattering angle translates into a wrong reconstruction of the direction of the incident photon, which affects the ARM directly, and a wrong azimuthal scattering angle affects the overall instrument modulation factor. On

average, 90% of the Compton events are well reconstructed, varying between 85% and 95% in the energy range of interest [18]. Selecting events through the ARM can be an effective way of selecting the photons that are completely absorbed in the instrument and that are better reconstructed, leading to a more reliable modulation factor, at the expense of the efficiency.

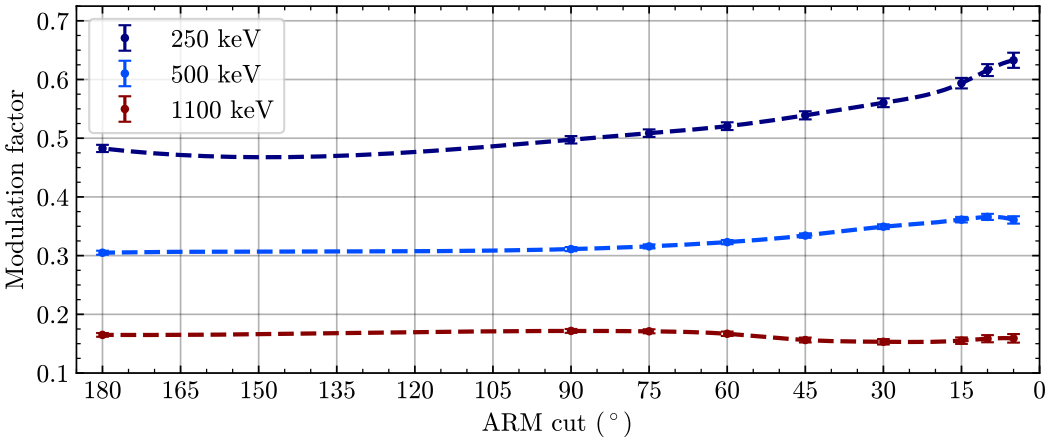

Figure 3.15: Modulation factor as a function of the ARM cut event selection.

In figure 3.16 it is presented the distribution of the ARM for the 500 keV photons originated from an on-axis source. The ARM cut selects the photons that are reconstructed to be originated from a given direction, e.g., if the ARM cut is 30° only the photons with an ARM $\leq$ 30° are selected. It can be observed that the majority of the photons have a small ARM, but that there is still a considerable number of photons that are reconstructed with a wide ARM.

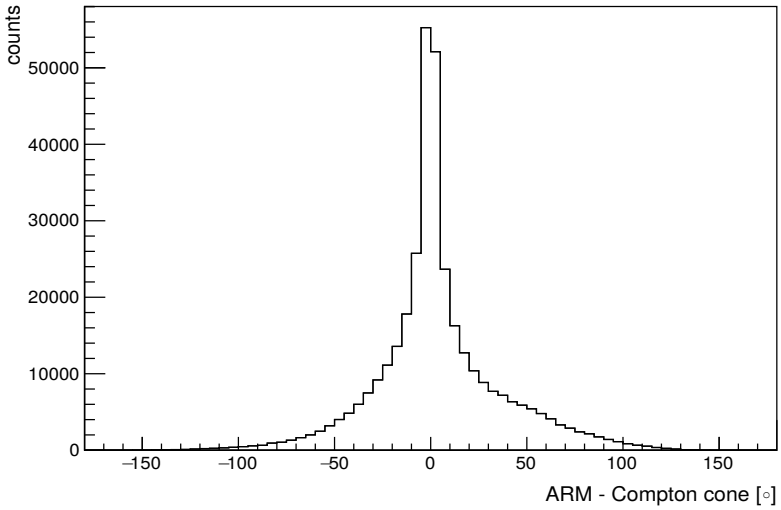

Figure 3.16: Histogram of the ARM of 500 keV photons.

The effects of the ARM cut on the efficiency of the detector are shown in figure 3.17. It is observed that the efficiency decreases as the ARM cut decreases. This is expected as we are

performing an event selection, which becomes more strict for smaller ARM cuts. With an ARM cut of 180°, no event selection based on the direction of the photon is being performed.

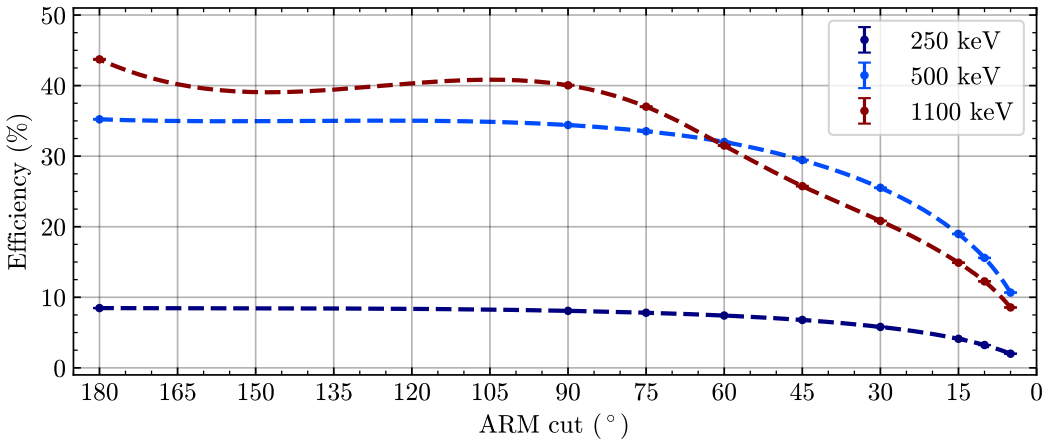

Figure 3.17: Efficiency as a function of the ARM cut.

In figure 3.18 is presented the ratio $\varepsilon/\varepsilon_{180°}$ as a function of the ARM cut. It shows how much the efficiency is affected by the ARM cut event selection. For 250 and 1100 keV, it is observed a decrease of the efficiency of $\sim 32\%$ and $\sim 52\%$, for an ARM cut of 30°, and a decrease of $\sim 51\%$ and $\sim 67\%$, for an ARM cut of 15°, respectively.

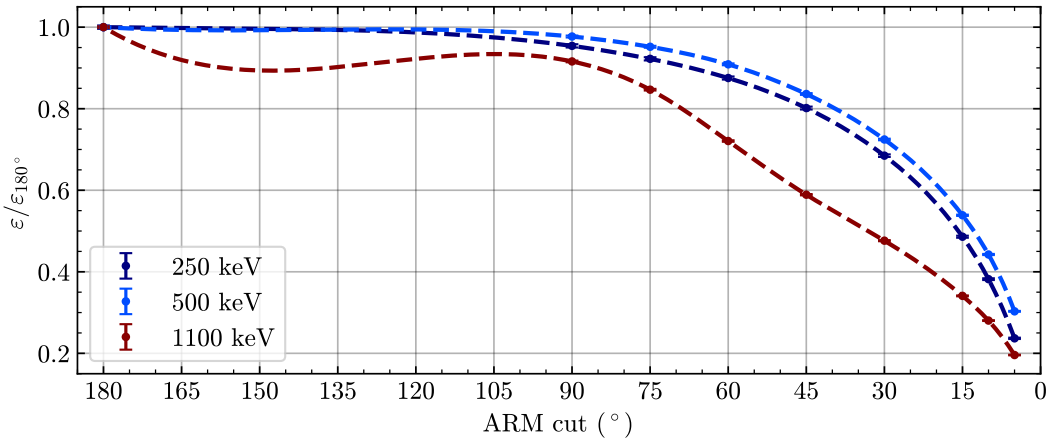

Figure 3.18: Ratio of the efficiency as a function of the ARM cut.

In the remainder of this work, the chosen values for the radial bin width and ARM cut are 10° and 15°, respectively. As mentioned in section 3.2, the angular resolution of AMEGO varies between $\sim 11°$ and $\sim 2°$, in the 200 keV to 2 MeV energy range. If the values of the ARM cut are equal to the ones of the angular resolution, the efficiency is reduced significantly, as can be observed in figure 3.18. The choice of the 15° ARM cut allows to obtain greater efficiencies, which benefits polarimetric measurements. It is chosen a radial bin width of 10°, as this value does not affect the computation of the modulation factor significantly.

3.4.5 Monochromatic source, on-axis

With a better understanding of the impact of the choices made during the data analysis, we start evaluating the performance of the instrument. The first step is to determine the modulation factor and the efficiency as a function of the energy, for an on-axis irradiation. These are computed with the simulation settings described in table 3.3, performed with the base trigger geometry.

In figures 3.19 and 3.20, are presented the modulation factor and efficiency as function of the energy, respectively.

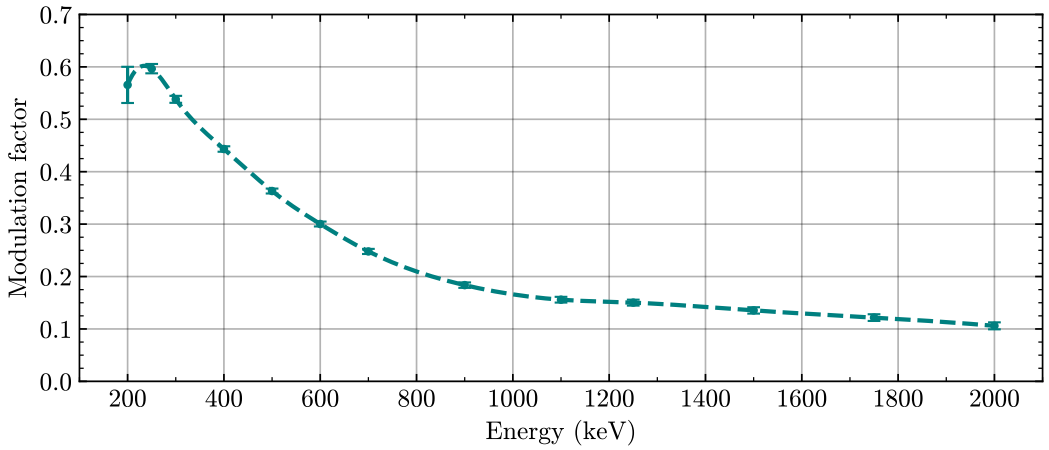

Figure 3.19: Modulation factor as a function of the energy.

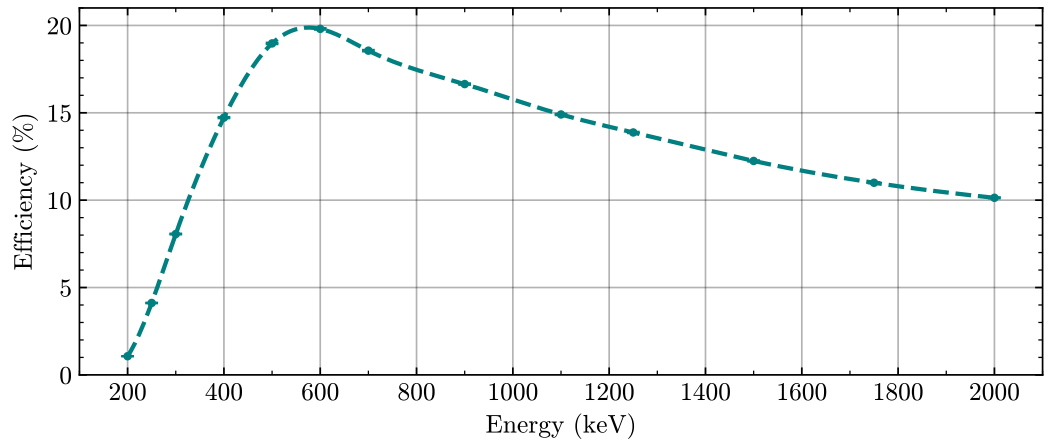

Figure 3.20: Efficiency as a function of the energy.

In figure 3.19 the plot shows an unexpected trend. It is expected that the modulation factor is higher at lower energies, while the plot has a maximum at 250 keV instead of 200 keV. One possible reason for this, is the wrong reconstruction of the events, such as the ordering of the Compton interactions. As seen before, the ARM cut is an effective tool to select the well reconstructed events. In figure 3.21, the modulation factor is computed with increasingly

smaller ARM cuts. It can be observed that for an ARM cut of 3° the maximum modulation factor is obtained at the lowest energy.

In figure 3.20 it can be observed that the efficiency is the highest at 600 keV and it is the lowest for energies below ∼300 keV. This may be due to a higher cross-section of the photoelectric effect at lower energies, reducing the overall efficiency of detection through Compton scattering.

POLAR, as mentioned in section 2.4.4, presents an efficiency of 14% for Compton events, in the 50 - 500 keV energy range, while performing no ARM cut event selection. AMEGO presents an average efficiency of ∼11% in the 200 - 500 keV range, and an efficiency of ∼15% in the 200 - 1000 keV range, while applying an ARM cut of 15°.

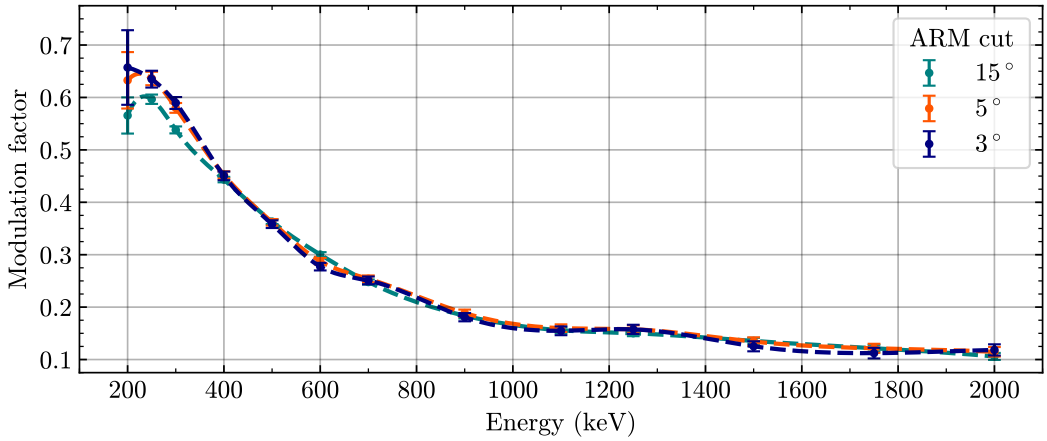

Figure 3.21: Modulation factor as a function of the energy of the photons, for different values of the ARM cut event selection.

In figure 3.22 is presented the modulation factor as a function of the energy of the photons and the polarization angle of the beam. It can be observed that the modulation factor does not vary significantly with the polarization angle.

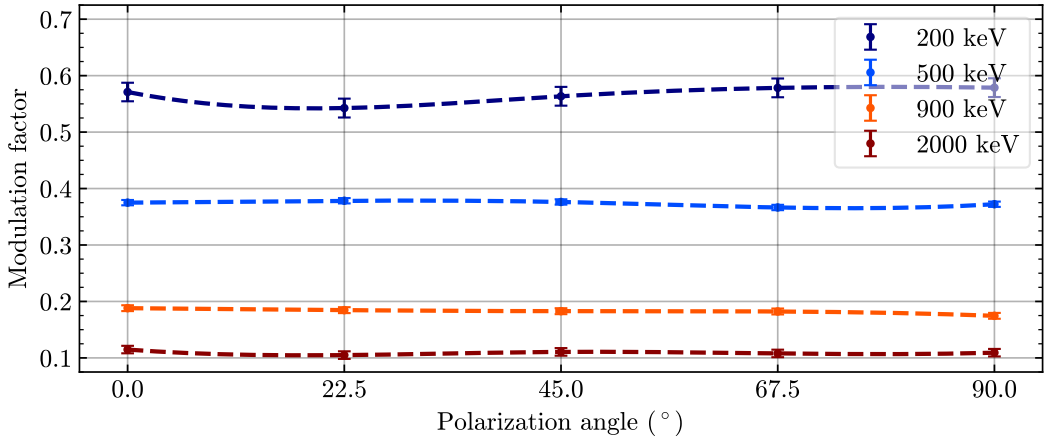

Figure 3.22: Modulation factor as a function of the polarization angle.

3.4.6 Monochromatic source, off-axis

As the main mode of operation of AMEGO is survey mode, most observed objects will be irradiating the instrument off-axis. In this section, it is studied how off-axis observations may affect the modulation factor and efficiency of the instrument. A new set of simulations is performed. These are summarized in table 3.4. According to the mission requirements (table 3.1), it is expected to observe photons up to 53° degrees off-axis, but it is performed simulations with sources up to 180° off-axis.

Table 3.4: Summary of the simulation parameters for an off-axis source.

Parameter	Description
Particle type	Photons
Energy	200 keV and 500 keV
Spectrum	Monoenergetic
Polarization	100% polarized and unpolarized beam
Beam	Far-field point source at $\theta \in [0, 180]$ and $\phi = 0$
Flux	1 photon/cm^2/s
Number of triggers	500 000

In figure 3.23 it is presented the modulation factor as a function of the angle of incidence of the photons. Mimrec allows the application of corrections to the off-axis incidence through its graphical user interface. It can be observed that, with the off-axis corrections, the modulation factor stays approximately constant, even for wider angles than the 53° threshold.

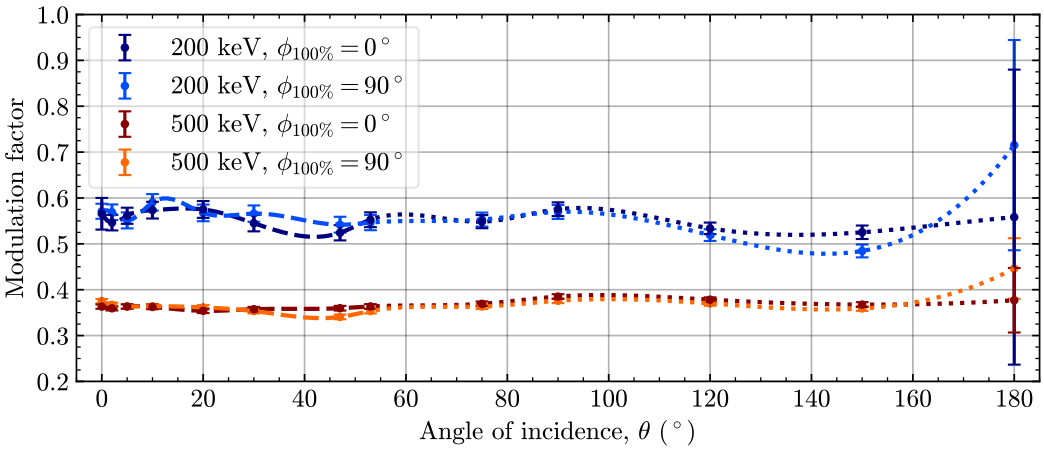

Figure 3.23: Modulation factor as a function of the angle of incidence of the photons.

In figure 3.24 it is presented the efficiency as a function of the angle of incidence of the photons. It can be observed that, for the 200 keV photons the efficiency stays approximately constant, but that for the 500 keV photons the efficiency rapidly decreases with the angle of

incidence of the photons, since the photons are more energetic and therefore the probability of escaping through the lateral sides of the instrument is increased as the off-axis incidence angle rises. As the MDP equation (equation 2.22) varies with the efficiency, a decrease of sensitivity to polarization is expected for off-axis observations.

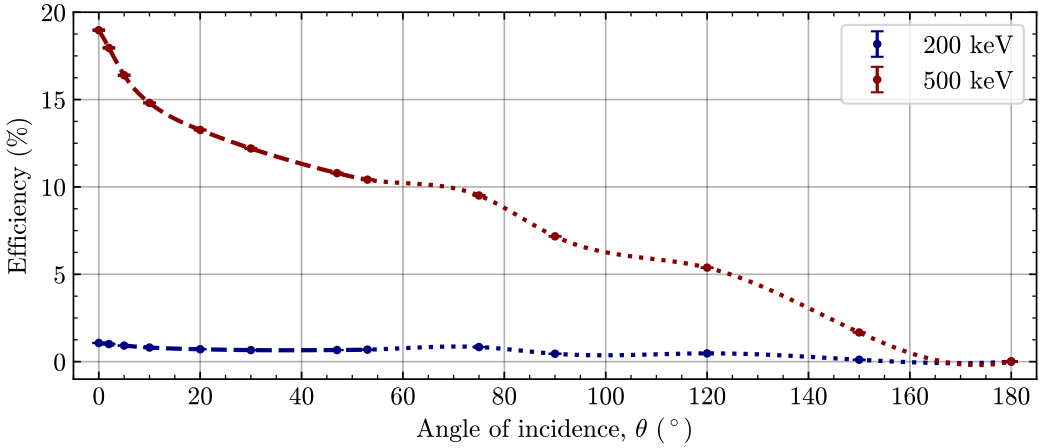

Figure 3.24: Efficiency as a function of the angle of incidence of the photons.

3.4.7 All triggers geometry

As the trigger criteria of the base geometry of AMEGO does not include all possible combinations, a new trigger criteria is defined in order to evaluate its effects on the modulation factor and efficiency of the instrument. The new trigger criteria includes all possible combinations of interactions in the detectors, that interact at least twice. These are summarized in table 3.2. The main addition are events that interact with the high-energy calorimeter. In the base geometry, the only trigger that includes the high-energy calorimeter is the one that requires two interactions in the tracker and one in the high-energy calorimeter.

During this study, it was observed that the base trigger criteria is not an effective way of selecting events that interact in a given detector. For example, a photon that interacts with the detectors in the following order: low-energy calorimeter → high-energy calorimeter → tracker, will trigger the *one hit on the tracker and one hit on the low-energy calorimeter* trigger, despite the first two interactions happening in the low-energy calorimeter and high-energy calorimeter. Even though the probability of photoelectric absorption in the calorimeter is high, the photon may backscatter in the high-energy calorimeter and then interact with the tracker.

The modulation factor and efficiency, as a function of the energy of the photons, were determined for the instrument with this new trigger criteria, denominated “all triggers”. These parameters are extracted from simulations described in table 3.3 and are presented in figures 3.25 and 3.26. The results are compared with the ones obtained for the base trigger geometry.

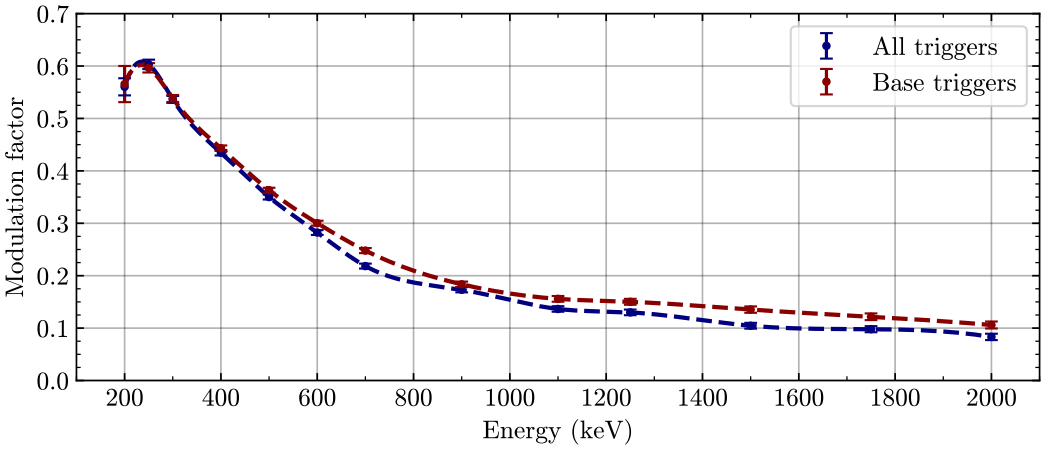

Figure 3.25: Modulation factor as a function of the energy of the photons for the base triggers and all triggers geometry.

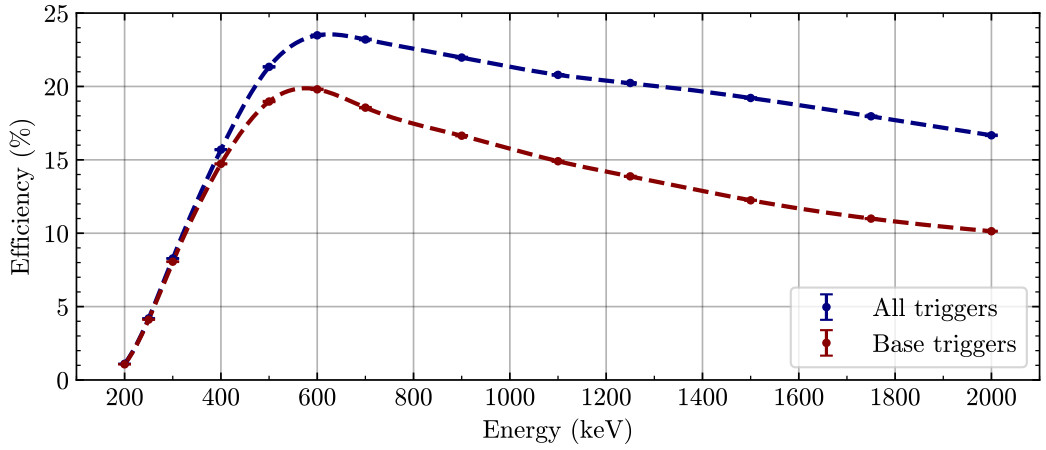

Figure 3.26: Efficiency as a function of the energy of the photons for the base triggers and all triggers geometry.

It is observed that for the all trigger geometry, the modulation factor decreases slightly and the efficiency increases, when compared with the base trigger geometry. The increase of the efficiency may be due to the acceptance of events that have been excluded by the base geometry, and the decrease of the modulation factor may be due to a worst position resolution of the high-energy calorimeter, worst energy resolution or acceptance of photons that scatter at very low angles, contributing with a lower modulation factor.

Detector selection

In order to have more detailed information on the interactions happening in the instrument and the contribution of each detector to the modulation factor and efficiency, a simple Python script that reads the .tra files and selects the events involved in a certain set of detectors was

created.

In figure 3.27 it is presented the ratio of events that interact, through Compton scattering, with a given detector or set of detectors. This ratio corresponds to all reconstructed events, without applying any event selection such as the ARM cut. The detectors are referred by their detecting element instead of their sub-system name, i.e., the tracker is referred to Si, the low-energy calorimeter as CZT and the high-energy calorimeter as CsI. The bottom (CZT_B) and side (CZT_S) components of the low-energy calorimeter are analyzed separately.

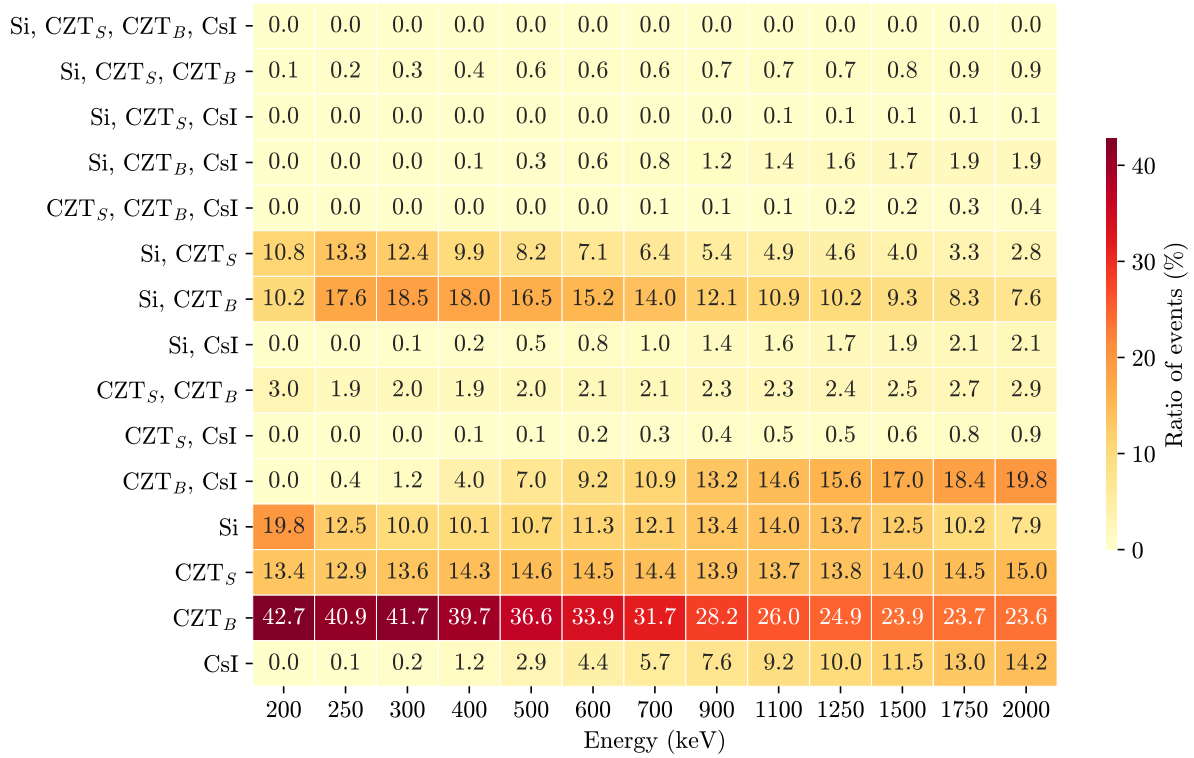

Figure 3.27: Ratio of events that interact with a given detector or set of detectors.

It can be observed that:

- The bottom low-energy calorimeter is the detector where more photons interact, and that as the energy of the photons increases its ratio of detection decreases, while it increases in the high-energy calorimeter.
- The high-energy ratio of detection on the high-energy calorimeter is considerable and explains the increase of the efficiency in the all triggers geometry when compared with the base triggers geometry that does not trigger events that happen uniquely on the high-energy calorimeter.
- The ratio of events on the side low-energy calorimeter stays fairly constant for the presented energy range.
- Regarding interactions on different types of detectors, the tracker and the low-energy

calorimeter, both the bottom and the side calorimeter, have a higher weight on the detection of low-energy photons, but its weight decreases with the increase of the energy of the photons.

- As the energy of the photons increases, the bottom low-energy calorimeter and the high-energy calorimeter have a higher weight on the detection of photons.
- Interactions generated in three or more detectors have a low contribution to the detection of photons in the studied energy range.

In figures 3.28 and 3.29 are presented the modulation factor computed with interactions in a single detector and in a pair of detectors, respectively, and the respective efficiencies are presented in figures 3.30 and 3.31.

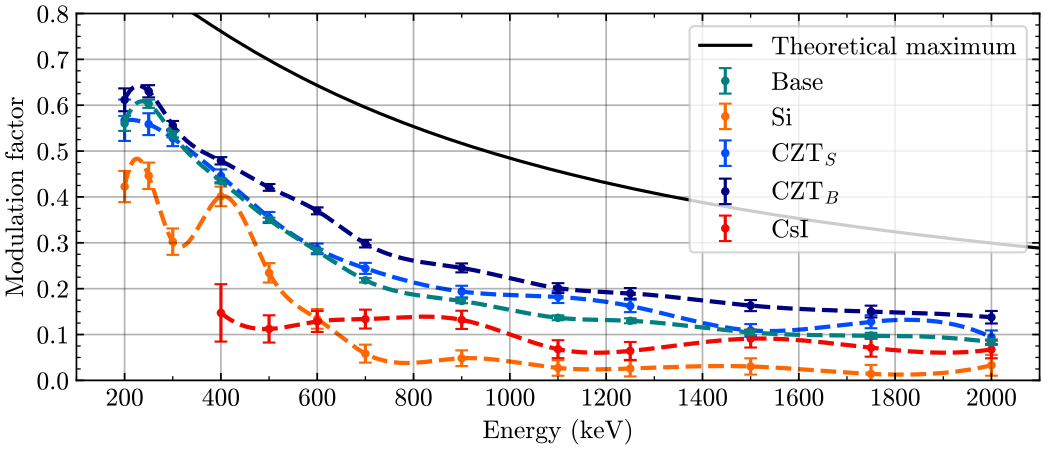

Figure 3.28: Modulation factor as a function of the energy of the photons, computed for events that interacted in a single detector type.

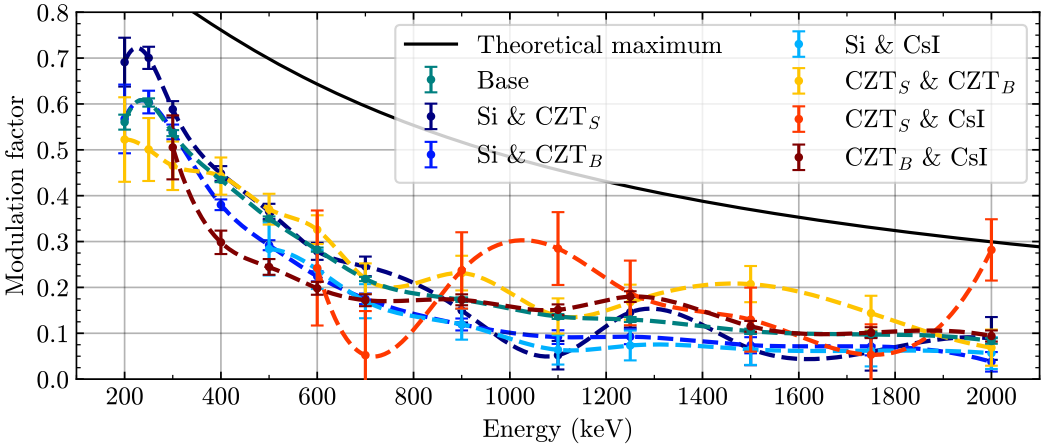

Figure 3.29: Modulation factor as a function of the energy of the photons, computed for events that interacted in a pair of different detectors.

From figure 3.28 it can be observed that the bottom low-energy calorimeter is the detector with the highest modulation factor. This detector consists of a single plane with a height of 4 cm, and the photons that scatter exclusively on this detector through Compton scattering have high scattering angles, contributing with a high modulation factor. The modulation factor of the side low-energy calorimeters is also high. This may be due to a high thickness of the detector and a good spacial resolution from the CZT bar detectors. From figure 3.29 it can be observed that the detector pairs that contribute with a higher modulation factor are the ones that are not positioned directly above each other, such as the side low-energy calorimeter and the tracker, the side low-energy calorimeter and the bottom low-energy calorimeter, and the side low-energy calorimeter and the high-energy calorimeter. As these detectors are not vertically aligned, they allow for the detection of photons that scatter close to right angles.

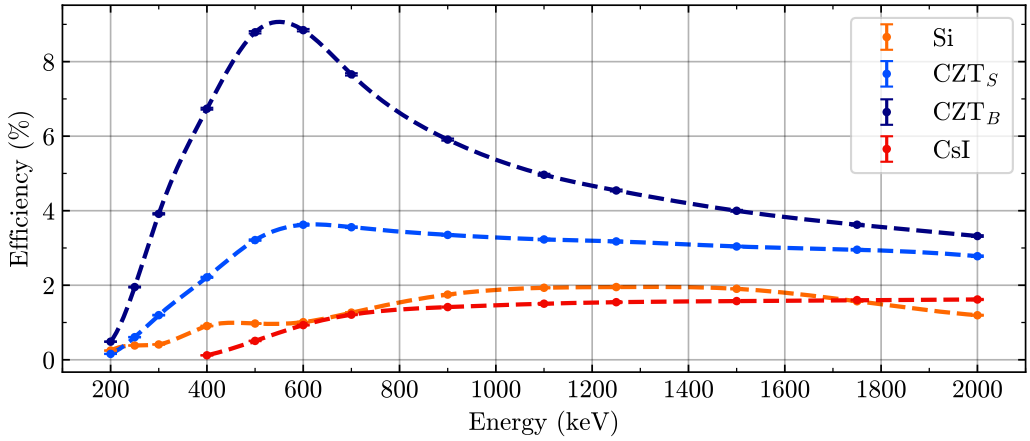

Figure 3.30: Efficiency as a function of the energy of the photons, computed for events that interacted in a single detector type.

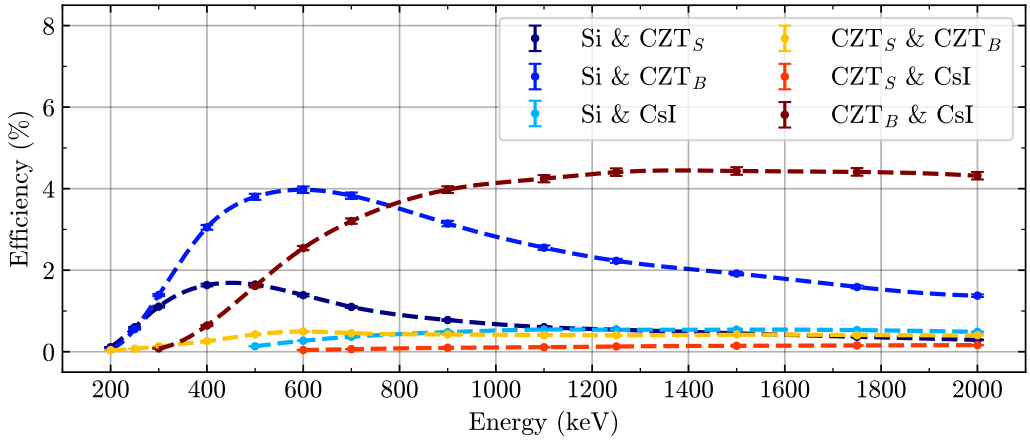

Figure 3.31: Efficiency as a function of the energy of the photons, computed for events that interacted in a pair of different detectors.

From figure 3.30, it is confirmed that the low-energy calorimeter is the detector that has the highest contribution for the detection of the photons. For low-energy photons, the contribution of the high-energy calorimeter is low, having its influence enhanced with the increase of the energy of the photons. As the low-energy calorimeter is a thick detector of high atomic number, it is expected that the photons interact with it, but as the energy of the photons increases, so does their mean free path, increasing the influence of the high-energy calorimeter in their detection. From figure 3.31 it can be observed that, for low-energy photons, the pair of detectors that show the highest efficiency is the tracker and the bottom low-energy calorimeter, while the bottom low-energy calorimeter and the high-energy calorimeter pair present higher efficiency for high-energy photons.

3.4.8 Scattering angle selection

The effects of the scattering angle of the photons on the value of the modulation factor were discussed in section 2.3.1. The modulation factor varies with the scattering angle, reaching a maximum for scattering angles close to 90° in the keV range. Therefore, a study was performed to evaluate the effects of event selection, based on the scattering angle, on the modulation factor and efficiency of the instrument. In order to do this, it was created a Python script that reads the .tra files and selects the events by the scattering angle. The scattering angle is computed by the Compton equation (equation 2.6), using the energies deposited in the detectors by the photons.

In figure 3.32 are presented the angles that correspond to a modulation factor above a given fraction of the maximum attainable modulation factor, as a function of the energy of the photons. These correspond to the colored areas of the plot.

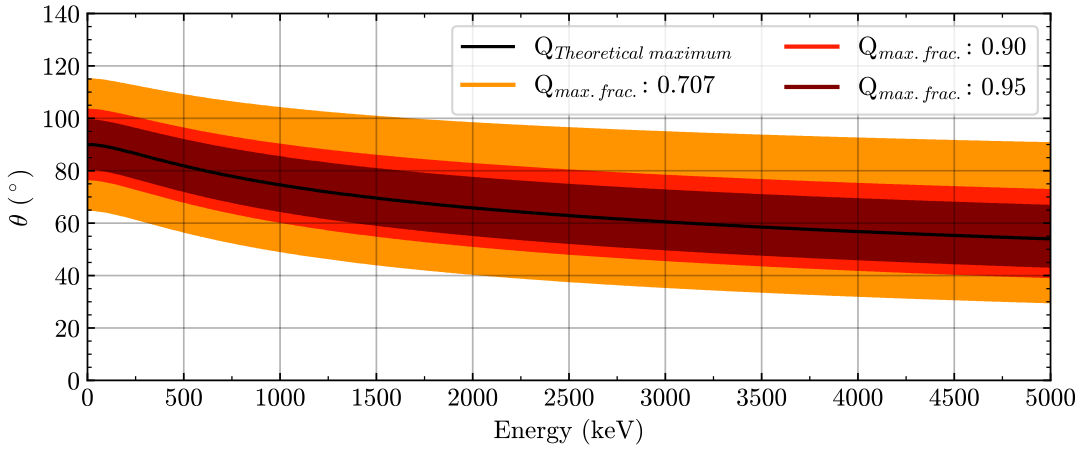

Figure 3.32: Scattering angles of a Compton interaction that correspond to the maximum attainable modulation factor, as a function of the energy of the photons. It is also presented, as colored areas, the scattering angles that correspond to a modulation factor above a fraction of the maximum attainable modulation factor.

In figures 3.33 and 3.34 are presented the modulation factor and efficiency, respectively, as a function of the energy of the photons, that resulted from the event selection described above. As expected, the selection through the scattering angle increases the modulation factor of the instrument and decreases its efficiency. As the event selection becomes more restraining, the higher the modulation factor becomes, converging to its theoretical maximum. A small ARM cut, alongside the scattering angle event selection, could provide an even higher modulation factor. There is a trade-off between the modulation factor of the instrument and its efficiency. When comparing the modulation factor and the efficiency at, for example, 600 and 1100 keV, for the "No angle selection" and the "$Q_{max.frac.}$: 0.707" curves, at 600 keV the modulation factor increases by a factor of $\sim 1.5\times$, while the efficiency decreases $\sim 2.2\times$, and at 1100 keV the modulation factor increases $\sim 1.9\times$, while the efficiency decreases $\sim 3.8\times$.

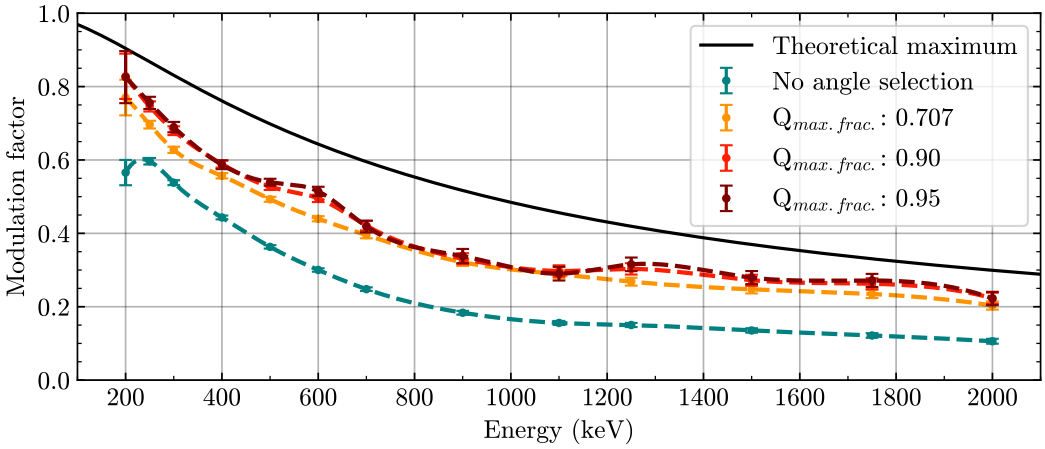

Figure 3.33: Modulation factor as a function of the energy of the photons, computed for events selected through the scattering angle of the first Compton interaction.

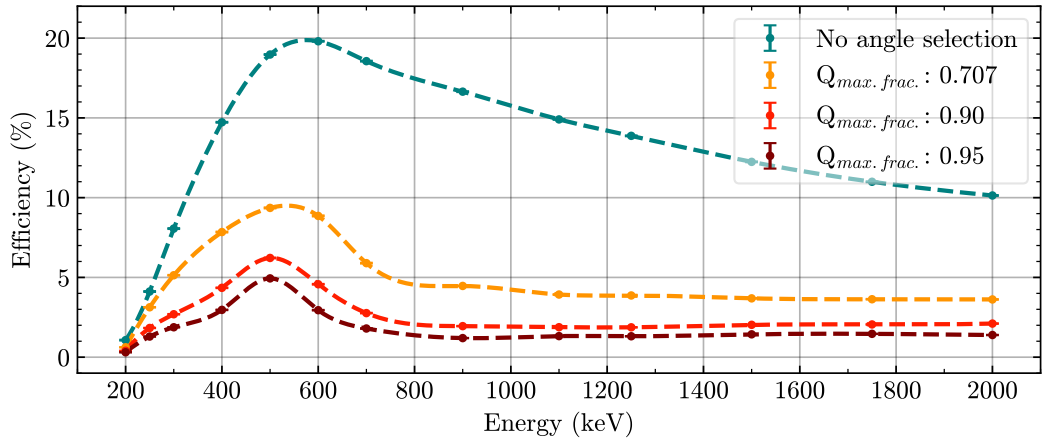

Figure 3.34: Efficiency as a function of the energy of the photons, computed for events selected through the scattering angle of the first Compton interaction.

3.4.9 Background

Space-based γ-ray telescopes are exposed to background radiation, which generates background signals that dominate the ones from the sources up to two orders of magnitude [50]. The background radiation is caused by cosmic-rays, such as photons, α-particles, protons, neutrons, electrons, positrons, etc., and due to radiation in the Earth orbital environment, the *albedo radiation*, which consists of charged particles trapped on the magnetosphere of the Earth and radiation produced in the interaction of cosmic-rays with the upper atmosphere of the Earth. The background radiation contributes to the background signals, not only with instantaneous signals generated by the interaction of the radiation with the detectors, but also from delayed emissions due to the activation of the instrument.

Zoglauer et al. [50] developed a simulation tool, for Cosima, that simulates the background radiation. It succeeds the MGGPOD, which already proved to be an efficient tool, modeling successfully the instrumental background of the SPI and RHESSI instruments [52].

The MGGPOD is based on packages that accurately estimate the background components such as, for example, galactic cosmic-rays, solar flares in the near-Earth environment and trapped protons fluxes. The MGGPOD also uses empirical data and analytical models to simulate the neutron components, electron and positron cosmic-rays, difuse photons and albedo photon components. It also accounts for the delayed emissions provenient from the activation of the instrument [52]. These packages are no longer maintained [50], which motivated the development of the Cosima background simulation tool. The background simulator of MEGAlib simulates the *prompt* interactions and estimates the *build-up* of radioactive isotopes generated by hadron interactions. Then it simulates the delayed emission of the isotopes and the emissions from the elements in the decay chains. As can be observed in figure 3.35, the background simulator of MEGAlib can accurately estimate the background radiation. The activation components of the simulation still needs development, for example reviewing the cross-sections for generated nuclei in Geant4 and validate the code with activation measurements on-ground and space-based telescopes [50].

The simulations allow the evaluation of the effects of the events reconstruction and selection algorithms on the minimization of background levels, as it is shown in figure 3.36. It also allows for the optimization of the instrument design, exploring the effects of using different detectors and different geometries [18, 52].

AMEGO background simulations with MEGAlib

In this section it is studied the background signals induced in the AMEGO instrument. The simulations were performed with the base trigger geometry (section 3.4.3), by the AMEGO team and the simulation files are available in the AMEGO GitHub. The background simulations took several days to compute while running on parallel threads, taking more than 20000 hours/core to complete.

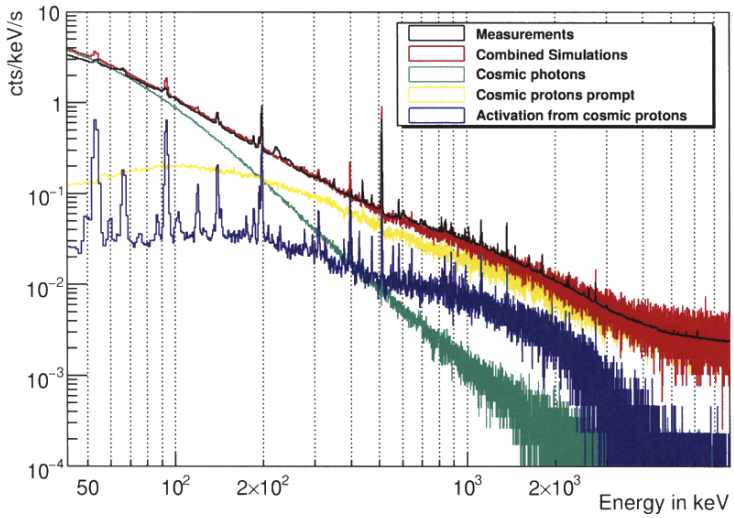

Figure 3.35: Comparison between the measured and simulated background spectra of the Transient Gamma-Ray Spectrometer (TGRS). The simulations were performed with the MEGAlib background simulation tool. The TGRS is a germanium detector designed to perform gamma-ray spectroscopy of transient gamma-ray sources, such as GRBs and solar flares [50]. This detector flies on board the Wind spacecraft and can detect photons with energies between 25 keV and 8 MeV. Adapted from [50].

The MEGAlib background simulation tool allows for the estimation of the background for different orbits. The parameters used for the AMEGO orbit are: radiation with energy between 10^1 and 10^9 keV and an orbit with an altitude of 575 km and inclination of 6°. The various radiation components that contribute to the total background are simulated separately, that include a photonic, a leptonic, a hadronic and a trapped hadronic component. The hadronic and trapped hadronic prompt component contribute to prompt signals and are used to estimate the activation of the materials of the instrument, generating a list of the isotopes created. After the prompt simulations, the build-up simulations are run, which estimate the activation of the materials of the instrument after a certain exposure time to these radiations. Finally, the decay simulations are run, which allow the estimation of the contribution of the activation of the instrument to the background signals. Each of the prompt and decay simulations, simulate 1 hour of irradiation. The activation simulations correspond to an activation time of 1 year. The trapped radiation prompt component is not included in the total background, as this component is only present during the passage on the South Atlantic Anomaly, where the instrument is turned off.

The figures 3.37 and 3.38 correspond to the spectra obtained from the simulation files while applying the ARM cut event selection. The spectra from figure 3.37 is computed with an ARM cut of 15°, while the spectra from figure 3.38 is computed with an ARM cut of 30°. It can be observed that at low-energies, the background is dominated by the photonic background and, as the energy increases, the activation of the instrument has the most influence in the background rates. In table 3.5 it is presented the rate of Compton background events induced in the AMEGO, according to the simulations. The background was calculated for different

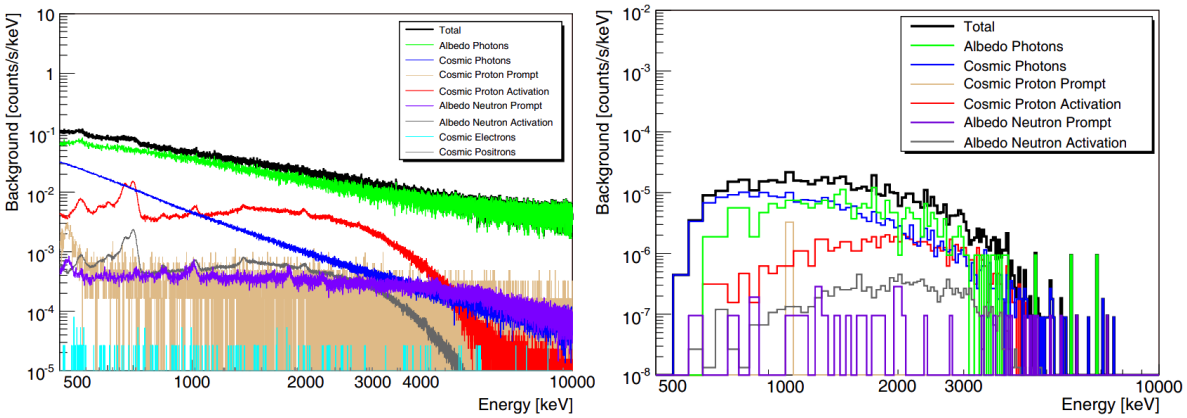

Figure 3.36: Simulations of the induced Compton background signals in MEGA, computed with MEGAlib. Left: Spectrum of each individual background component before event reconstruction. Only the trigger critteria is applying an event selection. Right: Background spectra after applying an ARM cut event selection. Adapted from [18].

ranges of energies and for on/off-axis observations. The uncertainties of the background rates are computed by square root of its corresponding value.

From the table 3.5 it can be seen that, as expected, the background rates increase with the increase of the energy range to higher energies, and that these are more intense for a wider ARM cut. It can also observed that the off-axis observations do not affect the background rates significantly.

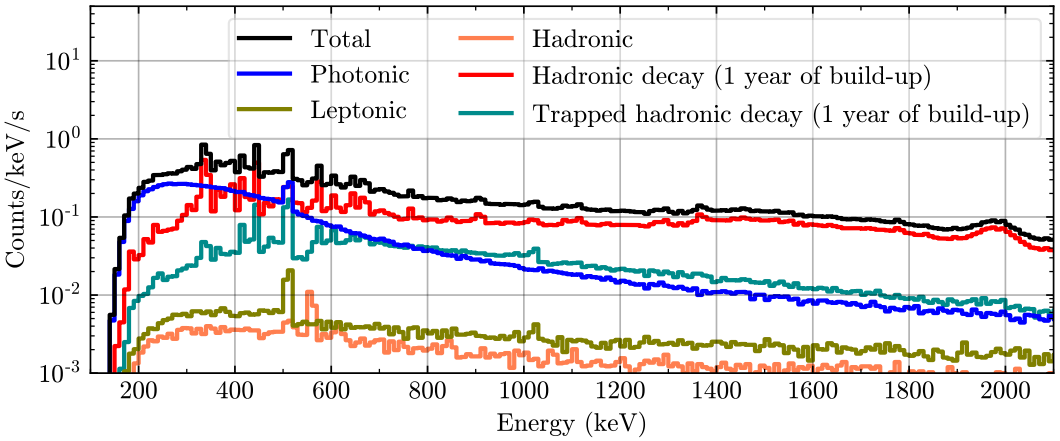

Figure 3.37: Background spectra expected for AMEGO in orbit, for on-axis observations and an ARM $< 15°$.

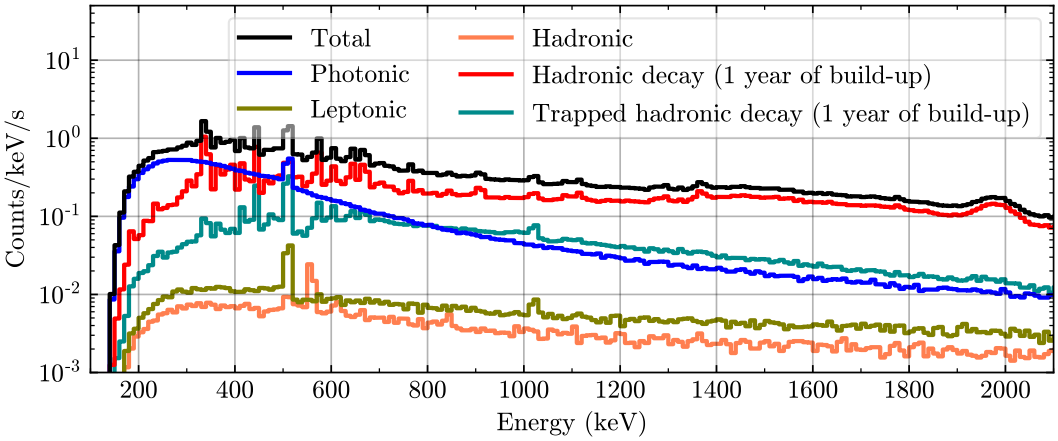

Figure 3.38: Background spectra expected for AMEGO in orbit, for on-axis observations and an ARM $< 30°$.

Table 3.5: Rate of the Compton background events expected for AMEGO, while in orbit, in counts/s units. These rates are presented for different ranges of energies, different ARM cuts and for different angles of incidence.

Energy range (keV)	ARM cut of 30°	ARM cut of 15°
200 to 400	165.58 ± 12.87	85.55 ± 9.25
200 to 500	246.65 ± 15.71	130.56 ± 11.43
200 to 700	383.38 ± 19.58	195.16 ± 13.97
200 to 1000	489.42 ± 22.12	246.41 ± 15.70
200 to 1000 at $\theta = 36.9°$	-	266.55 ± 16.33
200 to 1000 at $\theta = 53.1°$	-	268.12 ± 16.37

3.4.10 Minimum detectable polarization

As mentioned in section 2.3.5, the MDP (calculated by equation 2.22) characterizes the sensitivity of the instrument to polarization, relating the minimum degree of linear polarization that the instrument can measure with its operation conditions and with its properties, such as efficiency and modulation factor.

In order to estimate the MDP for a given source the overall efficiency and modulation factor will be computed within the observation energy range. Each simulation was performed for a total of 2 million triggers. The overall efficiency and modulation factor will vary according to the hardness of the sources and for different ranges of energy, e.g., it is expected to obtain a lower overall modulation factor for harder spectra.

The MDP is determined for the GRB 170817A, for a model of short GRBs (made available by the AMEGO team) and for the Crab. The simulations performed are similar to the ones performed before in the characterization of the modulation factor and efficiency as a function of

the energy of the photons. Instead of using a monochromatic spectra, the spectra of the sources is used, which are subdivided in a set of energy ranges. The relative flux of the spectra of the sources, in relation to the flux at 100 keV, is presented in figure 3.39. The absolute flux, for different energy ranges, is presented in the tables 3.6, 3.8 and 3.10.

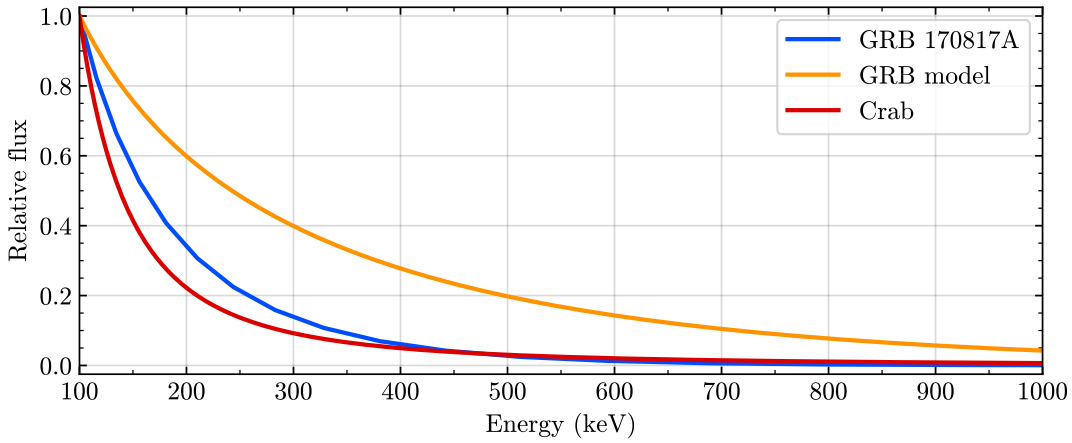

Figure 3.39: Relative flux of the spectra of the GRB 170817A, of the GRB model and of the Crab, in relation to the flux at 100 keV. The presentation of the spectra as a relative flux, allows for a better comparison between the hardness of the spectra.

GRB 170817A

The GRB 170817A simulation model spectrum (figure 3.39) is available in the AMEGO GitHub and is based on a fit from a spectrum observed by the Fermi sattelite [9]. According to the files where the GRB 170817A is defined, the GRB has a duration of 3 seconds.

According to the files, the total flux is 0.700 photons cm^{-2} s^{-1} in the 100 keV to 10 MeV energy range. The fluxes for the simulated energy ranges are presented in table 3.6, and are computed from the ratio of the integrated area between the energies of interest and the full integration of the spectrum. From figure 3.39 and table 3.6, it can be observed that a significant fraction of the flux is lost by neglecting the 100 to 200 keV energy range.

Table 3.6: Average fluxes of the GRB 170817A in different energy ranges.

Energy range (keV)	Flux (photons cm^{-2} s^{-1})
100 to 10^4	0.700
200 to 400	0.223
200 to 500	0.252
200 to 700	0.272
200 to 1000	0.278

The parameters of interest that result from the simulations, i.e., the modulation factor and

efficiency of the instrument, are presented in table 3.7. As expected, a smaller ARM cut leads to a higher modulation factor and smaller efficiency. It is also observed, that higher modulation factors are obtained in the lower energy ranges. This is expected, as the modulation factor decreases with the increase of the energy of the photons. From the plot of the efficiency of the instrument as a function of the energy (figure 3.20), it was observed that the efficiency is higher at greater energies, with a maximum at 600 keV. From table 3.7, it is also observed greater efficiencies in the higher energy ranges.

Table 3.7: Overall modulation factors and efficiencies of AMEGO, for the spectrum of the GRB 170817A.

	Modulation factor		Efficiency (%)	
Energy range (keV)	ARM $< 15°$	ARM $< 30°$	ARM $< 15°$	ARM $< 30°$
200 to 400	0.54 ± 0.01	0.51 ± 0.01	5.93 ± 0.01	8.14 ± 0.01
200 to 500	0.50 ± 0.01	0.48 ± 0.01	7.21 ± 0.01	9.87 ± 0.01
200 to 700	0.47 ± 0.01	0.45 ± 0.01	8.11 ± 0.01	11.10 ± 0.01
200 to 1000	0.46 ± 0.01	0.44 ± 0.01	8.29 ± 0.01	11.36 ± 0.02

In figure 3.40 it is presented the MDP as function of the observation time, with the source on-axis. The MDP is computed with the background rates found in table 3.5, the fluxes of the source found in table 3.6, and the modulation factors and efficiencies presented in table 3.7.

As it can be seen, an MDP of $\sim 55\%$ is expected for the GRB 170817A, and that different energy ranges result in different MDPs, with the best value achieved in the 200 to 500 keV energy range, for an ARM cut of 30°, and the worst in the 200 to 1000 keV energy range. This is due to a trade-off between the value of the flux, the background rates, the modulation factor and efficiency obtained for the different energy ranges. Comparing the mentioned energy ranges, the flux of the first is $\sim$10% smaller than the second, and the background rates are $\sim$47% lower. In the 200 to 500 keV energy range, the modulation factor is 0.48 ± 0.01 and the efficiency is $(9.87 \pm 0.01)\%$, while in the 200 to 1000 keV energy range, the modulation factor is 0.44 ± 0.01 and the efficiency is $(11.36 \pm 0.02)\%$. The decrease of the efficiency and flux of the source are compensated by the increase of the modulation factor and decrease of the background rates, leading to a better MDP. Comparing, for example, the 200 to 400 keV with the 200 to 1000 keV energy range, it is also obtained a higher modulation factor and smaller background rates, and lower efficiency and lower flux, but the MDP is very similar for the two energy ranges, indicating that, while some parameters are optimized for the increase of the sensitivity to polarization, these are easily counterbalanced by the contribution of the other parameters that worsen the sensitivity.

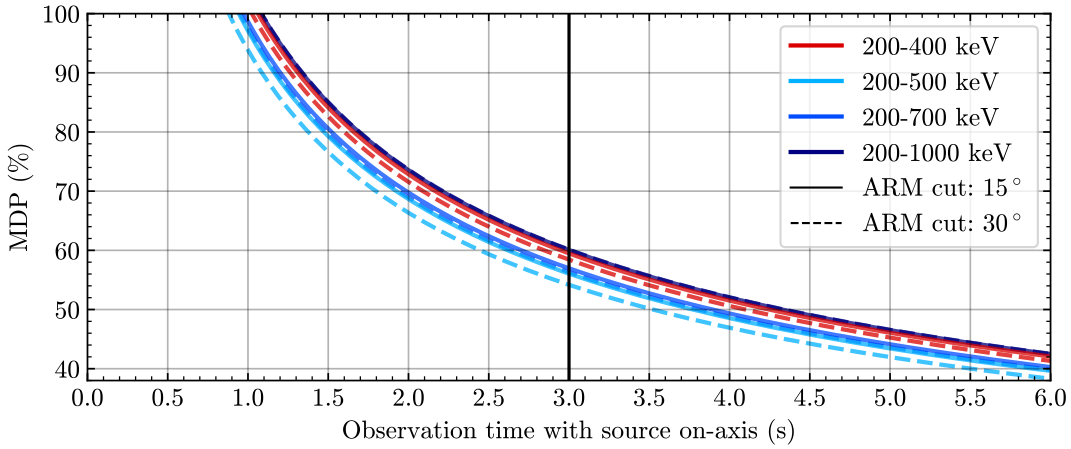

Figure 3.40: MDP for on-axis observations of the GRB 170817A as a function of the observation time. The GRB is modeled to have a total duration of 3 s.

GRB models

The GRB models were made available by the AMEGO team. These represent a range of short GRBs, designated as "Amp 1", "Amp 5", "Amp 10", "Amp 15" and "Amp 20". They all have the same spectrum shape, represented in figure 3.39, and have a duration of 1 s. It can be seen that the spectra from the GRB models is harder than the GRB 170817A spectrum. The only difference between the different GRBs in the model is their fluxes. These are presented in table 3.8.

Table 3.8: Average fluxes of the GRB models in different energy ranges.

	Flux (photons cm^{-2} s^{-1})				
Energy range (keV)	Amp 1	Amp 5	Amp 10	Amp 15	Amp 20
100 to 1000	1.008	5.006	10.012	15.018	20.024
200 to 500	0.459	2.278	4.555	6.833	9.111
200 to 700	0.585	2.903	5.807	8.710	11.614
200 to 1000	0.675	3.349	6.698	10.047	13.396

Only one simulation was performed per energy range, as the spectra shape is the same for all models, only varying their flux. The modulation factors and efficiencies computed from these simulations are presented in table 3.9.

Table 3.9: Overall modulation factors and efficiencies of AMEGO, for the spectrum of the GRB models, computed for an ARM cut of 15°.

Energy range (keV)	Modulation factor	Efficiency (%)
200 to 500	0.48 ± 0.01	9.21 ± 0.01
200 to 700	0.41 ± 0.01	11.43 ± 0.02
200 to 1000	0.37 ± 0.01	12.25 ± 0.02

The MDP is then computed for each energy range, taking into consideration the expected background rates, in the corresponding energy range, the respective flux of the source and the modulation factor and efficiency of the instrument, obtained for these spectra. The MDP, as a function of the observation time, with the source on-axis, is presented in figure 3.41.

The better MDPs are obtained for the wider energy range, i.e., from 200 to 1000 keV. As the modeled GRBs have a total duration of 1 second, the MDP for the "Amp 1", "Amp 5", "Amp 10", "Amp 15" and "Amp 20", are ∼52%, ∼21%, ∼15%, ∼12% and ∼10%, respectively. As the spectra of the different models is the same, for the same energy range, the background rates, the modulation factor and the efficiency remain constant, and only the flux of the source varies. This is the only factor that makes the MDP differ for the different models and same observation time.

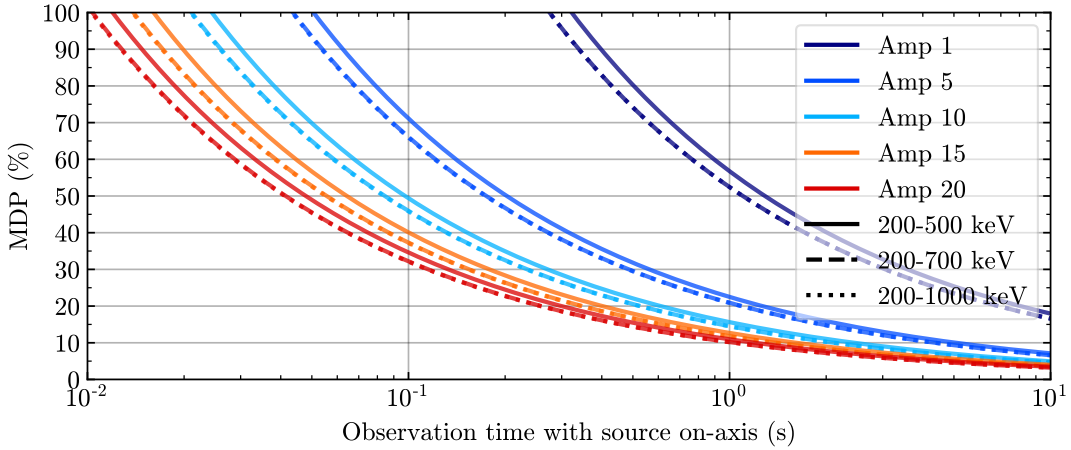

Figure 3.41: MDP for on-axis observations of the GRB models, as a function of the observation time, computed for an ARM cut of 15°. The GRBs are modeled to have a total duration of 1 second. The dotted lines overlap with the dashed ones.

In the case of the GRB 170817A, it was observed that a better MDP is obtained with a narrower energy range, more specifically the 200 to 500 keV range. This is not observed for the GRB models. One possible explanation may be the harder spectra. As more photons of high-energy are being emitted, when narrowing the energy range, a bigger fraction of the total flux is being cut, causing the MDP to worsen.

Other differences that can be observed when comparing the softer spectrum of the GRB 170817A with the harder spectrum of the GRB models, for the same energy range, are the modulation factor and efficiency. For example, the modulation factor in the 200 to 1000 keV energy range, for the GRB 170817A (for a 15° ARM cut) and for the GRB models, is 0.46 ± 0.01 and 0.37 ± 0.01, respectively, and the efficiencies are $(8.29 \pm 0.01)\%$ and $(12.25 \pm 0.02)\%$, respectively.

Crab

As mentioned in section 1.3.1, in [5] it was determined that the Crab spectrum, in the 50 keV to 1000 keV energy range, can be modeled by a power-law of index 2.17 and a normalization constant of 10.74. This spectrum is represented in figure 3.39. The fluxes of this source are computed through the integration of the power-law between the energies of interest, and are presented in table 3.10.

Table 3.10: Crab average fluxes in different energy ranges.

Energy range (keV)	Flux (photons cm^{-2} s^{-1})
200 to 400	0.010
200 to 1000	0.016

The modulation factors and efficiencies, computed from the simulations, are presented in table 3.11.

Table 3.11: Overall modulation factors and efficiencies of AMEGO, for the spectrum of the Crab.

	Modulation factor		Efficiency (%)	
Energy range (keV)	ARM $< 15°$	ARM $< 30°$	ARM $< 15°$	ARM $< 30°$
200 to 400	0.53 ± 0.01	0.50 ± 0.01	6.14 ± 0.01	8.43 ± 0.01
200 to 1000	0.40 ± 0.01	0.39 ± 0.01	10.26 ± 0.01	14.12 ± 0.02
200 to 1000 at $\theta = 36.9°$	0.38 ± 0.01	-	6.25 ± 0.01	-
200 to 1000 at $\theta = 53.1°$	0.38 ± 0.01	-	5.73 ± 0.01	-

In figure 3.42 it is presented the MDP as a function of the observation time, for on-axis observations, and in figure 3.43, it is presented the MDP for off-axis observations in the 200 to 1000 keV range. In figure 3.44 it is presented the MDP for Crab-like sources as a function of the observation time, for on-axis observations in the 200 to 1000 keV energy range.

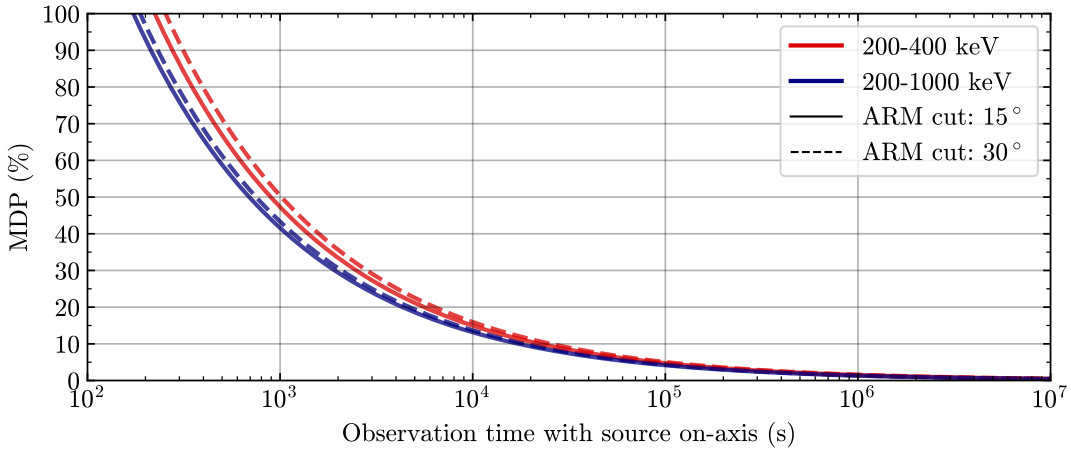

Figure 3.42: MDP for on-axis observations of the Crab as a function of the observation time.

From the figure 3.42, it can be observed that no polarization levels can be detected for an observation time below ∼200 s. At 10^3 s (∼ 17 minutes) the MDP is ∼42%, at 10^4 s (∼ 2.8 hours) it is ∼13%, at 10^5 s (∼ 25 hours) it is ∼4%, and at 10^6 s (∼ 11.2 days) it is ∼1%, in the 200 to 1000 keV energy range, for an ARM cut of 15°.

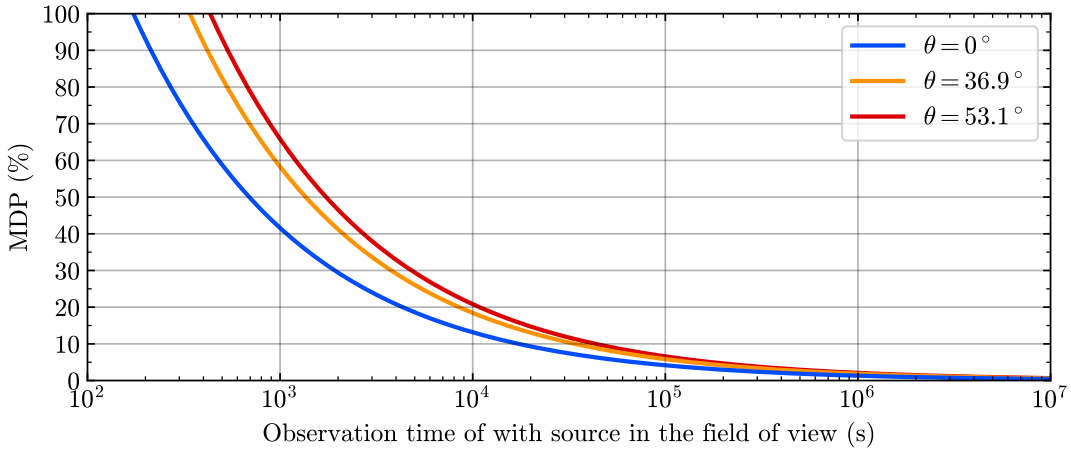

Figure 3.43: MDP for off-axis observations of the Crab, in the 200 to 1000 keV energy range, as a function of the observation time, computed for an ARM cut of 15°.

From figure 3.43 it can be observed that the off-axis observations deteriorate the MDP, but that for long observation times, the effects of the off-axis observations are minimized, since long exposure observation times provide enough statistics to determine the polarization level with a 99% confidence level. In table 3.11 it can be seen that the modulation factor stays approximately constant for the different angles, while the efficiency tends to decrease for wider angles. The off-axis observation effects on the modulation factor and efficiency were studied in section 3.4.6, and are in agreement with these results. Since the background rates, the flux of the source, and modulation factor stay approximately constant for the off-axis observations, the increase of the MDP is explained by the decrease of the efficiency.

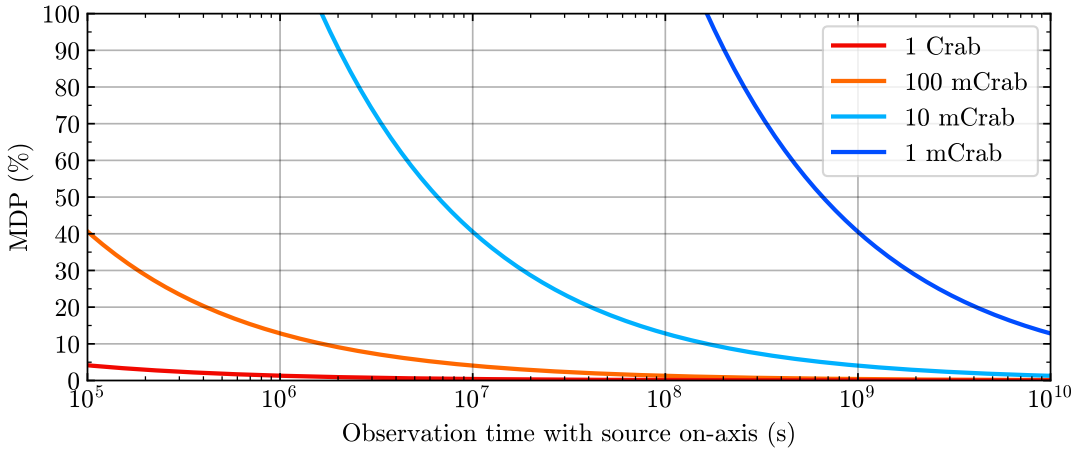

Figure 3.44: MDP for on-axis observations of the Crab-like sources, in the 200 to 1000 keV energy range, as a function of the observation time, computed for an ARM cut of 15°.

As mentioned in section 3.1, the AMEGO mission, if concretized, will observe the sky, in a survey mode, for at least 5 years. The instrument is required to have a FOV of at least 2 sr, which translates to an observation of ∼16% of the sky at each instant. An approximation for the total observation time for a permanent source like the Crab, during a 5-year mission (1 year $\approx 3.2 \times 10^7$ s), can be obtained through:

$$\text{Total observation time of a 5-year mission} \approx \frac{2}{4\pi} \times 5 \times 3.2 \times 10^7 \approx 2.5 \times 10^7 \text{ s}$$

From figure 3.44, it can be observed that during the 5-year mission, it will be possible to perform polarimetric measurements of sources with a flux down to ∼10 mCrab. At the end of the this mission, the MDP for 1 Crab is ∼0.3%, for 100 mCrab it is ∼2.6% and for 10 mCrab it is ∼25.6%.

3.5 AMEGO-X

The All-sky Medium Energy Gamma-ray Observatory eXplorer (AMEGO-X)[7] [53] is a mission concept that is being proposed as a MIDEX mission. It consists of a smaller version of AMEGO, and the main differences between the two are the number of layers of the tracker, the distance between these layers, and the fact that the low-energy calorimeter is only present in AMEGO. The tracker of the AMEGO-X is composed of 40 layers separated by 1.5 cm and the tracker of AMEGO is composed of 60 layers separated by 1 cm. The lower sensitive volume of the AMEGO-X tracker and the absence of the low-energy calorimeter, translates in lower sensitivities.

During the scope of this work, the AMEGO-X team started to explore a trade study regarding the tracker, studying the implementation of a different technology other than the DSSDs. The tracker trade-study is composed of the so called AstroPix, based on the *ATLASPix*, a

[7] https://asd.gsfc.nasa.gov/amego-x/

pixel detector built for the ATLAS experiment from CERN [54]. In this work, it is presented the modulation factors and efficiencies that are obtained with the base geometry, the tracker of DSSDs, and with the AstroPix tracker. Then, the sensitivity of the instrument with the AstroPix is computed, i.e., the expected background rates and the MDP as a function of the observation time, for the GRB 170817A, the GRB models and the Crab.

3.5.1 AstroPix

The AstroPix is a monolithic silicon pixel detector based on the ATLASPix, a high-voltage complementary metal-oxide-semiconductor (CMOS) detector optimized for the detection of high-energy particles [54]. The main advantage of the CMOS pixels is that they allow for the co-integration of the detector and readout electronics, reducing the noise of the instrument when compared with DSSDs. Also, DSSDs are complex to produce, while the CMOS is a common manufacturing technique used in commercial industry [55]. The lower noise allows for the reduction of the trigger threshold of the tracker to 25 keV [53].

The AstroPix tracker trade-study geometry files are available in the AMEGO GitHub. The main difference between the AMEGO-X base geometry and the AstroPix trade-study is the trigger threshold of the tracker which, as mentioned in section 3.4.3, is 60 and 25 keV, respectively. The lower thresholds allow for the extension of the detection of photons down to 100 keV.

In the remainder of this work, AstroPix will refer to the whole geometry that includes the new tracker, for simplicity.

3.5.2 Modulation factor and efficiency

In this section, it is computed the modulation factor and efficiency of the AMEGO-X base geometry and of the AstroPix. The simulations are similar to the ones performed for AMEGO, but for the AstroPix an additional simulation with 100 keV photons is performed.

In figure 3.45 it is presented the modulation factor of the AMEGO-X base geometry and of AstroPix, and in figure 3.46 are presented their efficiencies.

It can be observed that the modulation factor between the base geometry and the AstroPix differ significantly at low-energies. This will be further discussed in sections 3.5.2.1 and 3.5.2.2.

Comparing the modulation factors between the base geometry of AMEGO-X and AMEGO (figure 3.19), it can be observed that the ones obtained for AMEGO-X are lower than the ones obtained for AMEGO. For example, at 200, 700 and 1100 keV, the modulation factor for AMEGO-X base geometry and for AMEGO are 0.43 ± 0.03 and 0.57 ± 0.03, 0.16 ± 0.01 and 0.25 ± 0.01 , and 0.06 ± 0.01 and 0.16 ± 0.01, respectively. This may be due, to the absence of the low-energy calorimeter that, as seen in section 3.4.7, for AMEGO, is the detector that contributes the most for the high value of the modulation factor.

From figure 3.46 it can be observed that the AstroPix presents higher efficiencies than the base geometry. This may be due to the lower trigger threshold, that allows for more events to

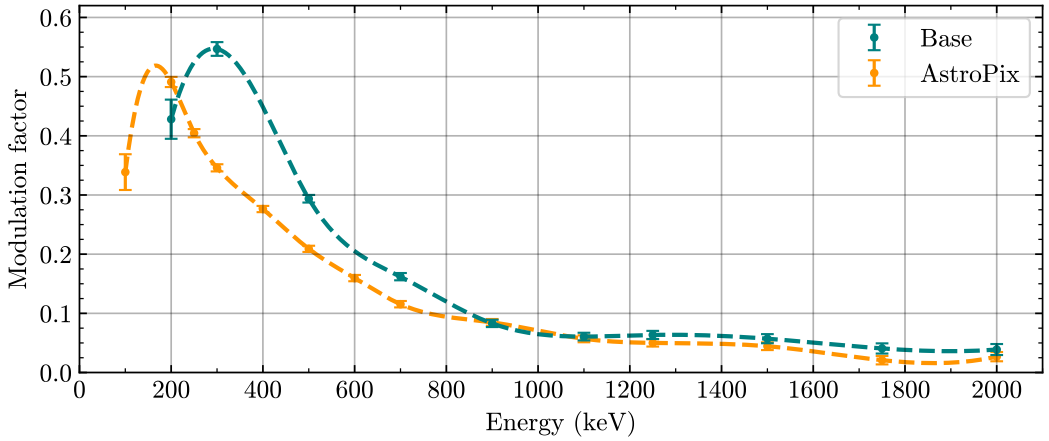

Figure 3.45: Modulation factor as a function of the energy, for the AMEGO-X base geometry and for the AstroPix.

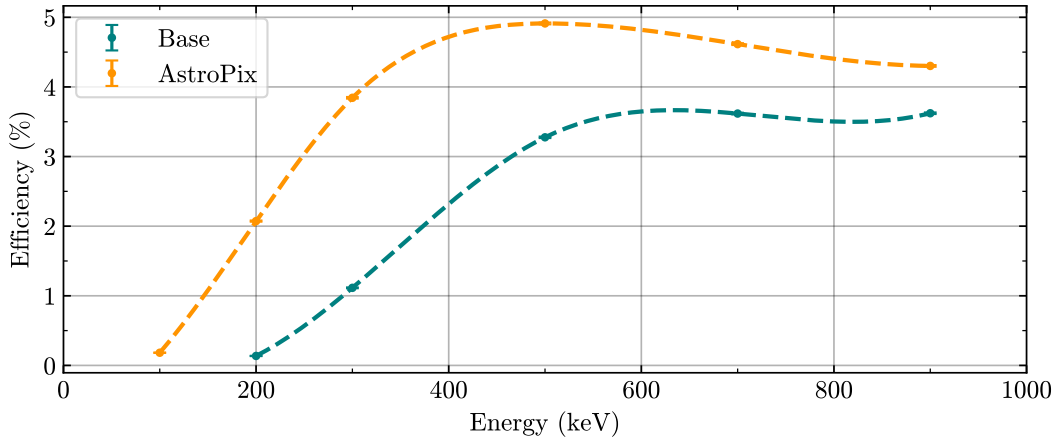

Figure 3.46: Efficiency as a function of the energy, for the AMEGO-X base geometry and for the AstroPix.

pass the event selection. As mentioned in section 2.3, the photons have a higher probability of being scattered at low-angles, transferring a lower amount of energy to the scattered electron, when comparing with a photon that scatters at higher angles. As the trigger threshold is lower, more photons that scatter at low-angles are being measured.

Comparing the efficiencies between AMEGO (figure 3.20) and the base geometry of AMEGO-X, it can be observed that the efficiencies of AMEGO-X are lower than the efficiencies of AMEGO, as expected. The AMEGO-X presents 2/3 of the sensitive volume of the tracker, when compared with AMEGO, and does not have a low-energy calorimeter.

3.5.2.1 Scattering angle distributions

It can be observed that the modulation factor, at low-energies, is lower for the AstroPix. One possible reason for this, is the lower energy of the trigger threshold. As mentioned before, a Compton interaction that transfers a low amount of energy to an electron results in a low

scattering angle, which translates in a low intrinsic modulation factor (as can be seen in figure 2.11). In figure 3.47 it is presented the scattering angles that corresponds to a transference of energy to an electron in a Compton interaction, as a function of the energy of the incident photons. As can be confirmed in the figure, a lower trigger energy translates in lower scattering angles. The energies 25 and 60 keV correspond to the trigger thresholds of the tracker, for the base geometry and AstroPix, respectively.

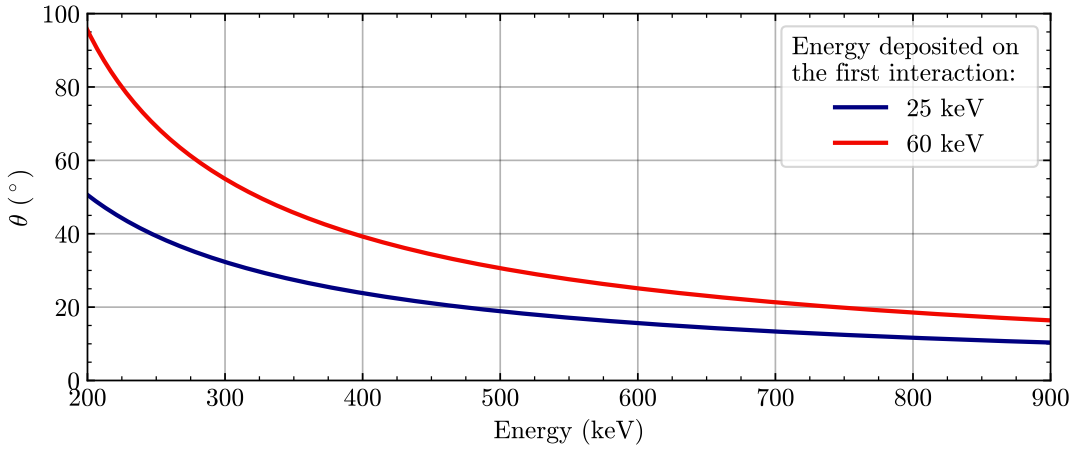

Figure 3.47: Scattering angle of a photon, for different energies transferred to the scattered electron, as a function of the energy of the photons.

In figure 3.48 are presented histograms of the scattering angles of the photons from the simulations. It can be observed that the AstroPix allows for photons with a lower scattering angle, in comparison with the base geometry. This may explain the decrease of the modulation factor and the increase of the efficiency.

3.5.2.2 Energy selection

In order to confirm that the reduction of the AstroPix modulation factor and increase of its efficiency, in comparison with the base geometry, is in fact due to a less demanding event selection based on the trigger threshold of the tracker, an additional trigger threshold is implemented. This trigger is implemented through a Python script that reads the .tra files and selects the events that deposit at least 60 keV (trigger threshold of the base geometry) in the first interaction.

In figure 3.49 it is presented the modulation factor of the base geometry, of the AstroPix geometry and of the AstroPix with the additional event selection. It can be observed that with the implementation of the event selection, the modulation factors at low-energies converge to the base geometry modulation factor values. In figure 3.50 it is presented the efficiencies of these geometries. It is also observed that the efficiencies of the AstroPix, with the additional event selection, converge to the efficiencies of the base geometry.

This study allows to confirm that the trigger threshold of the detectors affect, in fact,

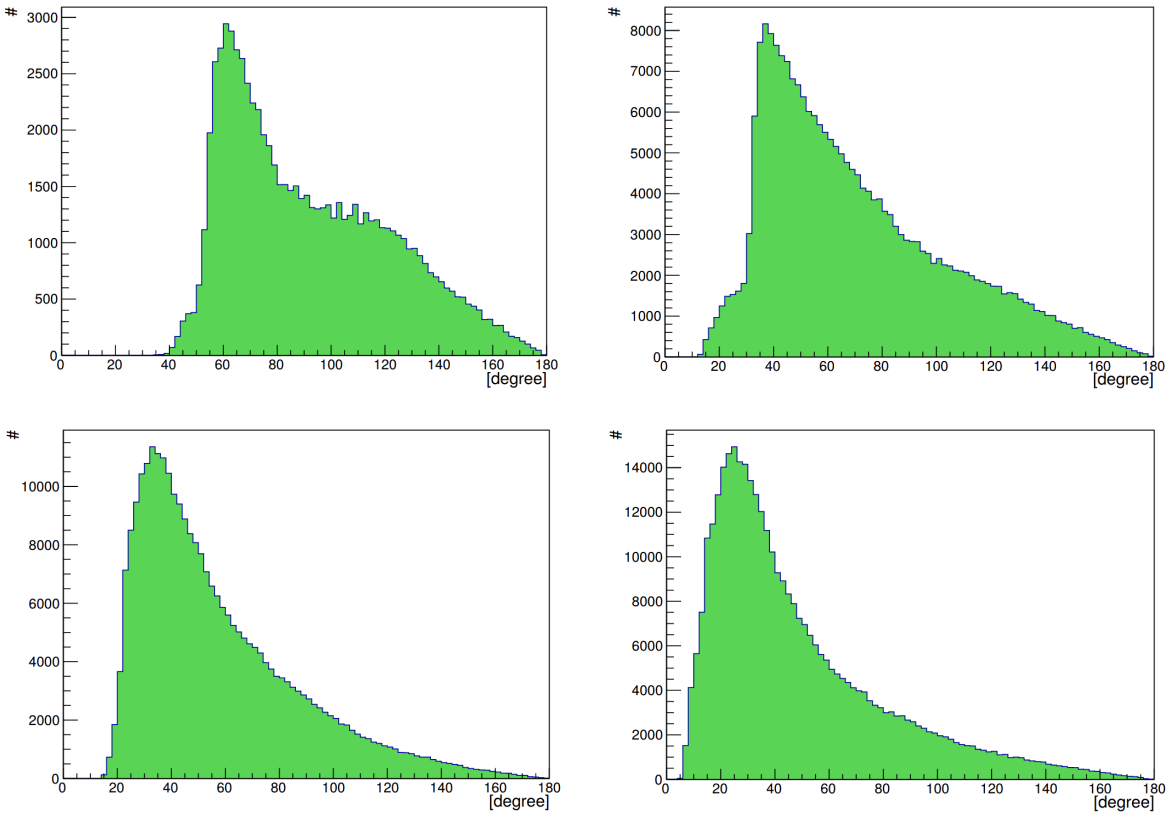

Figure 3.48: Histograms of the scattering angle of the photons detected with the AMEGO-X base geometry and with the AstroPix, for 300 and 700 keV photons. On the top row are presented the histograms obtained with 300 keV photons, and on the bottom row the histograms obtained with 700 keV photons. On the left column the histograms are obtained with the base geometry and on the right column with the AstroPix.

the modulation factors and efficiencies of the instrument, and that a trade-off between these parameters exists. It indicates that the lowering of the modulation factor of the AstroPix may be due to its "dilution", due to selection of events with low intrinsic modulation factor. It should be noted that at 200 keV the AstroPix presents better modulation factors than the base geometry.

The AstroPix allows to extend the operation of AMEGO-X to 100 keV. This benefits its sensitivity to polarization, as will be further discussed in section 3.5.4. It also shows versatility, as it can have a similar performance to the base geometry of AMEGO-X through data analysis.

3.5.3 Background

The background simulations, for the AstroPix geometry, were performed by the AMEGO team and are available at the AMEGO GitHub. The analysis performed for AstroPix is the same as the one performed for AMEGO.

In figure 3.51 are presented the spectra obtained from the simulation files, while applying an ARM cut of 15°. In table 3.12 it is presented the background rates expected for different

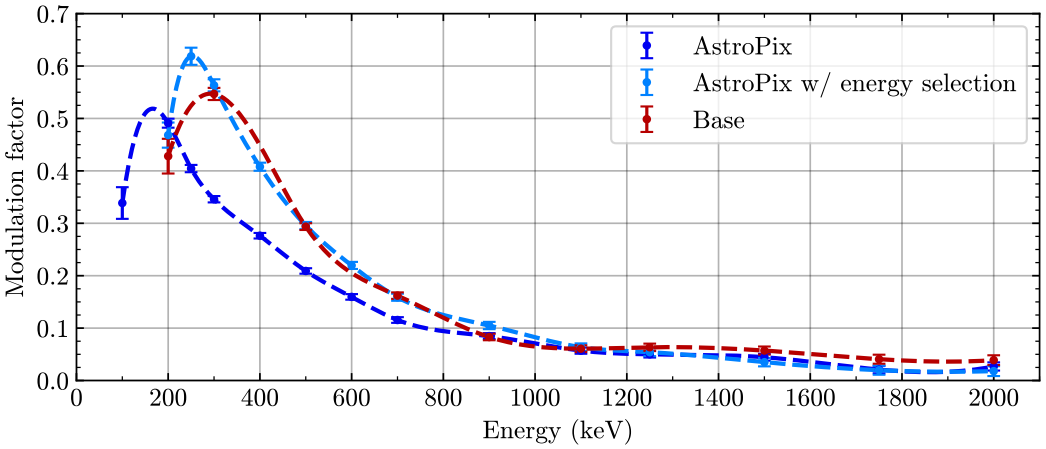

Figure 3.49: Modulation factor as a function of the energy, for the AMEGO-X base geometry, for AstroPix and for AstroPix with an additional event selection, that rejects the events that transfer < 60 keV in the first Compton interaction.

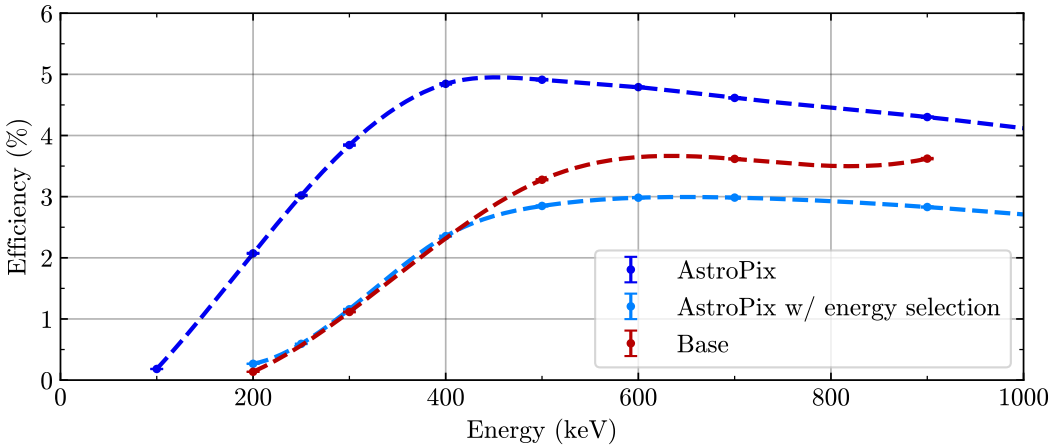

Figure 3.50: Efficiency as a function of the energy, for the AMEGO-X base geometry, for AstroPix and for AstroPix with an additional event selection, that rejects the events that transfer < 60 keV in the first Compton interaction.

energy ranges and ARM cuts. The background rates are lower than the obtained for AMEGO (table 3.5), even for the wider energy range of AMEGO-X. This may be explained by the absence of the low-energy calorimeter, which is a medium of high-atomic number and contributes to the background due to its activation. The lower detector volume, and therefore lower efficiency, of AMEGO-X, when comparing with AMEGO, is another factor that explains the lower background rates.

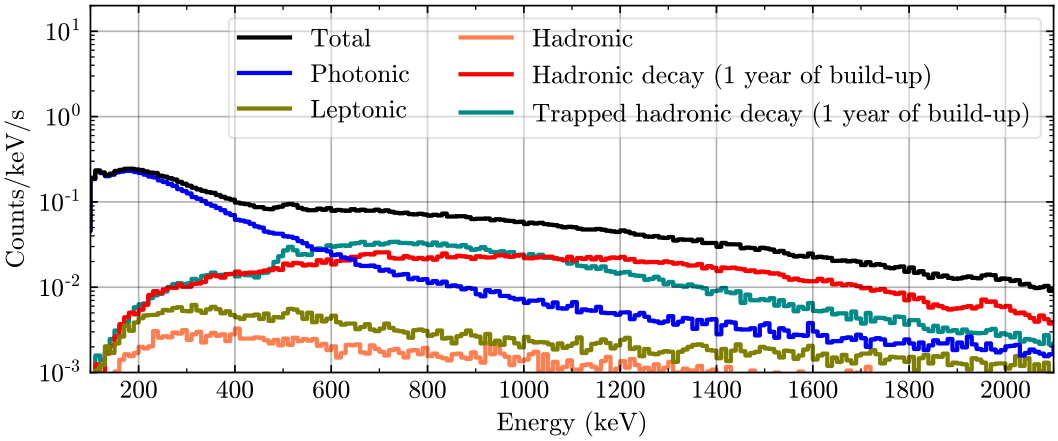

Figure 3.51: Background spectra expected for AMEGO-X in orbit, for on-axis observations and an ARM $< 15°$.

Table 3.12: Rate of the Compton background events expected for AMEGO-X, while in orbit, in counts/s units. These rates are presented for different ranges of energies and ARM cuts.

Energy range (keV)	ARM cut of 30°	ARM cut of 15°
125 to 225	47.94 ± 6.92	23.06 ± 4.80
200 to 400	62.07 ± 7.88	32.98 ± 5.74
100 to 500	125.26 ± 11.19	64.53 ± 8.03
100 to 700	155.31 ± 12.46	81.07 ± 9.00
100 to 1000	192.41 ± 13.87	101.46 ± 10.07

3.5.4 Minimum detectable polarization

The MDP computations for the AMEGO-X, more specifically the AstroPix geometry, are performed in a similar way to the ones for AMEGO. The same simulations are implemented, only the energy ranges vary. As seen in section 2.3.5, the MDP for AMEGO is affected by the fact that the observations are only performed for energies above 200 keV, rejecting a considerable fraction of the flux of the sources. In contrast, AMEGO-X can detect photons with energies down to 100 keV, offering an operation range that extends to lower energies.

Therefore, the MDP obtained with AMEGO-X is shaped by its wider operation range for low-energies and lower modulation factor, efficiency and background rates, when comparing with AMEGO. The MDP for different sources is estimated.

GRB 170817A

The fluxes of the Crab, for the simulated energy ranges, are presented in table 3.13. It can be observed that the fluxes from the energy ranges that start at 100 keV, are higher than the fluxes that start at 200 keV (table 3.6). For example, the wider energy range simulated with

AMEGO is 200 to 1000 keV, which corresponds to a flux of 0.272 photons cm^{-2} s^{-1}, while the wider energy range simulated with AMEGO-X is 100 to 1000 keV, which corresponds to a flux of 0.699 photons cm^{-2} s^{-1}.

Table 3.13: Average fluxes of the GRB 170817A for the energy ranges used in the simulation with AMEGO-X.

Energy range (keV)	Flux (photons cm^{-2} s^{-1})
100 to 10^4	0.700
125 to 225	0.323
200 to 400	0.223
100 to 500	0.674
100 to 700	0.694
100 to 1000	0.699

In table 3.14 are presented the modulation factors and efficiencies obtained from the different energy ranges. It can be observed that the modulation factors and efficiencies obtained with the AMEGO-X are lower than the ones obtained with AMEGO (table 3.7). For example, comparing the values of these parameters, obtained in the 200 to 400 keV energy range and ARM$< 15°$, for AMEGO-X and AMEGO, it is obtained a modulation factor of 0.38 ± 0.01 and 0.54 ± 0.01 and an efficiency of $(3.34 \pm 0.01)\%$ and $(5.93 \pm 0.01)\%$.

Table 3.14: Overall modulation factors and efficiencies of AMEGO-X, for the spectrum of the GRB 170817A.

	Modulation factor		Efficiency (%)	
Energy range (keV)	ARM $< 15°$	ARM $< 30°$	ARM $< 15°$	ARM $< 30°$
125 to 225	0.52 ± 0.01	0.48 ± 0.01	1.36 ± 0.00	1.94 ± 0.01
200 to 400	0.38 ± 0.01	0.35 ± 0.01	3.34 ± 0.01	4.31 ± 0.01
100 to 500	0.40 ± 0.01	0.37 ± 0.01	1.89 ± 0.01	2.56 ± 0.01
100 to 700	0.38 ± 0.01	0.36 ± 0.01	1.96 ± 0.01	2.67 ± 0.01
100 to 1000	0.37 ± 0.01	0.35 ± 0.01	1.98 ± 0.01	2.70 ± 0.01

In figure 3.52 it is presented the MDP as a function of the observation time, for the GRB 170817A. As is the case for AMEGO (figure 3.40), the best MDP is obtained in the energy range with a maximum limit of 500 keV. The best MDP obtained with AMEGO, for 3 s of observation time, is ∼55%, while for AMEGO-X it is ∼78%.

It can be observed that in the 200 to 400 keV energy range, in contrast with the other energy ranges, the better MDP is obtained with an ARM cut of 15°. One possible reason for this is that in this energy range the flux is lower than in the other energy ranges, thus the reduction

of the background through the ARM cut event selection allows to obtain a better MDP.

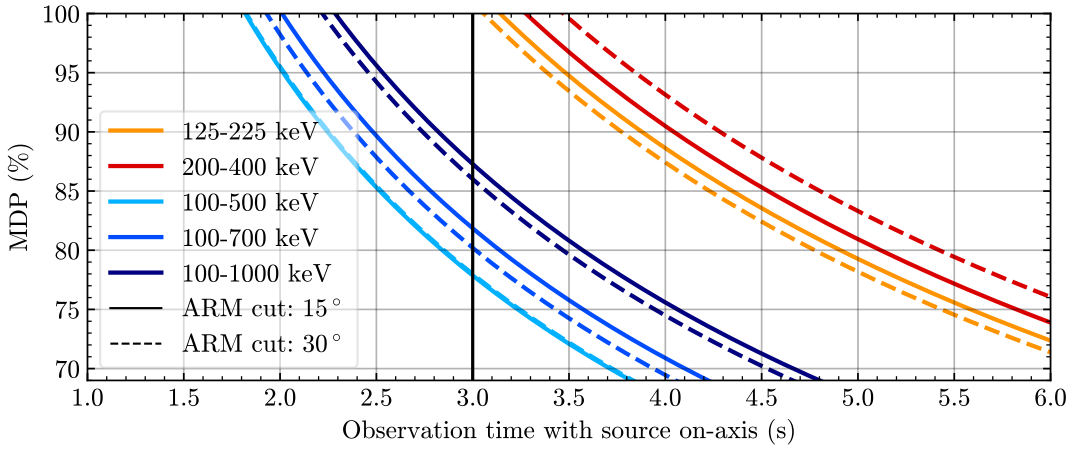

Figure 3.52: MDP for on-axis observations of the GRB 170817A, with AMEGO-X, as a function of the observation time.

GRB models

The fluxes of the GRB models are presented in table 3.15, and the modulation factors and efficiencies, that resulted from the simulations, are presented in table 3.16.

Table 3.15: Average fluxes of the GRB model for the energy ranges used in the simulation with AMEGO-X.

	Flux (photons cm^{-2} s^{-1})				
Energy range (keV)	Amp 1	Amp 5	Amp 10	Amp 15	Amp 20
100 to 500	0.792	3.935	7.869	11.804	15.739
100 to 700	0.918	4.560	9.121	13.681	18.242
100 to 1000	1.008	5.006	10.012	15.018	20.024

Table 3.16: Overall modulation factors and efficiencies of AMEGO-X, for the spectrum of the GRB models. Computed for an ARM cut of 15°.

Energy range (keV)	Modulation factor	Efficiency (%)
100 to 500	0.37 ± 0.01	2.64 ± 0.01
100 to 700	0.32 ± 0.01	2.94 ± 0.01
100 to 1000	0.28 ± 0.01	3.06 ± 0.01

In figure 3.53 it is presented the MDP as a function of the observation time, for the GRB model. It can be observed, that for the total duration of the GRBs (1 s), the MDP for the "Amp 20" is ∼20%, and that no polarimetric measurements can be performed with the "Amp

1" GRB. With AMEGO (figure 3.41), a MDP of ∼10% and ∼52% is achieved, for the "Amp 20" and "Amp 1" GRBs, respectively.

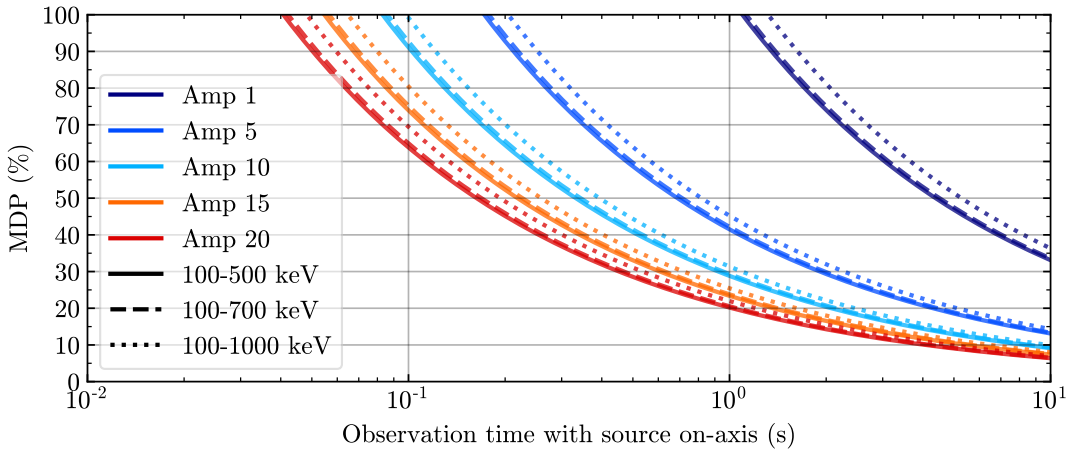

Figure 3.53: MDP for on-axis observations of the GRB models, with AMEGO-X, as a function of the observation time. Computed for an ARM cut of 15°. The solid lines overlap with the dashed ones.

Crab nebula

The fluxes of the Crab, for the simulated energy ranges, are presented in table 3.17. In table 3.18 are presented the modulation factors and efficiencies obtained with the Crab simulations.

Table 3.17: Average fluxes of the Crab for the energy ranges used in the simulation with AMEGO-X.

Energy range (keV)	Flux (photons cm^{-2} s^{-1})
125 to 225	0.016
200 to 400	0.010
100 to 1000	0.039

Table 3.18: Overall modulation factors and efficiencies of AMEGO-X, for the spectrum of the Crab.

	Modulation factor		Efficiency (%)	
Energy range (keV)	ARM < 15°	ARM < 30°	ARM < 15°	ARM < 30°
125 to 225	0.52 ± 0.01	0.48 ± 0.01	1.32 ± 0.01	1.90 ± 0.01
200 to 400	0.37 ± 0.01	0.34 ± 0.01	3.37 ± 0.01	4.36 ± 0.01
100 to 1000	0.34 ± 0.01	0.32 ± 0.01	2.04 ± 0.01	2.82 ± 0.01

The MDP as a function of the observation time, for on-axis observations, is presented in figure 3.54. Comparing the MDP for observations of the Crab, with AMEGO (figure 3.54) and AMEGO-X, it can be observed that AMEGO presents a higher sensitivity to polarization,

but that for long observation times the MDP is almost of the same level. For example, for an observation time of 10^3 s, the MDP is ∼42% and ∼64%, for AMEGO and AMEGO-X, respectively, while for an observation time of 10^6 s, the MDP is ∼1% and ∼2%.

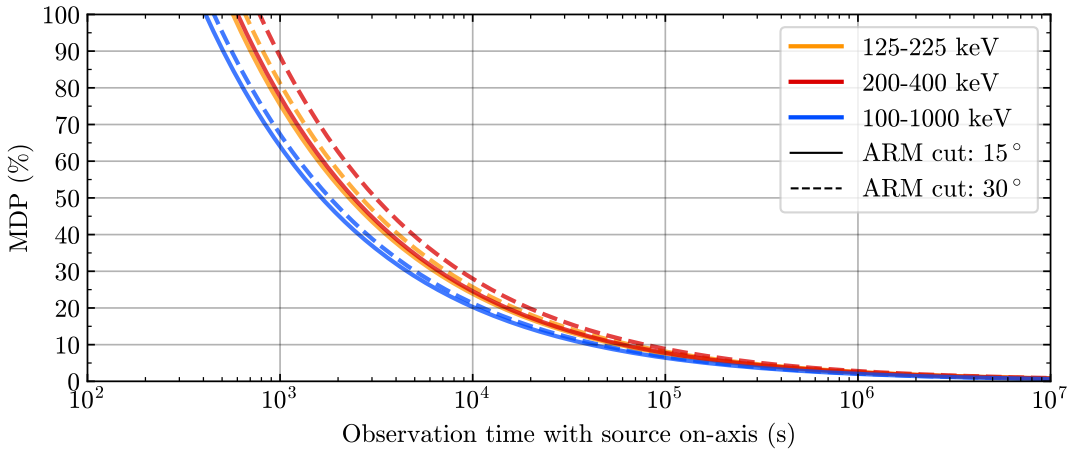

Figure 3.54: MDP for on-axis observations of the Crab, with AMEGO-X, as a function of the observation time.

In figure 3.55 it is presented the MDP, for Crab-like sources, as a function of the observation time. When comparing the MDPs achieved with AMEGO (figure 3.44) with the ones achieved with AMEGO-X, it can be observed that, for long observation times, the differences in sensitivity are more significant in weak sources. For example, for an observation time of 10^7 s, it is achieved a MDP of $< 1\%$, for 1 Crab sources, ∼4% and ∼6%, for 100 mCrab sources, and ∼41% and ∼62%, for 10 mCrab sources, for AMEGO and AMEGO-X, respectively.

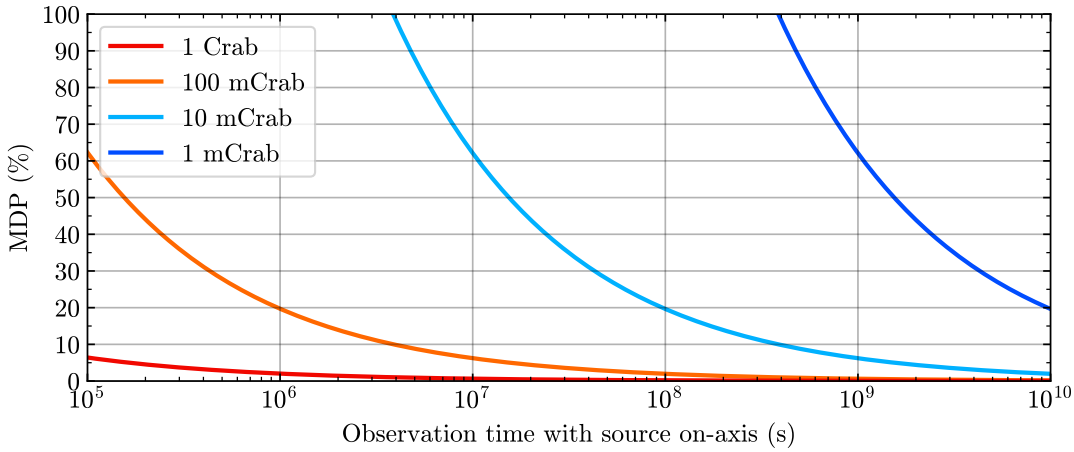

Figure 3.55: MDP for on-axis observations of the Crab-like sources, with AMEGO-X, in the 200 to 1000 keV energy range, as a function of the observation time. Computed for an ARM cut of 15°.

4

Conclusion

High-energy polarimetry is a relatively recent field, which allows to discriminate between competing models of emission mechanisms of astronomical sources, that can not be done with spectroscopic, imaging and timing measurements alone. It has contributed with polarimetric measurements of the Crab and of GRBs, but despite the progress the emission mechanisms of GRBs are still unknown. The objective of this work was to characterize, through simulations, the sensitivity to polarization of the AMEGO and AMEGO-X instruments. AMEGO will operate as a Compton-pair telescope observing the sky in survey mode, promoting synergies with other observatories and contributing to the multi-messenger astrophysics. It aims to increase the understanding of astronomical sources and extreme events, such as GWs, GRBs, active galactic nuclei and element formation in supernovae, through spectroscopic, imaging, timing and polarimetric measurements. Beyond the polarimetric capabilities, AMEGO will provide better sensitivities than previous instruments that operate in the MeV range.

As mentioned, this work contributed with the characterization of the polarimetric sensitivity of AMEGO and AMEGO-X. The data from the simulations also allow to calibrate the response of the instruments, which, along with laboratory measurements, will allow these instruments to perform polarimetric measurements, contributing to the study and understanding of extreme events in the universe. This data also allows to have a better understanding of the weight that each detector has on the overall efficiency and modulation factor of the instrument, and how the trigger criteria, such as which detectors require an interaction to activate the trigger and the energy required to recognize and measure an interaction, affect these parameters and thus, the sensitivity to polarization of the instruments. This work also shows that, dividing the analysis of polarimetric measurements into different energy ranges allows for the optimization of the sensitivity of the instrument, especially for GRBs. As the hardness of the sources may vary, it can be found an optimal trade-off between the flux of the source, background rates, modulation factor and efficiency of the instruments.

The modulation factors of AMEGO and AMEGO-X reach their maximum at low-energies, decreasing with the increase of the energy of the photons, presenting a value of 0.57 ± 0.03 and 0.43 ± 0.03, at 200 keV, and 0.16 ± 0.01 and 0.06 ± 0.01, at 1100 keV. The efficiency of AMEGO is at its highest at 600 keV, corresponding to $\sim 20\%$, while the efficiency of AMEGO-X corresponds to $\sim 5\%$, at this energy.

It was observed that the low-energy calorimeter is the detector that contributes the most for the modulation factor and efficiency of the instrument. The low-energy calorimeter detector consists of a 4 cm thick, high atomic number, single plane detector. Its thickness and high atomic number contributes to its efficiency and its single plane geometry to its high modulation factor, due to the measurement of photons that scatter close to right angles. Regarding pairs of detectors, the low-energy calorimeter and the tracker are the ones that contribute with the highest efficiency at lower energies ($\lesssim$ 800 keV), and the low-energy calorimeter and high-energy calorimeter at higher energies ($\gtrsim$ 800 keV). Regarding the contribution of the pairs of detectors to the modulation factor, it was observed that the pairs that contribute with the highest modulation factor are the ones that include the side low-energy calorimeter. These combinations of detectors favor the detection of photons that scatter close to right angles due to their geometrical displacement.

Regarding the sensitivities to polarization of the instruments in its operation conditions, the MDP as a function of the observation time was computed for the GRB 170817A, a model of short GRBs and the Crab. The results are summarized in table 4.1.

Table 4.1: Summary of MDPs obtained with AMEGO and AMEGO-X for different sources and observation times.

		AMEGO	AMEGO-X
Source	Observation time (s)	$MDP_{99\%}$ (%)	
GRB 170817A	Total duration of the event (3 s)	~ 55	~ 78
Least intense GRB of the GRB model	Total duration of the event (1 s)	~ 52	-
Most intense GRB of the GRB model	Total duration of the event (1 s)	~ 10	~ 20
Crab	10^3	~ 42	~ 64
	10^6	~ 1	~ 2
100 mCrab	10^7	~ 4	~ 6
10 mCrab	10^7	~ 41	~ 62

AMEGO presents better sensitivities, than AMEGO-X, to the degree of linear polarization from astronomical sources. Regarding the MDP of weak short GRBs, AMEGO is sensitive to these events if their emissions present a high degree of linear polarization, while AMEGO-X does not have enough sensitivity to perform polarimetric measurements. For intense short GRBs, both instruments are sensitive to polarization, but AMEGO has a better MDP than AMEGO-X. Regarding Crab-like sources, both instruments present a low MDP for a long observation time.

AMEGO also has better sensitivities to the polarization of the emission these sources comparing with AMEGO-X. The differences of the sensitivities are more relevant for weak sources and for short observation times.

For a 5-year mission of AMEGO, it is possible to perform polarimetric measurements of sources with flux down to $\sim$ 10 mCrab. The MDP is $\lesssim$ 1% for 1 Crab sources, $\sim$ 3% for 100 mCrab sources and $\sim$ 26% for 10 mCrab sources, at the end of the 5-year mission.

In conclusion, AMEGO presents a higher sensitivity to polarization and will be able to perform polarimetric measurements of weaker sources than AMEGO-X, which is a lighter and less complex instrument, with a smaller cost. The proposal of the two instruments increases the odds of one being accepted and launched, which will benefit many areas of the MeV astrophysics.

In **future work**, the MDP for long GRBs should be computed. Their softer spectrum, higher fluences and duration have a positive influence on the MDP, which should be confirmed through simulations. The MDP should also be computed for off-axis observations of GRBs. It was observed that when the observation time is short, the off-axis observations lead to a worse MDP. Since the GRBs have a short duration and are likely to be observed off-axis, due to the instruments operation in survey mode, the MDP should be estimated for these conditions.

As mentioned in this work, a prototype of AMEGO, that will be calibrated in the HIGS facility and will go through a balloon flight, is currently being built. The mass model of the prototype will be constructed and simulated, in order to compare the simulation results with the experimental values.

Lastly, as AMEGO operates as a Compton-pair telescope, its sensitivity to polarization should be evaluated using data from pair-production events. If it is shown to be possible to perform polarimetric measurements through this interaction mechanism with AMEGO, the polarimetric measurements can extend beyond a few MeV. The thickness of the layers of the tracker affect the efficiency and the multiple scattering of the charged particles, originated from pair-production events, altering their direction. Future work is required in order to study the trade-off between efficiency and the scattering of the particles, aiming to increase the sensitivity to polarization.

Bibliography

[1] F. Lei, A. J. Dean, and G. L. Hills. "Compton Polarimetry in Gamma-Ray Astronomy". In: *Space Science Reviews* 82.3 (Nov. 1997), pp. 309–388. DOI: 10.1023/A:1005027107614.

[2] C. Ilie. "Gamma-Ray Polarimetry: A New Window for the Nonthermal Universe". In: *Publications of the Astronomical Society of the Pacific* 131.1005 (Sept. 2019). ISSN: 1538-3873. DOI: 10.1088/1538-3873/ab2a3a.

[3] D. Götz et al. "The polarized gamma-ray burst GRB 061122". In: *MNRAS* 431 (June 2013), p. 3550. DOI: 10.1093/mnras/stt439.

[4] M. F. Moita. "Polarimeter Development for Future Space Gamma-ray Telescopes". Doctoral dissertation. Coimbra: University de Coimbra, 2020.

[5] M. G. Kirsch et al. "Crab: the standard x-ray candle with all (modern) x-ray satellites". In: *UV, X-Ray, and Gamma-Ray Space Instrumentation for Astronomy XIV* 5898 (2005). Ed. by O. H. W. Siegmund, pp. 22–33. DOI: 10.1117/12.616893.

[6] M. Forot et al. "Polarization of the Crab Pulsar and Nebula as Observed by the INTEGRAL/IBIS Telescope". In: *The Astrophysical Journal* 688.1 (Nov. 2008), pp. L29–L32. DOI: 10.1086/593974.

[7] H.-C. Li et al. "Phase-resolved gamma-ray spectroscopy of the Crab pulsar observed by POLAR". In: *Journal of High Energy Astrophysics* 24 (2019), pp. 15–22. ISSN: 2214-4048. DOI: 10.1016/j.jheap.2019.10.001.

[8] L. Kuiper et al. "The Crab pulsar in the 0.75-30 MeV range as seen by CGRO COMPTEL". In: *A&A* 378.3 (2001), pp. 918–935. DOI: 10.1051/0004-6361:20011256.

[9] A. Goldstein et al. "An Ordinary Short Gamma-Ray Burst with Extraordinary Implications: Fermi -GBM Detection of GRB 170817A". In: *The Astrophysical Journal* 848.2 (Oct. 2017), p. L14. ISSN: 2041-8213. DOI: 10.3847/2041-8213/aa8f41.

[10] B. P. Abbott et al. "GW170817: Observation of Gravitational Waves from a Binary Neutron Star Inspiral". In: *Phys. Rev. Lett.* 119 (16 Oct. 2017), p. 161101. DOI: 10.1103/PhysRevLett.119.161101.

[11] S.-N. Zhang et al. “Detailed polarization measurements of the prompt emission of five gamma-ray bursts”. In: *Nature Astronomy* 3.3 (Jan. 2019), pp. 258–264. ISSN: 2397-3366. DOI: 10.1038/s41550-018-0664-0.

[12] A. Thompson et al. *X-ray Data Booklet*. 3th. Lawrence Berkeley National Laboratory, 2009.

[13] M. Berger et al. *XCOM: Photon Cross Sections Database*. 2010. URL: https://physics.nist.gov/PhysRefData/Xcom/html/xcom1.html (visited on 05/17/2021).

[14] G. F. Knoll. *Radiation Detection and Measurement*. 4th. Wiley, 2010. ISBN: 978-0-470-13148-0.

[15] E. Costa et al. “An efficient photoelectric X-ray polarimeter for the study of black holes and neutron stars”. In: *Nature* 411.6838 (June 2001), pp. 662–665. ISSN: 1476-4687. DOI: 10.1038/35079508.

[16] M. C. Weisskopf et al. “The Imaging X-ray Polarimetry Explorer (IXPE)”. In: *Results in Physics* 6 (2016), pp. 1179–1180. ISSN: 2211-3797. DOI: 10.1016/j.rinp.2016.10.021.

[17] J. Hubbell. “Electron–positron pair production by photons: A historical overview”. In: *Radiation Physics and Chemistry* 75.6 (2006). Pair Production, pp. 614–623. ISSN: 0969-806X. DOI: 10.1016/j.radphyschem.2005.10.008.

[18] A. C. Zoglauer. “First Light for the Next Generation of Compton and Pair Telescopes”. Doctoral dissertation. München: Technische Universität München, 2005.

[19] D. Bernard. “Polarimetry of cosmic gamma-ray sources above e^+e^- pair creation threshold”. In: *Nuclear Instruments and Methods in Physics Research Section A: Accelerators, Spectrometers, Detectors and Associated Equipment* 729 (2013), pp. 765–780. ISSN: 0168-9002. DOI: 10.1016/j.nima.2013.07.047.

[20] P. Gros and D. Bernard. “γ-Ray polarimetry with conversions to e^+e^- pairs: Polarization asymmetry and the way to measure it”. In: *Astroparticle Physics* 88 (2017), pp. 30–37. ISSN: 0927-6505. DOI: 10.1016/j.astropartphys.2016.12.006.

[21] S. Wang et al. “HARPO: beam characterization of a TPC for gamma-ray polarimetry and high angular-resolution astronomy in the MeV-GeV range”. In: *Journal of Physics: Conference Series* 650 (Nov. 2015). ISSN: 1742-6596. DOI: 10.1088/1742-6596/650/1/012016.

[22] P. Gros et al. “First measurement of the polarisation asymmetry of a gamma-ray beam between 1.7 to 74 MeV with the HARPO TPC”. In: *Space Telescopes and Instrumentation 2016: Ultraviolet to Gamma Ray* 9905 (2016). Ed. by J.-W. A. den Herder, T. Takahashi, and M. Bautz, pp. 893–905. DOI: 10.1117/12.2231856.

[23] V. Schonfelder and G. Kanbach. “Imaging through Compton scattering and pair creation”. In: *ISSI Scientific Reports Series* 9 (Jan. 2010), pp. 207–222. DOI: 10.1007/978-1-4614-7804-1_11.

[24] A. Zoglauer and G. Kanbach. "Doppler broadening as a lower limit to the angular resolution of next generation Compton telescopes". In: *Trümper, Joachim E.; Tananbaum, Harvey D.: X-Ray and Gamma-Ray Telescopes and Instruments for Astronomy, SPIE (2003)* 4851 (Mar. 2003), pp. 1302–1309. DOI: 10.1117/12.461177.

[25] F. Lei et al. "Characteristics of COMPTEL as a polarimeter and its data analysis." In: *Astronomy and Astrophysics Supplement Series* 120 (Nov. 1996), p. 695.

[26] P. Laurent et al. "Constraints on Lorentz Invariance Violation using integral/IBIS observations of GRB041219A". In: *Physical Review D - PHYS REV D* 83 (June 2011). DOI: 10.1103/PhysRevD.83.121301.

[27] E. Caroli et al. "Hard X-ray and Soft Gamma Ray Polarimetry with CdTe/CZT Spectro-Imager". In: *Galaxies* 6.3 (2018). ISSN: 2075-4434. DOI: 10.3390/galaxies6030069.

[28] R. M. Curado Da Silva et al. "Cipher, A Polarimeter Telescope Concept for Hard X-Ray Astronomy". In: *Experimental Astronomy* 15.1 (Feb. 2003), pp. 45–65. ISSN: 1572-9508. DOI: 10.1023/B:EXPA.0000028168.26442.30.

[29] M. Bagheri, J. R. Dwyer, and M. L. McConnell. "On the Linear Polarization of TGFs and X-Rays From Natural and Rocket-Triggered Lightning and Its Association With Source Geometry". In: *Journal of Geophysical Research: Space Physics* 124.11 (2019), pp. 9166–9183. DOI: 10.1029/2019JA026570.

[30] *INTEGRAL's Instruments*. URL: http://www.isdc.unige.ch/integral/outreach/integral (visited on 09/28/2021).

[31] T. Kamae et al. "PoGOLite – A high sensitivity balloon-borne soft gamma-ray polarimeter". In: *Astroparticle Physics* 30.2 (2008), pp. 72–84. ISSN: 0927-6505. DOI: 10.1016/j.astropartphys.2008.07.004.

[32] M. Chauvin et al. "The design and flight performance of the PoGOLite Pathfinder balloon-borne hard X-ray polarimeter". In: *Experimental Astronomy* 41.1-2 (Aug. 2015), pp. 17–41. ISSN: 1572-9508. DOI: 10.1007/s10686-015-9474-x.

[33] M. Chauvin et al. "Observation of polarized hard X-ray emission from the Crab by the PoGOLite Pathfinder". In: *Monthly Notices of the Royal Astronomical Society: Letters* 456.1 (Dec. 2015), pp. L84–L88. ISSN: 1745-3925. DOI: 10.1093/mnrasl/slv177.

[34] M. Kole. "Polarimetry with POLAR". In: *PoS* MULTIF2017 (2018), p. 068. DOI: 10.22323/1.306.0068.

[35] S. Xiong et al. "Overview of the GRB observation by POLAR". In: *PoS* ICRC2017 (2018), p. 640. DOI: 10.22323/1.301.0640.

[36] J. Hulsman. "POLAR-2: a large scale gamma-ray polarimeter for GRBs". In: *Space Telescopes and Instrumentation 2020: Ultraviolet to Gamma Ray* (Dec. 2020). Ed. by J.-W. A. den Herder, K. Nakazawa, and S. Nikzad. DOI: 10.1117/12.2559374.

[37] *Flat panel type multianode PMT assembly H8500 series / H10966 series.* TPMH1327E. Hamamatsu Photonics K.K. July 2011.

[38] M. Kole et al. "POLAR: Final calibration and in-flight performance of a dedicated GRB polarimeter". In: *IEEE Nuclear Science Symposium, Medical Imaging Conference and Room-Temperature Semiconductor Detector Workshop (NSS/MIC/RTSD)* (2016), pp. 1–6. DOI: 10.1109/NSSMIC.2016.8069846.

[39] N. Produit et al. "POLAR, a compact detector for gamma-ray bursts photon polarization measurements". In: *Nuclear Instruments and Methods in Physics Research Section A: Accelerators, Spectrometers, Detectors and Associated Equipment* 550.3 (2005), pp. 616–625. ISSN: 0168-9002. DOI: 10.1016/j.nima.2005.05.066.

[40] M. Kole et al. "Instrument performance and simulation verification of the POLAR detector". In: *Nuclear Instruments and Methods in Physics Research Section A: Accelerators, Spectrometers, Detectors and Associated Equipment* 872 (Nov. 2017), pp. 28–40. ISSN: 0168-9002. DOI: 10.1016/j.nima.2017.07.070.

[41] P. Bloser et al. "The MEGA project: Science goals and hardware development". In: *New Astronomy Reviews* 50.7 (2006). Astronomy with Radioactivities. V, pp. 619–623. ISSN: 1387-6473. DOI: 10.1016/j.newar.2006.06.001.

[42] A. Zoglauer, R. Andritschke, and F. Schopper. "MEGAlib – The Medium Energy Gamma-ray Astronomy Library". In: *New Astronomy Reviews* 50.7 (2006). Astronomy with Radioactivities. V, pp. 629–632. ISSN: 1387-6473. DOI: 10.1016/j.newar.2006.06.049.

[43] C. A. Kierans. "AMEGO: A Multimessenger Mission for the Extreme Universe - Response to Astro2020 Decadal Request for Information." In: *Space Telescopes and Instrumentation 2020: Ultraviolet to Gamma Ray* (2020). URL: https://asd.gsfc.nasa.gov/amego/files/AMEGO_Decadal_RFI.pdf.

[44] J. McEnery et al. "All-sky Medium Energy Gamma-ray Observatory: Exploring the Extreme Multimessenger Universe". In: *Bulletin of the AAS* 51.7 (Sept. 30, 2019). URL: https://baas.aas.org/pub/2020n7i245.

[45] C. A. Kierans. "AMEGO: exploring the extreme multi-messenger universe". In: *Space Telescopes and Instrumentation 2020: Ultraviolet to Gamma Ray* (Dec. 2020). Ed. by J.-W. A. den Herder, K. Nakazawa, and S. Nikzad. DOI: 10.1117/12.2562352.

[46] Y. Cui et al. "CZT virtual Frisch-grid detector: Principles and applications". In: *2009 IEEE Long Island Systems, Applications and Technology Conference* (2009), pp. 1–5. DOI: 10.1109/LISAT.2009.5031559.

[47] W. J. McNeil et al. "Single-charge-carrier-type sensing with an insulated Frisch ring CdZnTe semiconductor radiation detector". In: *Applied Physics Letters* 84.11 (2004), pp. 1988–1990. DOI: 10.1063/1.1668332.

[48] A. Moiseev et al. “High-energy 3D calorimeter for use in gamma-ray astronomy based on position-sensitive virtual Frisch-grid CdZnTe detectors”. In: 12.12 (Dec. 2017). ISSN: 1748-0221. DOI: 10.1088/1748-0221/12/12/c12037.

[49] R. S. Woolf et al. “Development of a CsI:Tl calorimeter subsystem for the All-Sky Medium-Energy Gamma-Ray Observatory (AMEGO)”. In: (2018), pp. 1–6. DOI: 10.1109/NSSMIC.2018.8824629.

[50] A. Zoglauer et al. “Status of instrumental background simulations for gamma-ray telescopes with Geant4”. In: *2008 IEEE Nuclear Science Symposium Conference Record* (2008), pp. 2859–2864. DOI: 10.1109/NSSMIC.2008.4774966.

[51] D. Green. *Using Fermi’s Anti-Coincidence Detector to Measure Cosmic Ray Abundances*. 2018. URL: https://fermi.gsfc.nasa.gov/fermi10/fridays/05112018.html (visited on 08/25/2021).

[52] C. B. Wunderer et al. “The ACT vision mission study simulation effort”. In: *New Astronomy Reviews* 50.7 (2006). Astronomy with Radioactivities. V, pp. 608–612. ISSN: 1387-6473. DOI: 10.1016/j.newar.2006.06.064.

[53] H. Fleischhack. *AMEGO-X: MeV gamma-ray Astronomy in the Multimessenger Era*. 2021. arXiv: 2108.02860.

[54] I. Brewer et al. “Developing the future of gamma-ray astrophysics with monolithic silicon pixels”. In: *Nuclear Instruments and Methods in Physics Research Section A: Accelerators, Spectrometers, Detectors and Associated Equipment* (2021), p. 165795. ISSN: 0168-9002. DOI: 10.1016/j.nima.2021.165795.

[55] R. Caputo et al. “AstroPix: investigating the potential of silicon pixel sensors in the future of gamma-ray astrophysics”. In: 11444 (2020). Ed. by J.-W. A. den Herder, S. Nikzad, and K. Nakazawa, pp. 445–456. DOI: 10.1117/12.2562327.